Universidade de Aveiro
2023

Artur Alexandre da Conceição Chaves

Design and fabrication of an artificial cervical disc implant combining 3D electrospinning and hydrogel

Projeto e fabricação de implante de disco cervical artificial combinando eletrofiação 3D e hidrogel

Universidade de Aveiro
2023

Artur Alexandre da Conceição Chaves

Design and fabrication of an artificial cervical disc implant combining 3D electrospinning and hydrogel

Projeto e fabricação de implante de disco cervical artificial combinando eletrofiação 3D e hidrogel

Trabalho de Projeto apresentado à Universidade de Aveiro para cumprimento dos requisitos necessários à obtenção do grau de Mestre em Engenharia Mecânica, realizada sob orientação científica de António Manuel Godinho Completo, Professor Associado com Agregação, do Departamento de Engenharia Mecânica da Universidade de Aveiro, e de Paula Alexandrina de Aguiar Pereira Marques, Investigadora Principal do Departamento de Engenharia Mecânica da Universidade de Aveiro.

Este trabalho de projeto teve o apoio dos projetos UIDB/00481/2020 e UIDP/00481/2020 - Fundação para a Ciência e a Tecnologia; e CENTRO-01-0145 FEDER-022083 - Programa Operacional Regional do Centro (Centro2020), através do Portugal 2020 e do Fundo Europeu de Desenvolvimento Regional.

O júri / The jury

Presidente / President

Prof. Doutor Fábio António Oliveira Fernandes
Professor Auxiliar em Regime Laboral da Universidade de Aveiro

Vogais / Committee

Doutor Jorge Américo de Oliveira Pinto Belinha
Professor Adjunto do *Instituto Superior de Engenharia do Porto*

Prof. Doutor António Manuel Godinho Completo
Professor Associado com Agregação da Universidade de Aveiro

Agradecimentos / Acknowledgements

Ao Professor Doutor António Completo, pelos ensinamentos, orientação, paciência e disponibilidade que teve durante todo o projeto. À Professora Doutora Paula Marques pela disponibilidade e ajuda prestada. Aos investigadores do TEMA (Centre for Mechanical Technology and Automation), em especial ao Professor Gil Alberto Batista Gonçalves.
Aos meus pais e irmão pelo apoio constante e por me ajudarem a atingir os meus objetivos.
Aos meus amigos, porque isto sem eles também não seria possível. Em especial ao Teófilo por me aturar e ouvir sempre que preciso, um segundo irmão para mim. À Filipa pela ajuda e companhia neste percurso. Ao José Pedro Carreira pelas horas de estudo, que se tornaram mais fáceis. Ao Luís Verdasca por todas as vezes que me ouviu falar deste projeto.
Um especial agradecimento aos meus avós.

Keywords Artificial disc, Cervical disc, Annulus fibrosus, nucleus pulposus, 3D electrospinning, Hydrogel, Degenerative disc disease

Abstract

Cervical spine pain is a common ageing problem. The painful condition may be associated to some disorders, such as intervertebral disc degeneration, disc herniation, spinal stenosis, and facet arthritis, that limit people's quality of life. The most common treatment for these issues is surgical intervention, in which cervical fusion is performed. However, cervical fusion has its limitations and problems. Such limitations are increasing the use of artificial discs, which can contribute to eliminating pain and restoring movement. Despite this being a good concept, there are few artificial discs designed for this purpose. Therefore, this project has the main objective of exploring the possibilities of fabricating an experimental artificial disc that mimics the native cervical disc, combining 3D electrospinning and hydrogel. A bibliographic review was conducted in the initial phase of the project. Starting with the anatomy, biomechanics, pathologies and repair techniques of the cervical disc. Followed by the cervical disc implants that are in use or being developed, and concluded with the materials and fabrication processes. In the second phase of the project, the concept design was developed, followed by the 3D modelling of the concept using CAD software and, finally, the simulation of the models. In the third phase of the project, with the model in mind, and with the understanding gained in the numerical simulation, started an exploratory phase on the hydrogels to try to find the best one to mimic the nucleus pulposus. The three best hydrogels were used in the fabrication of the disc. The fabrication of the artificial annulus fibrosus was then initiated, using the 3D electrospinning system, and the deposition of the hydrogel in the centre of the disc. Twelve samples were fabricated with the three different hydrogels. Lastly, the fabricated discs were mechanically characterized, using the SEM, Micro-ct and mechanical tests at compression until 20% deformation. The mechanical tests were made in different states of the fabrication of the discs.

The results obtained showed that the disc manufactured using this method is possible. However, the direct comparison with the native disc showed that this disc concept exhibits significantly inferior mechanical properties. There is room for improvement, and this work serves to highlight that this concept can still be enhanced in terms of materials and geometry in order to approach the behaviour of the native disc.

Palavras-chave Disco artificial, Disco cervical, Ânulo fibroso, Núcleo pulposo, Eletrofiação 3D, Hidrogel, Doença degenerativa do disco

Resumo

A dor na coluna cervical é um problema comum no envelhecimento. Essa dor pode ser devido a distúrbios como degeneração do disco intervertebral, hérnia de disco, estenose espinhal e artrite facetária, que limitam a qualidade de vida das pessoas. O tratamento mais comum para esses problemas é a intervenção cirúrgica, na qual é realizada a fusão cervical. Essa fusão possui limitações e problemas. Devido a isso, começaram a ser utilizados discos artificiais, que além de eliminar a dor, restauram o movimento. Apesar de ser um bom conceito, existem poucos discos artificiais com esse objetivo. Por essas razões, este projeto tem como objetivo principal explorar as possibilidades de fabricar um disco artificial experimental que imite o disco cervical nativo, combinando a técnica de eletrofiação 3D e hidrogel. Na fase inicial do projeto, foi realizada uma revisão bibliográfica, abrangendo a anatomia, biomecânica, patologias e técnicas de reparação do disco cervical. Em seguida, foram estudados os implantes de disco cervical que estão em uso ou em desenvolvimento, e finalizou-se com os materiais e processos de fabricação. Na segunda fase do projeto, iniciou-se o design conceitual, seguido pela modelagem 3D do conceito utilizando software CAD e, finalmente, foram feitas simulações dos modelos. Na terceira fase do projeto, com o modelo em mente e com o entendimento adquirido na simulação numérica, iniciou-se uma fase exploratória dos hidrogéis para tentar encontrar o melhor para imitar o núcleo pulposo. Os três melhores hidrogéis foram utilizados na fabricação do disco. Em seguida, iniciou-se a fabricação do anel fibroso artificial utilizando o sistema de eletrofiação 3D e a deposição do hidrogel no centro do disco. Foram fabricadas doze amostras com os três diferentes hidrogéis. A última fase foi a caracterização mecânica dos discos fabricados, utilizando SEM, Micro-CT e testes mecânicos de compressão até 20% de deformação. Os testes mecânicos foram realizados em diferentes estados de fabricação dos discos.

Os resultados obtidos, mostraram que o disco fabricado com este método é de possível execução. No entanto, a comparação direta com o disco nativo, mostrou que este conceito de disco exibe propriedades mecanicas bastante inferiores. Há espaço para melhorias, e este trabalho serve para evidenciar que este conceito pode ainda ser melhorado, em termos de materiais e geometria, por forma a aproximar-se do comportamento do disco nativo.

Contents

List of Tables

List of Figures

Chapter 1

Introduction

1.1 Background and motivation

The human spine is a very complex and sound structure that not only supports the body and protects the spinal cord, but also enables a very wide range of motion for the body. The spine is divided into four main parts: the cervical spine, the thoracic spine, the lumbar spine, and the sacrum. This project focuses on the fabrication of an artificial intervertebral disc (IVD) for the cervical spine.

The cervical spine not only supports the head and neck but also sustains compressive and shear forces and transfers them to the lower parts of the spine. However, disorders of the cervical spine are relatively common with age. These disorders include: IVD degeneration, disc herniation, spinal stenosis, facet arthritis, and cervical spondylosis, all of these disorders cause pain. Many people suffer from pain caused by these disorders; it limits their daily activities and reduces their quality of life. So solutions are needed to help people overcome these problems.

In general, physiotherapy or medication is the first treatment for pain resulting from an IVD disorder. Surgical treatment may be required if pain continues to worsen, to decompress pinched nerves. The most popular treatment for cervical IVD is anterior cervical discectomy and fusion. This procedure consists in removing the IVD and replacing it with a metal bracket (cage) to restore the natural height of the replaced disc, which helps to eliminate the pain. However, this procedure will reduce the range of movements of this section of the spine, which has been reported to cause the adjacent IVDs to deteriorate. For these reasons, the use of artificial IVDs is starting to be more common. It allows spinal decompression, preserves the movement of the cervical segment, maintains the length of the initial cervical segment, minimises degenerative alterations in the adjacent discs, and allows a quick recovery. Although a good concept, there are only a few implants the aim is to replace the native IVD.

Human IVD is a cylindrical fibrocartilage tissue that enables spinal movement by evenly distributing the load over the vertebral body. The disc has a cylindrical shape and comprises three tissue components: nucleus pulposus (NP) (acts as a shock absorber), annulus fibrosus (AF) (contains the NP), and end plates (EP) (attaches the IVD to the vertebrae). With this in mind, using the structure of the native IVD, the aim of the project is to make an artificial IVD using 3D electrospinning of PCL fibres and hydrogel fusion, using titanium plates as endplates, that has similar mechanic properties to the native IVD.

1.2 Aim

The current project focuses on the fabrication of an artificial disc utilizing the 3D electrospinning technique available at the University of Aveiro to produce a mimic of the annulus fibrosus, in conjunction with hydrogel to mimic the nucleus pulposus. The intention behind this research is to explore the potential of this novel approach, as it differs from the currently available disc implants in the market. By starting this exploratory work, the aim is to fabricate a prototype of the artificial disc using this idea.

For this, it was necessary to develop a concept of the disc, using CAD software, and explore different models using computational simulation to understand them. After that, it is necessary to explore the available materials to find a suitable hydrogel solution that would mimic the nucleus pulposus behaviour and mechanical properties. Fabricate both the artificial annulus fibrosus with the system and combine them with the hydrogel artificial nucleus pulposus. Finally, mechanically characterise the disc and discuss its viability.

1.3 Dissertation Structure

The dissertation is organized into six chapters. Chapter one presents the background and motivation, the aim of the project, and the dissertation structure.

Chapter two consists of a bibliographic review of the anatomy of the cervical spine and cervical disc, the biomechanics, pathologies and techniques for the reparation of the cervical disc.

Chapter three provides an overview of the existing options for treating degenerative disc conditions. It discusses two main devices that are currently utilized: interbody fusion cages and artificial discs. Furthermore, the chapter presents ongoing research on alternative concepts that are different from the devices currently available in the market. A literature review is conducted, encompassing studies on native cervical discs, existing implants, as well as new concepts.

Chapter four goes into the materials and processes used currently to fabricate both the artificial nucleus pulposus as well as the artificial annulus fibrosus. There is a special focus on hydrogel production and polymer solutions as well as research on the basics of the electrospinning system.

Chapter five consists of the experimental part of the dissertation, containing the results, its analysis and discussion. Starting with the development of the concept by modelling in CAD software, all the conditions and material properties used in the numerical simulation, the results of this simulation, as well as, a discussion of said results. Next, the preparation of all the materials and solutions used, as well as, the exploratory phase regarding the hydrogel choice. Followed by the fabrication of the artificial disc, the mechanical characterisation using the SEM, Micro-ct and the mechanical tests. Lastly, comes the presentation of the results, its analysis and discussion.

Chapter six contains the conclusions and possible future works for the project. The dissertation contains two appendices. First comes appendix A, which contains the results of all the mechanical properties of all the disc samples. Appendix B contains the results from the studied parameter for the excluded samples.

Chapter 2

Anatomy, biomechanics, pathologies and techniques for cervical disc repair

2.1 Introduction

This chapter provides an overview of the cervical spine and the cervical disc, focussing on the anatomy, biomechanics, pathology of these elements and methods of cervical disc repair.

The human spinal column is the structural pillar of the body. It consists of 33 vertebrae and 23 intervertebral discs (IVD) (Figure 2.1). It is divided into five regions: cervical, thoracic, lumbar, sacral, and coccyx. Each region has 7, 12, 5, 5, and 4 vertebrae, respectively. The stability and flexibility of the human spine are guaranteed by articulations, muscles, ligaments, and tendons. The stacking of vertebrae forms the vertebrae canal. This canal is an anatomical space formed by the vertebral column that stores an integral portion of the central nervous system [1]: the spinal cord and the spinal nerve roots that branch off the spinal cord bilaterally.

(a) The segments of the human spine

(b) The cervical spine.

Figure 2.1: Anatomy of the human spine. (Adapted from [2]).

2.2 Anatomy

2.2.1 Cervical spine

As mentioned above, the cervical spine has seven vertebrae labelled C1 to C7 and six intervertebral discs. C1 is the upper level of the cervical spine and connects the scull, while C7, the lowest, is connected to the top of the trunk, where the thoracic vertebrae and the rib cage begin [2].

C1 and C2 vertebrae have special characteristics that distinguish them from the other vertebrae. The atlas and axis, C1 and C2, respectively, are part of the craniovertebral junction of the spine. These two vertebrae are responsible for approximately 50% of flexion and 50% of rotation of the neck [2]. The remaining vertebrae (C3 to C7) have less mobility and provide support to the head and neck. The cervical vertebrae, as a group, produce a lordotic curve [3].

The cervical spine is responsible for protecting the efferent and afferent nerves, which derive from the spinal cord. If damaged, it can have dramatic effects on the nervous system, eventually affecting the patient's daily activities and even causing potential paralysis [2]. The cushioning and supporting load of the intervertebral discs is critical to the longevity of the vertebrae and, therefore, nerves, as they pass through the same joint separation.

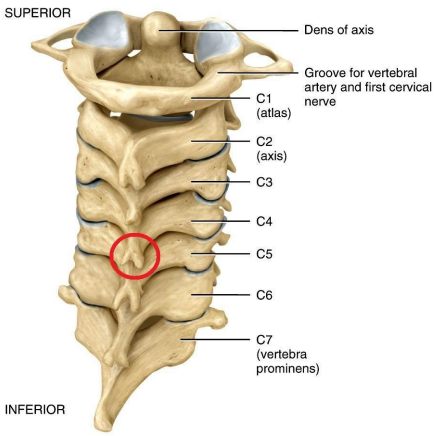

Figure 2.2: Cervical spine [4]

2.2.1.1 Vertebrae

Typical vertebrae consist of a vertebral body, a vertebral arch, and seven processes. The body bears the majority of the force placed on the vertebra [5], andis composed of trabecular bone, which contains the red marrow, and is surrounded by an external layer of cortical bone. The arch, along with the posterior aspect of the body, forms the vertebral canal, which contains and protects the spinal cord [5].

Typical vertebrae articulate with the above and below through three types of joints: zygapophyseal, which are synovial joints formed by the facets of the articular processes; fibrous attachments between the laminae and the spinous processes; and a cartilaginous joint in the form of a fibrocartilaginous intervertebral disk that firmly unites the bodies

of adjacent vertebrae while allowing for a small amount of movement [6]. These joints maintain the alignment of the vertebrae, control the range of motion, and are weight bearing at certain positions.

There are two special vertebrae in the cervical spine, C1 and C2. The C1 lacks the vertebral body and a spinous process. The circular bone contains two bilateral masses that take the place of a body in its load-bearing capacity [5].

C2 differs in that it contains bilateral masses to articulate with C1, a body through which weight is transmitted through C3 and below, and an odontoid process [5, 6].

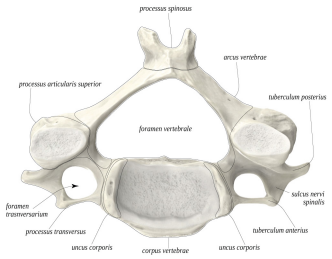

(a) Top view of the C4 vertebra

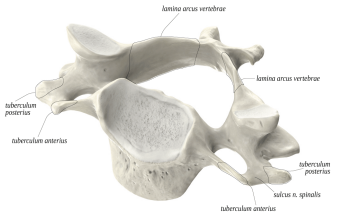

(b) Isometric view of the C3 vertebra

Figure 2.3: Anatomy of the cervical vertebra. (Adapted from [5]).

2.2.1.2 Spinal cord

The spinal cord acts as a conduit for information from the brain to the peripheral, it measures 40 to 45 cm in length, in an adult, and occupies two thirds of the vertebral canal [7]. Enclosed in three membranes (or meninges) are: the dura mater, the arachnoidea and the pia mater from the superficial layer to the deeper layer [7].

The spinal cord is divided into 31 segments (eight cervical, twelve thoracics, five lumbar, five sacral and one coccygeal) [8]. With the exception of C1, which does not have a sensory nerve root, each segment of the spinal cord has a pair of dorsal roots (sensory root) and ventral roots (motor root) that join to form a mixed spinal nerve [8]. Each segment corresponds to a vertebra, apart from C8, which does not have a corresponding vertebra.

Pathological processes affecting the spinal cord, even those limited to a small area, are usually clinically apparent, taking into account the role the spinal cord plays in the human body.

2.2.2 Cervical disc

The vertebrae of the cervical spine (excluding vertebrae C1 and C2), the thoracic and lumbar spines are separated by an intervertebral disc, each named for the two vertebrae between which they sit, for example, C5-C6. The first intervertebral disc is located between the vertebral bodies C2 and C3.

IVDs make up approximately 20-30% of the total length of the spine [2], they have important mechanical functions such as load cushioning, reducing stress caused by impact, weight dispersion, and movement of individual vertebrae, and also help with the

transport of nutrients and fluids to the spine and spinal cord [2]. It is a cylindrical fibrocartilage tissue composed of three tissue components: nucleus pulposus (NP), annulus fibrosis (AF), and endplates (EP) (Figure 2.4).

The structure and mechanical properties of IVD vary along the spinal column, to adapt to different loads, stresses, strains, and range of movements [9]. The dimensions of the cervical IVD were obtained by [10], scanning ten asymptomatic patients (6 men and 4 women) and measuring in the static neutral position. Anterior-posterior (AP), medial-lateral (ML), and superior-inferior (SI) dimensions were obtained as seen in Table 2.1. IVDs in the cervical spine have a smaller cross-sectional area than any other disc in the spine. This is because the load on the cervical spine is lower than any other section of the spine, which does not require a significant load distribution [2]. The average cross-sectional areas and thicknesses taken from 70 cervical discs range from 190 to 440 mm2 and from 3.5 to 4.5 mm, respectively, according to Frost et al. [2]. These measurements can also be seen in Table 2.1.

Table 2.1: Average dimension of the intervertebral discs in the cervical spine [2, 10]

Disc Level	IVD dimensions (mm)			Disc Height (mm)	Area (mm^2)
	AP	ML	SI		
C2/C3	-	-	-	3.51 ± 0.71	190 ± 10
C3/C4	17.3 ± 1.9	16.4 ± 1.5	4.1 ± 0.9	3.74 ± 0.36	280 ± 40
C4/C5	17.7 ± 1.6	16.6 ± 1.5	4.2 ± 0.9	4.07 ± 0.36	240 ± 20
C5/C6	17.8 ± 1.8	17.7 ± 1.5	4.2 ± 0.8	4.45 ± 0.21	300 ± 30
C6/C7	18.2 ± 1.9	21.0 ± 2.3	3.7 ± 0.5	4.11 ± 0.28	460 ± 5
C7/T1	-	-	-	4.50 ± 0.53	440 ± 5

2.2.2.1 Nucleus pulposus

The nucleus pulposus is a gel-like material that is located in the centre of the disc and is surrounded by the AF which prevents it from leaking into the spinal canal. It contains 70-90% of water [2,11] while its dry weight contains approximately 35 to 65% proteoglycan, 5 to 20% fine type II collagen fibrils. The remaining dry weight contains some non-collagenous proteins and elastin [11]. This mixture of type II collagen and proteoglycan creates a high hydrostatic pressure and provides NP with swelling properties that help overcome deformation and maintain disc height [12]. When exposed to certain forces, the NP deforms and transmits these forces to the surrounding AF. With age, the water content and height of the NP start to decrease. At a young age, the NP is fully hydrated, which means that when a normal compressive force is applied, it is evenly distributed between the AF and the NP. In older patients, the normal compressive force is shifted toward the AF [13].

2.2.2.2 Annulus fibrosus

The annulus fibrosus usually contains 15-25 concentric fibrous lamellae, which circumferentially surround the NP structure and confine its pressure. Each lamella is made up of organised collagen fibres that are orientated approximately 30 degrees to the horizontal [11]. This angle changes direction from one lamella to the next, forming a criss-cross

pattern to support compressive and torsional forces [11–13]. The AF contains 65–70% water, and its dry weight is approximately 20% proteoglycan, 50–70% collagen and 2% elastin [2, 11]. This tissue is then divided into three separate regions: the outer AF contains primarily type I collagen fibres produced by elongated, fusiform, fibroblast-like cells of mesenchymal origin; the inner AF primarily type II collagen fibres produced by rounded chondrocyte-like cells [11], There is also a transition zone between the outer and inner AF. The thickness of each lamella varies between 100-500 µm where the thicker layers are in the outer AF, meaning that the inner lamellar are thinner [11].

2.2.2.3 End plate

Endplates (EP) are two layers of cartilage that cover each lower and upper vertebral disc. Its thickness ranges from 0.6 to 1 mm [11,12]. The EP serves as a physical barrier between the NP and the vertebral bone, preventing the disc from exerting pressure directly on the bone, transporting nutrients into the IVD from the blood vessels [2, 11, 12]. The EP and NP have similar chemical compositions. Collagen type II and proteoglycan make up the majority of the dry weight of the EP, with about 60% water [11].

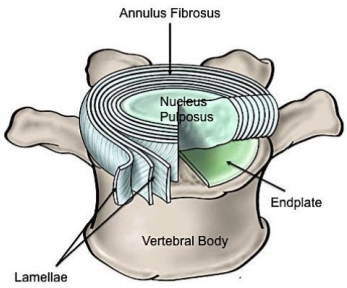

(a) Intervertebral disc. This image was taken from [12]

(b) Human intervertebral disc.

Figure 2.4: Anatomy of the cervical disc.

2.3 Biomechanics

The goal of studying the biomechanics of the human body is to understand the structure, function, range of motion (ROM), and mechanical properties of body parts, organs, or even cells, in daily activities, with the help of mechanical tests.

2.3.1 Cervical spine

Cervical spines have the fundamental function of transmitting the axial load of the skull, maintaining horizontal gaze, allowing normal movement of the head and neck, and protecting important neurovascular structures such as the spinal cord. The foundation for performing many everyday tasks and maintaining a high quality of life is a healthy and properly functioning cervical spine. Normally, the cervical spine has a C shape and is not completely vertical. This natural curvature is known as cervical lordosis.

According to Tan (2017) [14], the centre of mass of the skull is thought to lie 10mm anterior to the supratragic notch immediately above the mandibular head. The posterior

tension band and paraspinal muscles compensate for forward bending motion caused by head weight in a regularly positioned lordotic cervical spine, maintaining natural cervical alignment [14]. The axial load of the cranium is first transferred from the occipital condyles to the lateral masses of C1, then to the C1-C2 facet joints, then to the lateral masses of C2, and finally is distributed to the rest of the spinal column via C2-C3 IVD and facet joints. About two thirds of the axial stress in the subaxial cervical neck is carried by the facet joints, while the remaining one third is transmitted by the intervertebral discs [14].

2.3.1.1 Range of motion (ROM)

The cervical spine has 6 degrees of freedom [14]. The main motions of the cervical spine are flexion/extension, lateral bending, and axial rotation. Some small amounts of anterior/posterior translation movements can also be performed [14].

In general, the cervical spine has the following ROM according to [14, 15] (Table 2.3): 90°of flexion, 70°of extension, 20°to 45°of lateral bending, and up to 90°of rotation. However, cervical spine movements are complex, mainly because pure uniplanar motion does not adequately represent movement between cervical levels, and travelling within any range is not a simple addition of equal motion from one vertebra to the next [15].

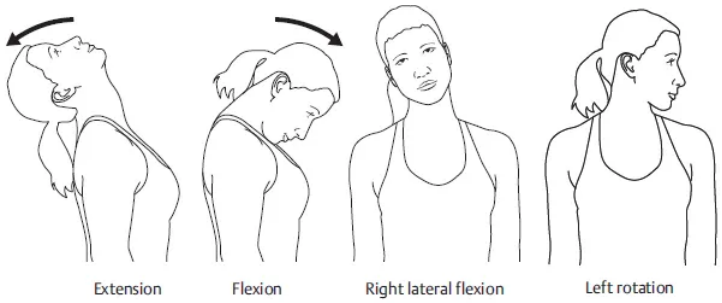

Figure 2.5: Kinetic motions of the cervical spine. [16]

Table 2.2: ROM of the cervical spine [14, 15]

Cervical spine	Flexion [°]	Extension´[°]	Axial rotation [°]	Lateral bending [°]
ROM	90	70	90	20-45

2.3.1.2 Forces and moments

Some studies have been conducted to study the biomechanics of the cervical spine doing daily activities, sports, and other activities.

According to Swart et. all [15] the mechanism for an injury that has received the most attention in athletics is axial loading. Only 13% of the 209 injuries related to American football that resulted in permanent cervical quadriplegia between 1971 and 1975 resulted from hyperflexion (10%) and hyperextension (3%), while 52% were attributed to axial load.

Axial loading occurs when the head and neck are flexed to approximately 30°, as in a head-first tackle [15]. In this case, the normal lordotic curve disappears, which removes the absorbent components of the region. When contact with the helmet of a player occurs, the cervical spine experiences a compressive load from the torso. When the padding of the helmet reaches the absorptive limits, the head turns in the opposite direction, increasing the compressive load, as the cervical spine is compressed between the head and the torso. When this compressive load exceeds the absorption capacity of the cervical spine, the components of the soft and hard tissues fail [15]. The load limit on the cervical vertebrae was calculated to be 4000N, applied to the head during the first 20ms of compressive impact experiments [17]. According to the same author, compressive forces result in transient deformation during axial loading in the cervical spine, also called the buckling effect (figure 2.6. This effect is a causative element for damage, causing massive angulations within the cervical spine to release the extra strain energy generated by vertical loading. There are two types of buckling effects, first-order and second-order buckling. First-order buckling resulted in the extension of the upper cervical spine through C5 and flexion through T1. Second-order buckling created flexion of C1 through C3, extension in C4 and C5, and flexion in C6 through T1 [15].

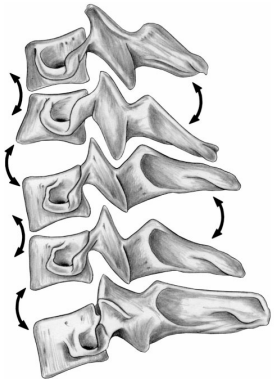

Figure 2.6: The buckling effect in the cervical spine caused by an axial load [15]

Some factors that can influence the extent of the injury or can prevent the injury as a whole. The location of the impact, on the head, is one of the factors that can influence the outcome of the player's injury. This injury is more severe when the impact occurs at the head vertex, and no injuries were shown when the impact is posterior to the vertex [15]. The use of padding in the helmet also can influence the risk of injury. In this case, on one hand, the using of padding protects the head, decreasing the risk of injury in the head, but on the other hand, the use of padding increases the resultant forces in the cervical spine, causing more severe injuries than with nonpadded impacts [15]. In most scenarios of the sport, this effect with the padding is desired to protect the head, but it can cause injuries in the cervical spine [15].

Nightingale et. all [17] did a study to examine the relative importance of mass, moment of inertia, stiffness, and loading rate in the expression of the buckling effect in the cervical spine ligament (Figure 2.6). A cervical spine model and MADYMO software were used for this effect. The cervical spine model had 7 segments, represented by hyperellipsoids, connected by rotational springs with nonlinear stiffness. These segments also had massless spinous process ellipsoids to aid in the differentiation of flexion

and extension rotation (figures 2.7). The atlanto-occipital joint was connected to an unconstrained 4.9 kg head mass with a moment of inertia. The model was subjected to a constant acceleration of $816.3\,\mathrm{m\,s^{-2}}$ to produce a force of 4000 N, applied with an eccentricity of 0.001 m, to obtain the buckling effect. The results showed that first- and second-order buckling were observed in the base model. During the first 3ms of the experiment, the force at C7-T1 showed a rapid decrease in magnitude due to second-order buckling. The transition to first-order buckling occurs 6 ms after the force was applied, and a magnitude drop follows.

Figure 2.7: Second-order buckling in the dynamically loaded ligamentous cervical spine. Images taken from [17]

In this experiment also various vertebral masses were tested, with factors of 0.125, 1.0 (baseline), and 8.0. The increase in vertebral mass and the maximum load also increased, with the following values: 3682 N, 3692 N and 3823 N for each respective factor. Using different mass inertias, with peak forces of 3682 N, 3692 N and 3830 N for a factor of 0.1, 1.0 and 10, respectively. This increase in mass of inertia did not influence the peak force as much, but when increased, the second-order buckling effect was present for a longer period of time. Changes in stiffness were tested and that affected the way the buckling effect was expressed. An increased factor of 8.0 resulted in a structurally stable column under the 4000 N load. The axial impulse for each test increased: (1) from 26.6 to 44.7 N s when the mass increased; and (2) from 27.4 to 33.6 N s when the moment of inertia increased. The large increase occurs when the mass changes, which means that understanding the behaviour of the mass in the buckling effect is important to understand the mode of injury [17].

In 2023, Barrett et al. [18], performed a computational analysis on the cervical spine to test four hypotheses: (1) the increased gravitational moment incurred from increased head-supported mass (HSM) and deviated postures will translate to increased compression due to increased muscle activity; (2) it requires more muscle activation to stabilize the vertebral column with higher magnitudes of HSM, which translates to more joint compression; (3) displacement of the HSM's COM induces a gravitational moment that translates to elevated joint compression; and (4) the increased HSM MOI necessarily increases the muscle contributions required to reposition the head rapidly. For this effect, a cervical spine model with 24 degrees of freedom was used for analysed in OpenSim 4.1 software. The model included ligaments, IVD, and muscles. Data were collected from various participants, in static postures, and in dynamic movements. The static postures were 20°of lateral bending, 30°of extension, 45°of flexion, 45°of axial rotation, or remained neutral. For the dynamic movements, the participants used a helmet with

a laser pointer and had to aim at targets that would light up, with the goal of getting as many targets as possible, and the total ROM was 70 degrees. These were the static postures and movements used in the computational analysis. The static data was used in hypotheses 1, 2, and 3. The HSM magnitude or position was varied and the resulting compression was calculated. The HSM magnitude varied from 0 to 7.74 Kg, and the position between ±25 mm in the anteroposterior and superior-inferior directions from the centre of mass of the skull. The dynamic data were used in hypotheses 1 and 4. The helmet mass was varied in the same way as in the static analysis for case 1, and for case 4 the moment of inertia was introduced, varying from 0 to 0.174 kg m2 for axial twist and 0 to 0.078 kg m2 for flexion-extension.

The results show that there is a direct linear proportionality between the magnitude of the head-supported mass and the resulting compression at C5-C6. Without stability constraints, compression ranged between 18.0 N of compression per kg of head-supported weight, in a neutral position, and 31.7 N/kg in a flexed posture (hypothesis 1). The results with stability constraints were 21.0 N/kg in a neutral position and 35.0 N/kg in extension (hypothesis 2). Linear relationships described the position of the HSM and the resulting compression, with each centimetre the position of the HSM moved anteriorly was associated with 7.5 N less compression in extension, corresponding to an increase of 4.8 N in flexion (hypothesis 3). The increase in HSM for dynamic movement had a simillar result as in the static postures, with compressions of C5-C6 ranging between 23.7 and 38.4 N for every kg of head-supported weight (hypothesis 4).

2.3.2 Cervical disc

IVDs, as previously said are fibrocartilage that is in between each vertebra. They allow vertebral column bends, twist and distribute the compressive load of vertebral plates over adjacent vertebral bodies. The mechanical properties of discs are important since the human lumbar IVD is often physically disrupted, which can lead to degenerative changes and chronic pain in the back [19]. Head weight places C2±T1 discs in some form of compression under normal physiological conditions. Under normal physiological conditions, the fundamental functional mechanical role is to react to compressive loads [20]. The internal response of IVD is influenced by the magnitude and type of load [21].

2.3.2.1 Range of movements (ROM)

The cervical disc has the same 6 degrees of freedom as the cervical spine [22]. The movements are flexion/extension, lateral bending, and axial rotation.

The upper cervical spine is composed of the atlanto-occipital joint (the joint between the atlas and the occipital bone) and the atlantoaxial joint (the joint between the atlas and the axis). According to [23] the atalanto-occipital range of motion is 3.5°of flexion, 21.0°of extension, 5.5°of lateral bending and 7.2°of axial rotation. The ROMs for identical motions in the atlantoaxial joint are 11.5°, 10.9°, 6.7°, and 38.9°, respectively.

At the junction C2-C3, the upper cervical spine meets the rest of the cervical spine (C3-C7). The ROM of each segment between C3 and C7 is shown in the following table 2.3.

In the bibliographic review, the ROM of each cervical spine disc was not widely reported, but Puttlitz et al. [22] investigated the effect of implanting a cervical disc

Table 2.3: Range of motion (mean ± standard deviation) for each segment of the cervical spine. [24]

Segment	Flexion [°]	Extension [°]	Axial Rotation [°]	Lateral bending [°]
C2/C3	3.5 ± 1.3	2.7 ± 1.0	3.3 ± 0.8	9.6 ± 1.8
C3/C4	4.3 ± 2.9	3.4 ± 2.1	5.1 ± 1.2	9.0 ± 1.9
C4/C5	5.3 ± 3.0	4.8 ± 1.9	6.8 ± 1.3	9.3 ± 1.7
C5/C6	5.5 ± 2.6	4.4 ± 2.8	5.0 ± 1.0	6.5 ± 1.5
C6/C7	3.7 ± 2.1	3.4 ± 1.9	2.9 ± 0.8	5.4 ± 1.5

prosthesis on ROM and how it changes the motion patterns of the cervical spine compared to a healthy cervical spine. Six fresh frozen human cadaver cervical spines (C2-C7) were used for this. The perispinous soft tissue was removed without altering the capsules, ligaments, or bone structures of the joint. Between the C2-C3 section, screws were drilled to provide a rigid fixation in that intervertebral space, the same was done in the C6-C7 section. The cervical spine was connected to metal potting fixtures in each of the extremities (C2-C3 and C6-C7).

The study evaluated two cervical spine conditions, with intact disc and after total disc replacement at C4–C5. For this section, the focus of the study is on the ROM of the intact disc. To the specimens, it was applied a pure moment loading, with and without compression (with a magnitude of 44N). Moments were applied in flexion and extension, lateral bending to both sides, and left and right axial rotation up to 1.0Nm after 3 cycle of preconditioning of the specimen. The results were collected at the maximum moment loading (1.0 Nm), and are presented on table 2.5.

Table 2.4: ROM (mean ± standard deviation) for the C4-C5 segment with and without compressive loading [22]

Cervical segment	Flexion/ Extension [°]	Axial Rotation [°]	Lateral bending [°]
Without compressive loading	9.4 ±2.2	13.0 ±3.6	9.9 ±2.1
With compressive loading	9.4 ±2.2	8.9 ±2.7	8.1 ±1.3

2.3.2.2 Forces and moments

For the project, it is important to know the mechanical properties of the IVD and the biomechanic response when different types of load are applied. Responses were obtained by subjecting a functional spinal unit (vertebra-disc-vertebra) or a disc segment (body-disc-body) to external loading [20]. Due to the importance of compressive load to understand the response of IVDs, studies have focused on that response. Usually, a materials testing machine applies compression loading to the superior end of the specimens while fixing them at the inferior end till failure [20] (figure 2.8).

Using the style of test shown in Figure 2.8), it was obtained by [25] the values represented in the table 2.6 where the IVD is under compression.

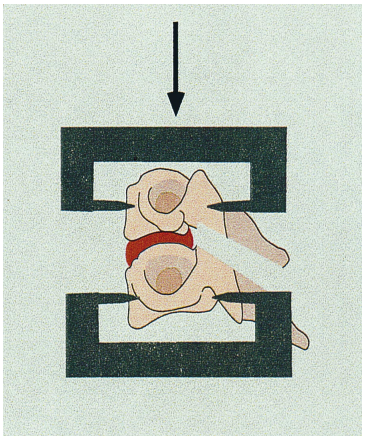

Figure 2.8: IVD compression test. Image taken from [20]

Alongside the biomechanics, the mechanical properties of each anatomical feature of IVD are important to be known for this project. Due to the lack of testing the specific mechanical properties of cervical IVD, it was used tests done on the lumbar IVD.

Starting with the mechanical properties of the AF, it was found that depending on the distance from the centre of the IVD the characteristics of the AF change, becoming stiffer and stronger in the outer AF [2]. These mechanical properties are highly anisotropic and nonlinear in uniaxial tension, compression, and shear, and have a high tensile modulus in the circumferential direction [26]. In particular, the tensile properties of the lamella can be different depending on the samples that are tested and the orientation of the tests [2]. The orientation of the fibre can be determinant for the properties of the material, and as the outer AF has the lamellas with different orientation compared to the inner AF, it can be seen in the table 2.7 the influence of that orientation.

AF has a tendency to break down and deteriorate because it is the only section of the disc that undergoes tensile stress, making these unique tensile properties an important feature in disc degeneration research [2]. Although the properties of the AF are important for a better understanding of how much stress and strain the AF can stand, most injuries occur due to cyclic loads or wear and tear of the spine, which causes the deterioration of collagen fibrils [2]. This was tested, both in the anterior and posterior sections of healthy AF, and was shown to withstand more than 10,000 cycles applied with a stress magnitude of 45% or less than its maximum tensile strength [27].

NP can tolerate compression loads because the annulus fibrosus can withstand radial forces, not tensile stresses or strains, because it is a nearly incompressible liquid [2]. The natural swell pressure of the nucleus at rest is 0.138 MPa [2]. When tested the NP is confined so it is possible to get accurate measurements, this also allows for a more accurate resemblance of the resistance towards outward deformation controlled by the AF, and the NP is not infinitely compressed [2]. In daily activities, compressive forces vary from 800 N to 3000 N, causing the NP to be pressurised up to 0.4 MPa while lying down, 1.5 MPa while standing or sitting, and up to 2.3 MPa while actively lifting [28].

Table 2.6: Biomechanical data of intervertebral disc under compression test. Values taken from [20].

Level	Force (N)	Deformation (mm)	Energy (J)	Stiffness (N/mm)
A - Under tension test				
C2-C3	636	11.4	3.70	63.5
C3-C4	636	12.1	4.41	69.8
C4-C5	571	9.3	5.50	66.8
C5-C6	391	12.7	2.64	22.0
C6-C7	505	10.0	3.32	69.0
C7-T1	535	11.3	3.28	82.2
B - Under compression test				
C2-C3	602	1.4	0.31	637.5
C3-C4	683	1.5	0.33	765.3
C4-C5	777	1.6	0.40	784.6
C5-C6	664	1.6	0.33	800.2
C6-C7	673	1.7	0.34	829.7
C7-T1	910	1.6	0.48	973.6

Table 2.7: Mechanical properties of the annulus fibrosus [2]

Tensile properties of the annulus fibrosus						
Sample	Specification	Ultimate stress, MPa	Elastic Modulus, MPa	Yield strain, %	Ultimate Strain, %	Stiffness N/m
Bulk Annulus	Outer, A	3.9 ±1.8	16.4 ±7.0	20-30	65 16	5.7 ±3.4
	Outer, P	8.6 ±4.3	61.8 ±23.2	20-30	34±11	5.7 ±3.4
	Inner	0.9	-	20-30	33	1.2 ±1.1
Single Lamella	Parallel	-	80-120	-	-	-
	Perpendicular	-	0.22	-	-	-

2.4 Cervical disc disorders

Back pain is one of the most common problems in today's society. A study in the UK estimated that in 1998, the direct cost of health care associated with back pain was approximately £1.6 billion, with a total cost of approximately £11 billion due to productivity loss [29]. Back pain can be caused by a variety of anatomical structures within the back, for example, IVD, facet joints, muscles, ligaments, and nerve root sheaths [30]. From these structures, IVD is responsible for 45% of cases of back pain [30] and for subjects older than 40 years, 62% had degenerative disc changes [31]. IVD degeneration is a natural process that occurs due to ageing, causing tissue loss or destruction over

time, reducing disc height, and ultimately jeopardising the ability of the vertebral body to operate mechanically. Evidence suggests that other factors, such as cell nutrition and transport, the presence of degradative enzymes, mechanical loading, smoking, and exposure to intense vibrations, are involved in IVD degeneration. With IVD degeneration, pain can come from the disc itself (discogenic pain) or when the degenerated disc compresses the neural structures of the spinal canal, producing radicular pain [30]. Degenerative disc diseases can be: (1) degenerative disc disease, (2) herniated nucleus pulposus, and (3) internal disc disruption. These disc degenerative diseases are the core problem of some cervical spine diseases, including cervical spondylosis, spinal stenosis, and disc herniation.

2.4.1 Degenerative disc disease

Degenerative disc disease is defined by intervertebral disc degeneration due to ageing and other environmental factors, with genetic inheritance playing a significant role in the rate of degradation [2]. Musculoskeletal tissue strength, such as that of intervertebral discs, is affected by the composition of the extracellular matrix, such as the strength of collagen fibrils throughout the annulus fibrosus, which is regulated by the individual's genetic inheritance [2]. Disc degeneration is genetically predisposed but is not widespread and common until the individual is in his 40s. The degeneracy process can begin at the age of 11 and 16 [2], and according to Rea, Kapur, and Mutagi [30] involves four stages: (1) dehydration, (2) fissuring, (3) neovascularisation, and (4) bony changes.

Disk dehydration (1) is the result of reduced proteoglycan synthesis, which also causes the loss of glycosaminoglycans, resulting in a reduction in the osmotic pressure of the IVD matrix [11, 30]. Cell concentration gradually decreases, especially in the annulus fibrosus. Matrix turnover declines and proteoglycan loss is accelerated by interleukin 1 (IL-1) and tumour necrosis factor production in response to repeated injuries.

With time, the IVD components can start to suffer from (2) fissures. AF may develop radial fissures, EP is prone to fracture under repeated loading, and NP material may leak into AF or EP. As these injuries begin to heal, a process of new vessel formation or (3) neovascularisation is associated with the AF or EP. Sensory nerve terminals proliferated alongside neovascularization and penetrated the EP and inner layers of the AF. It is beleaved that this process is key to the development of discogenic pain. Smaller injuries within the IVD and repeated small extravasations of the proinflammatory NP material lead to sensitization of nerve endings and ultimately pain. The release of inflammatory mediators from the NP to neural structures within the spinal canal is believed to underpin the development of radicular pain as a result of disc herniation 2.9.

Disc degeneration is connected with loss of disc height which alters spinal mechanics, that with time may result in (4) bony changes, such as osteophyte formation, facet joint arthropathy, and ultimately, spinal stenosis.

2.5 Cervical disc current treatments methods

There are several treatment options, both invasive (surgical) and noninvasive (nonsurgical), depending on the severity of disc degeneration and whether a disc has bulged or herniated. The most common treatment includes physical therapy, noninvasive epidural injections and pain medications, radiofrequency ablation, spinal fusion surgery, synthetic

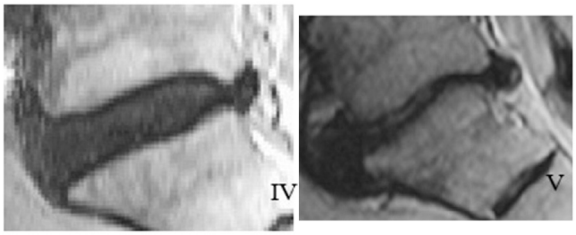

Figure 2.9: IVDs degenerate at different stages of degeneration [32].

total disc replacement, and invasive repair of annulus fibrosis [2]. In addition to these treatments, and due to their effectiveness, other treatments are researching, such as the use of stem cells, growth factors, and gene therapy with theoretical potential to prevent, slow, or even reverse disc degeneration, as well as tissue-engineered scaffolds to completely replace degenerated discs [2, 12].

2.5.1 Spinal fusion surgery

Although spinal fusion surgery (arthrodesis) is widely recognised as a useful therapeutic option for the treatment of severe degenerative disc disease, its effectiveness and success are still disputed. The principle of spinal fusion is to eliminate pain by eliminating motion [33]. This procedure is performed using anterior cervical discectomy and fusion (ACDF), in which the surgeon removes the degenerated disc through an incision along the anterior border of the sternocleidomastoid muscle to allow soft tissue dissection and annular incision [34,35]. Cloward, Robinson, and Smith first described this procedure in the 1950s [35]. The injured disc is completely removed and a titanium cage filled with osteoconductive materials, or hydroxyapatite bone graft extender, is inserted into its place between the two vertebrae [2]. The titanium plates are attached to the vertebrae above and below the titanium cage using titanium pedicle screws as fasteners to provide additional spinal support after surgery. These plates provide stability to the spine and correct the anatomic alignment of the spinal segments by sharing the loads that act on the spine, until the point where solid biological fusion occurs [2]. This is crucial because if the motion of the next segment is changed, it could induce degeneration of the adjacent discs [36].

2.5.2 Total disc replacement

Total disc replacement is a procedure that consists of removing the degenerated/injured IVD and replacing it with a synthetic disc. This type of treatment is an attractive option, with great success in achieving knee and hip replacements and serving as examples of continued research and improvements in disc replacement treatments. Although not as mainstream, this treatment offers mobility similar to the native disc, which spinal fusion surgery does not [22]. These discs are designed to maximise the ROM, inside the ROM of the native disc. The development of a cervical total disc replacement is less challenging than a lumbar total disc replacement because a lumbar disc must support extra loads compared to the cervical discs [2]. The long-term results of this treatment are still to be seen and the perspective is not the best for the long term [33].

Chapter 3

Cervical disc implants

3.1 Introduction

This chapter focuses on the types of implants available on the market, such as interbody fusion cages and artificial disc replacement, and also new experimental designs. It is necessary to understand how they work, the materials that are used and their mechanical properties, the biomechanics of each type of implant, as well as the problems and their limitations. Also, computer simulation, in vitro testing, and clinical evaluation found in the literature for some devices were studied to make it possible for comparison during the project.

3.2 Conventional Implants

There are two types of disc implants. These are divided into fusion implants and mobility implants. Interbody fusion, as the name says, fuses the two vertebrae separated by the injured disc. Mobility implants replace the injured cervical disc with an artificial disc that was designed to mimic the characteristics of the original disc. Both types of implants have advantages and disadvantages at the moment, but research is trying to make mobility implants the future.

3.2.1 Fusion or fixation implants

Since pioneering work by Cloward, Dereymaker, Smith, and Robinson employing iliac bone graft 50 years ago, the idea of cervical interbody fusion for treating degenerative and unstable disc disorders has gradually progressed [37]. According to [38], which analysed the trend in spinal fusion usage in the United States between 1998 and 2008, the frequency and use of spinal fusion had increased at a higher rate than other inpatient procedures during that time. Annual spinal fusion volume increased by 137%, while others such as hip replacement and knee replacement increased by 49.1 % and 126.8 %, respectively [38].

Although autograft is the preferred method of establishing fusion, interbody cage implants with various bone graft substitutes have replaced it as the basis of anterior cervical discectomy and fusion due to short- and long-term problems with graft harvest [39]. Historically, the creation of interbody fusion cages was made in a variety of materials and designs. Titanium, polyetheretherketone (PEEK), and carbon fibre-PEEK were

used in both threaded and non-threaded designs [35, 39]. Currently, cages are moving more to a non-threaded, wedge-shaped profile design made of PEEK or titanium alloys [35].

The fundamental design of a cage consists of a small hollow implant with lateral, upper, and/or lower windows that lead to a central cavity filled with autologous bone, allograft bone, or ingredients that induce bone growth [35]. The cage design, has mentioned, can be divided into (1) threaded (screw) or (2) non-threaded (box-shaped and vertical rings).

3.2.2 Mobility implants

An implant of an artificial disc should, ideally, be able to function as closely as possible to the native disc. This is the main focus of the present investigation regarding artificial discs.

Artificial discs should preserve normal motion at the intervertebral joint, preserving the six degrees of freedom of the native disc, in a controlled way, to prevent unstable motion. Furthermore, the artificial disc must use materials that are biocompatible. According to Kiradzhiyska et al. [40] a biomaterial is any substance or combination of substances, natural or synthetic, that can be used for a period of time, independently or as part of a system that treats, augments, or replaces any tissue, organ, or function of the body. When implanted, the artificial disc should be able to last a long time, for this is crucial the choice of materials to use. Normally, the intervertebral joint sustains 80 million motion cycles during the course of 40 years [41].

Another important feature of the artificial disc is the connection with the vertebrae. This connection is made by the endplates; these are normally made of metal and have some anchoring features, such as a keel, spikes, teeth, rails, ridges or screws to connect to the vertebras [42]. The main function is to prevent the device from moving and affecting the posterior longitudinal ligament, which protects the spinal cord [13].

Artificial discs can be classified as articulating or non-articulating according to their structure [43]. Articulating implants are composed of 2 or 3 solid discrete components that are combined in a ball-in-socket or ball-in-through configuration. These do not have a component that is capable of absorbing compressive loads, unlike non-articulating devices that have a soft core that allows compression and limits the range of motions [43].

There is another type of classification for artificial implants according to Othman et al. [43], which is based on the range of motion. There are 3 classes: constrained, semi-constrained, and unconstrained. Each class is defined in relation to the physiologic range of motion, being less than, equal to, or greater than the physiologic range of motion in constrained, semi-constrained, and unconstrained devices, respectively.

To be effective, artificial disc must meet these four requirements: (1) a solid, non-destructive interface with the adjacent vertebral bodies, (2) provide a ROM as similar as possible to the native disc, (3) resist wear and tear to minimise contamination due to debris and (4) have the ability to absorb shock and distribute loads evenly and effectively [2, 44].

In the past 30 years, there have been improvements in the artificial disc to get as close as possible to the mechanics of the native disc. The first generation design was a simple ball-and-socket or ball-and-trough joint to provide rotational capability. Second-generation designs had more degrees of freedom and had compressive and rotational

elasticity/resistivity in spinal mobilities. The more recent designs may have some degrees of viscoelasticity, impact resistance, and variable instant centre-of-rotation capabilities [13].

Currently, some IVDs are approved by the Food and Drug Administration (FDA) or CE, and others are still in the experimental phase. The devices are (1) Bryan cervical disc (figure 3.1),(2) Prodisc-C (figure 3.2), (3) Prestige cervical disc (figure 3.3), (4) M6-C artificial cervical disc (figure 3.4 and (5) CP-ESP (figure 3.5). These are the devices most encountered in the literature, they use different approaches by using various materials, each with advantages and disadvantages.

3.2.2.1 Bryan cervical disc

In the early 1990s, neurosurgeon Vincent Bryan conceived and developed the Bryan Cervical Disc. After extensive research and testing, the first Bryan Cervical Disc was implanted in Leuven, Belgium, in January 2000 [45]. This artificial cervical disc from Medtronic Sofamor DanekMemphis, TN, USA, was approved by the FDA on 12 May 2009.

Figure 3.1: Bryan cervical disc [45].

It comprises a double ball-and-socket construction with two metal-on-polymer articulating surfaces at the top and bottom of the device, allowing the ability to support rotational movements and compression [13]. Materially, it has a polyurethane inner nucleus (99% polycarbonate-urethane, 1% silicon) sandwiched between a circular titanium alloy shell (Ti-6Al-4V) on top and bottom [13, 45]. A flexible polyurethane outer sheath (94 % polyurethane urea, 6 % silicon) filled with saline and attached to the sides of the upper and lower shells by retaining rings completely enclosing the inner nucleus [13, 45]. Both of each titanium shell are coated with pure titanium beads (CP Ti B.I. Thortex K-coat) to provide porosity, facilitate bone ingrowth, and promote long-term stability [13, 45]. In addition to this coating, the shells also have a small vertical anterior lip to anchor the device to the adjacent vertebrae with a screw [13]. The interbody height of this device, which comes in five sizes with diameters ranging from 14 to 18 mm in 1 mm increments, is about 6 mm. In the following table 3.1 are the ROM specifications.

3.2.2.2 Prodisc-C

The Prodisc-C device of Synthes Inc., West Chester, PA, USA, according to a survey conducted in 2017 to evaluate surgeons' opinions on the use of cervical disc arthroplasty, was the most used device to treat cervical disc herniation [46, 47]. It was invented by

Thierry Marnay of France, based on the Prodisc-L, wich is used inlumbar arthroplasty, and in 2007 was approved by the FDA [45, 46].

Figure 3.2: Prodisc-C cervical disc [45].

It is a ball-and-socket joint (metal-on-polyethylene), 3-piece uniarticulating device with 2 endplates composed of cobalt chrome molybdenum and an articulating surface composed of ultra-high molecular weight polyethylene (UHMWPE) [45, 46]. The endplates have central keels to provide fixation to the vertebrae and are coated with plasma-sprayed titanium for better stability and bone adhesion [45]. The articulating surface is contained in the inferior end plate that articulates with the superior end plate [46]. This is a semi-constrained device.

The device comes in several sizes that range from 15-19 mm wide (medial-lateral) x 12-18 mm deep (anterior-posterior), and it is also available in three disc heights, 5, 6 and 7 mm [48].

3.2.2.3 Prestige LP cervical disc

The Prestige LP is a device from Medtronic Sofamor Danek, Memphis, TN, USA, and is the most recent evolution of the Cummins Bristol stainless steel disc after the Prestige-ST [46]. The main difference between the ST and LP models is the use of titanium in the newer model whereas the older used stainless steel.

Figure 3.3: Prestige LP cervical disc [49].

It is a two-piece ball-and-through articulating device, made of titanium ceramic composite (Titanium-6Aluminum-4Vanadium with 1% Titanium Carbide) [49]. The ball section of the mechanism is located in the implant's superior component, whereas the trough portion is found in the implant's inferior component [49]. Each part includes two rails with anti-migration teeth that are designed to press fit into two pre-drilled holes in the adjacent vertebral bodies [13, 49]. The area between the rail structures that comes into contact with the vertebrae has a commercially pure titanium (CP Ti) plasma

thermally sprayed coating, designed to stimulate bony growth [49]. The remaining surface that is also in contact with the vertebrae bodies is titanium ceramic roughened to improve fixation [13]. Finally, each component contains two anterior tab features that were designed to help with device implantation and menimize the risk of the implant going too far into the intervertebral space [49].

The device comes in several sizes that range from 5-8mm in height x 12-18mm (anterior-posterior) and is available with 15mm medial-lateral for the 5mm height disc and 17.8mm medial-lateral for the rest of the available heights [49].

3.2.2.4 M6-C artificial cervical disc

The M6-C disc according to Turkov et al. [46] is the most recent and advanced artificial disc on the market, made by Spinal Kinetics LLC, Sunnyvale, CA, USA. It was designed to mimic the anatomy and ROM of the native cervical disc, it is a one-piece with 6 degrees of freedom that move with progressive resistance [13, 46].

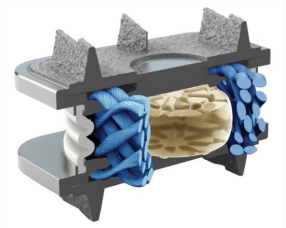

Figure 3.4: M6-C cervical disc [13].

It is composed of a compressible polycarbonate urethane (PCU) inner core that replicates the NP, surrounded by UHMWPE fibres wound in a specific pattern that mimics AF fibres [46, 50]. Fibres also go through slots in the two titanium alloy (Ti6Al4V) inner EP, that is in contact with the NP but not attached to them [50]. Two outer EPs that are welded to the inner EPs, have low profile fins and are coated with titanium plasma spray to increase contact area and bone cell adhesion (osseointegration) [13, 50]. This artificial disc also has a polymer (PCU) sheath surrounding the inner core fixed by two Ti6Al4V weld bands, to prevent debris from leaking outside of the core and to prevent tissue growth into the core [13, 46].

The M6-C cervical disc specifications can be seen in Table 3.3. Size-wise it comes in 4 width x depth combinations (15x12.5mm, 15x15mm, 17x14mm and 17x16mm) and 2 heights (6mm and 7mm) [50].

3.2.2.5 CP-ESP cervical disc prosthesis

The ESP has been in development for the past 20 years, by Spine Innovations (France) and is currently available with cervical and lumbar disc prostheses. The biggest problem faced in disc development was how to bond the elastic component and the titanium endplates [51]. When solved, it gained CE approval in 2005 for the lumbar disc, and in 2012 for the cervical disc [51].

CP-ESP is a six-degree-of-freedom elastomeric one-piece intervertebral prosthesis. It is a single-piece deformable implant with a polycarbonate urethane (PCU) core that is firmly attached to titanium endplates (TiAl4V) [13, 51]. The endplates have anchoring

Figure 3.5: CP-ESP cervical disc [52].

pegs to add fixation, and are coated with a texture titanium layer (T40) and hydroxyapatite to promote bone growth [51]. The titanium endplates and the core are joined through adhesion moulding, which uses a peripheral groove to enhance the bond without the need for glue [51]. The internal surfaces of the endplates have supplementary "male" and "female" pegs that stabilise the PCU annulus [51]. The shape of the cushion, together with the location of the pegs, control the translation, shear movements during cervical spine mobility, and helps to control compression and translation [13, 51].

The prostheses are available in three thicknesses (5, 6 and 7 mm), each with three sizes in AP and lateral dimensions (13 mm x 15 mm, 14 mm x 17 mm and 15 mm x 20 mm) making a total of 9 combinations [51]. In the following table (3.4 and 3.5) is the ROM and mechanical properties of this disc.

3.2.3 Problems and limitations

Although already in commercial use, and with positive results both types of implants previously mentioned, there are problems and limitations.

3.2.3.1 Fusion or fixation implants

The use of interbody fusion implants has shown good results in the treatment of degenerative disc diseases. A study from [53] found a successful rate of 98% arthrodesis for one-level BAK/C [54]. However, these types of devices are not perfect and have problems that can favour the use of treatment. The main problem is in the possible degeneration of adjacent segments, in the long term, due to the elimination of motion between the vertebrae [2, 55]. When the vertebrae fuse, there cease to exist motion and the load absorbing centre of the NP, which increases the loads and stress concentration on the surrounding discs and tissues [2, 55]. Degeneration of the adjacent discs can lead to the need for treatment caused by the use of the interbody fusion cage.

Due to these serious drawbacks, surgeons tend to use arthroplasty as a more advanced solution [12].

3.2.3.2 Mobility implants

Mobility implants are the future of IVD repair; however, they have some drawbacks that are being addressed to improve the capabilities of these implants. The main drawback of total disc replacement is the wear and tear of the implant [43], but other problems can occur, such as fixation to the bone and anchorage that can produce an inflammatory reaction that causes pain [12].

Aseptic loosening caused by wear is the most common cause of implant failure [43]. The wear of the implant, causes debris to deposit in the surrounding of the implant, inducing an inflammatory response that mimics foreign body reaction with formation of granulomas and resorption of bone causing the implant to loosen [43].

In addition, the long-term effectiveness of arthroplasty procedures is not well established, has the survival and integrity of the implants.

Disc replacement implants, biomechanically still do not replicate all the way the physiologic spinal motion or stability and there is still a lack of proof that is a method that can suit all patients [55]. Ball-and-socket designs give way to the potential for motion segment hypermobility, increased wear debris, and stress concentration within the bearing itself, all of which result in higher forces acting on the vertebrae [2]. These designs, also show a lack of shock absorption ability [2]. One-piece designs, although having shock absorption capabilities from the elastomer core, this core suffer from a greater chance of material tears either within the material or at the adhesion interface between the different materials [2].

3.3 Non-conventional implants

The term non-conventional implants here is applied, as a type of implant that is different due to the use of new technology, is a completely new concept, or is a scaffold for IVD tissue engineering.

With this in mind, some of these implants are being tested to be used in the future, and some of them are just computational experiments.

3.3.1 Experimental device made from PHEMA/PMMA hydrogel composite from Antonio Gloria et al.

Antonio Gloria et al. [56], developed an alternative design to mimic the native IVD structure. The disc is composed of polyethylene terephthalate (PET) fibres, wounded helically on a mandrel until the final size of the IVD was obtained (in the centre of the disc space for the NP was left). The winding had a variable angle between 45 and 65 mimicking the AF structure of the natural IVD. The wound fibres, after winding, were tranfered to a pseudoelliptically shaped Teflon mould and filled with within the poly (2-hydroxyethyl methacrylate)/polymethyl methacrylate (PHEMA/PMMA) 80/20 w/w chemically cross-linked hydrogel. During this process hydroxyapatite (30% w/w) reinforcing hydrogel was added to form the endplates figure 3.6 (B).

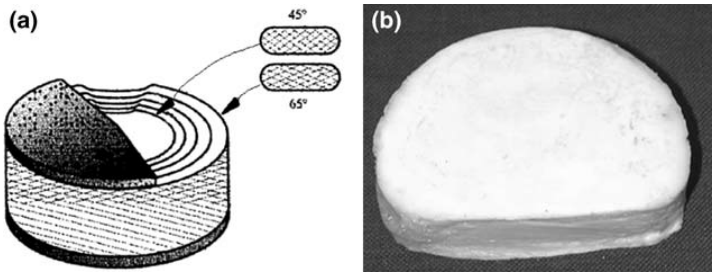

Figure 3.6: (A) The schematic representation of the fibre orientation, and the hydroxyapatite reinforcing hydrogel endplates (B) The final prototype of the IVD [56].

3.3.2 Intervertebral disc for Cervical spondylosis composed of seeded biomaterials by Mariana Vasquez-Alvarez et al.

This disc from Mariana Vasquez-Alvarez et al. [57] aims to solve the biomechanical and mechanical problems mentioned above in 3.2.3, which artificial IVDs currently available on the market have. The design and dimensions were based on images of a native IVD to better emulate the geometry and, consequently, the range of motion. The diameter of the upper and lower disc faces varies between 10-18 mm when estimating the AP distance and 10.33-22.91 mm when estimating the distance from the centre to the end of the end plate.

The disc (figure 3.7) consists of (A) two endplates that enclose the disc and interface with adjacent vertebrae made of, (B) the nucleus pulposus that has shock absorbing capabilities and (C) the annulus fibrosus responsible for maintaining the integrity of the disc during flexion, compression, extension and torsion movements.

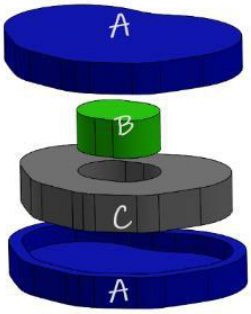

Figure 3.7: Cervical disc developed by Vasquez-Alvarez et al. [57]. (A) endplates, (B) nucleus pulposus, (c) annulus fibrosus.

Regarding material, the author [57] tried to obtain the best materials for each component. The annulus fibrosus is made up of carbon fibre called Hexcel Magnemite (PAN-based PV42-850) due to its good mechanical properties. The nucleus pulposus is made of hyaluronic acid hydrogel with methylcellulose loaded with mesenchymal stem cells because it has good swelling capacity and biocompatibility and improves the viability of nucleus pulposus cells while decreasing the degradation of ECM. Endplates are made of acellular porous polycaprolactone (PCL), mainly because of their ability to integrate with osseous tissue.

3.3.3 NeoDisc cervical disc

The Neodisc (Figuere 3.8) is an artificial IVD developed by Health Innovation Support (UK) and later sold to NuVasive, Inc., San Diego, CA [13]. It consists of a core of solid silicone elastomers surrounded by embroidered polyester fibre jackets [58]. The jacket contains two flanges that are attached to the two adjacent vertebrae with four titanium bone screws [58]. Long-term fixation is expected, due to the use of the jacket material, which is known to stimulate soft tissue growth [13, 58]. This jacket is a piece of fabric produced by a computer-controlled embroidery process [58]. The two flanges of the jacket are connected with each other by passing the superior flange through the inferior, and during extension/flexion movement are pulled in opposite directions, transferring a compressive load through the silicon core [58].

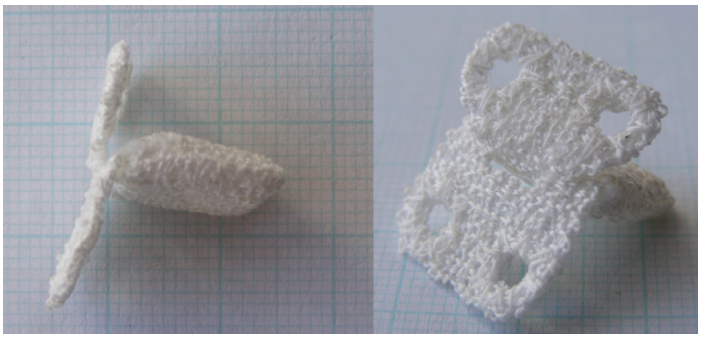

Figure 3.8: Cervical disc NeoDisc made from a computer-controlled polyester fibre from the embroidery process. The image was taken from [59].

This is a non-conventional that goes in a different direction regarding the design when compared with all the others previously presented. The NeoDisc does not use endplates and bone growth is based on soft tissue ingrowth on its polyester fabric material instead of ossification.

3.4 Biomechanics and clinical studies of IVD implants

Besides understanding, the designs/concepts and materials used for all types of implants mentioned above, conventional or non-conventional, it is also important to search for available proof of biomechanical testing. These tests include clinical studies, in vitro studies, and computational studies found during this research.

3.4.1 Neodisc

In 2010, a study carried out by [60], tested the clinical and radiographic outcome of the Neodisc cervical total disc replacement at a 2-year follow-up. The study was carried out in 61 patients, 30 who received the NeoDisc implant, and a control group of 31 who received an ACDF. The success of the experiment was defined as a score greater than 15 points improvement in the neck disability index (NDI). At each pro-operative and follow-up visit, visual analogue scale (VAS), NDI, patient satisfaction, and flexion/extension radiographs were evaluated.

NDI success was achieved in 72% of control patients and 89.3% of the NeoDisc patients (P>0.027). The average pre-operative NDI was 64.3 in the control group and 69 in the NeoDisc group. The average two-year post-operative NDI was 40 in the control group and 24 in the NeoDisc group (P<0.018). ROM in the pre-operative period, for the Neodisc group, was 10.7°, 8.4°at six months of follow-up and 8.2°at two years of follow-up.

FDA IDE trials for NeoDisc by NuVasive were terminated for unknown reasons [42].

3.4.2 Bryan cervical disc

Summarised results of the FDA approval of the Bryan cervical disc.

Table 3.1: Full range of motion ex vivo - for all prosthesis sizes [61].

Flexion/ Extension [°]	Lateral Bending [°]	Axial Rotation [°]	Translation [mm]
±10	±11	±7	±1

Table 3.2: Compressive loads on the Bryan cervical disc [61].

Avarege [N]	Maximum [N]
130	1164

3.4.3 M6-C artificial cervical disc

Summarised results of the FDA approval of the M6-C cervical disc.

Table 3.3: Mechanical testing in the FDA Summary of Safety and Effectiveness Data for the M6-C [50].

Test Name	Acceptance Criteria	Results
Static Axial Compression	Ultimate load 3.2kN	No failure could be achieved to approximately 25kN
Static Compression-shear	Ultimate load 845N	The average load at failure (including a full extension angle of 7.5) was 6714 113N.
Static Torsion	Ultimate load 4 Nm.	The maximum torque was 10.26 ± 1.23 Nm.

3.4.4 CP-ESP cervical disc prosthesis

Summarised results of in-vitro studies of the CP-ESP [51].

Table 3.4: Full ROM of the cervical disc CP-ESP [51].

Flexion/ Extension [°]	Lateral Bending [°]	Axial Rotation [°]	Translation [mm]
±14	±12	±8	±0.8

Table 3.5: Mechanical properties of the CP-ESP disc [51].

Stiffness for compression	733 N/mm
Moment for extension	0.03 Nm/1°
Moment for flexion	0.03 Nm/1°
Moment for lateral bending	0.05 Nm/1°
Moment for rotation	0.24 Nm/1°

3.4.5 Experimental device made from PHEMA/PMMA hydrogel composite from Antonio Gloria et al.

The authors who created the disc [56] tested the compressive properties of the device. The test was carried out at different strain rates, ranging from 1 to 10 mm/min. Engineering stress and strain were evaluated, and compressive moduli were calculated. Compressive tests were performed on hydrated samples with PBS aT 37°C. A stress of 2MPa was applied and the strain was monitored for 4,500s.

The static compressive tests were conducted to a load of 17000N. The findings revealed a strain-stress curve that remained constant until a strain of 0.09mm/mm was achieved., and the strain-stress curve became linear. This constant part of the curve was due to the properties of the fibres, which straighten their crimped waveform and reorient themselves in the transverse direction. The compressive modulus for this artificial disc was 84.0 ±9.8, 102.0 ±9.8 and 120 ±12.0 for 1, 5 and 10 mm/min, of strain rates respectively.

3.4.6 Intervertebral disc for Cervical spondylosis composed of seeded biomaterials by Mariana Vasquez-Alvarez et al.

Mariana Vasquez-Alvarez et al. [57] after developing the artificial IVD performed computational studies to understand the behaviour and loads that the disc can withstand. Two static conditions were evaluated: (1) compression and bending on the lateral sides and (2) compression and bending back and forth.

For the boundary conditions, the IVD was fixed in the inferior face. A load of 80 N was applied to the upper face, simulating the weight of the average head, and a safety factor of 1.6 was used to compensate for the uncertainties of the load. The model was evaluated by the author using SolidWorks. The size of each element, in the mesh, was 0.202 mm and 99. 9% of the elements used had an aspect ratio less than 3.

The result obtained for both conditions was compression, displacement and safety stress, and can be consulted in the following table 3.6.

From the values of the safety factor that were greater than 1, the author concluded that the device supported the conditions without failure.

Table 3.6: Results of the computational simulation on the two static conditions: (1) compression and bending on the lateral sides and (2) compression and bending back and forth [57].

Stactic Condition	Principal stress at compression	Total displacement	Safety factor		
			EP	NP	AF
1	7.4 MPa	-	13.63	2.58	523
2	1.0 MPa	Critical 0.004 mm	10.89	2.13	407

3.4.6.1 Development of a Finite Element Model of the Cervical Spine and Validation of a Functional Spinal Unit

Silva et al. [62] developed a finite element model of the cervical spine, to understand the mechanics of the neck by creating a new finite element model of the human cervical spine that accurately represents most of its components.

The geometry of the cervical spine was obtained using computer tomography scans (CT-scan) of a 46-year-old female. The team doing the study sectioned the model from the CT scan and the result was a functional spine unit consisting of the C6-C7 segment. The segment was simulated, using computational simulation. The finite element modelling was made using hexahedral elements, with a size variation between 0.5 (IVD) and 0.6 (vertebrae) mm. The disc (an interesting part of this study to this project) was divided into the different components of the IVD, AF, NP and endplates and the ligaments presented in the segment studied were also included. The material properties were defined with values from published literature, assuming all the components as isotropic with linear elastic properties. The boundary conditions were set to simulate the segment during flexion, extension, lateral bending, and axial rotation. For this, the bottom vertebra was restricted in all degrees of freedom and the top was defined in order to allow the previously described movements. The segment was subjected to six moments of pure moments of 1 Nm to perform the movements, and the ROM was monitored.

With these conditions, the ROM during the simulation flexion was 2.03°, extension 2.53°, left rotation 1.95°, right rotation 1.75°, left bending 1.32°and right bending 1.14°. The study concluded that the face joints and the ligaments play a major role in limiting the movements of the spine.

Chapter 4

Processes and biomaterials applied to implant manufacturing

4.1 Introduction

This chapter provides an overview of the biomaterials that can be used in this project, as well as the method of fabrication of artificial IVD.

First, was the analysis of different types of fibres and hydrogels to better understand how they are used and the mechanical properties of each. Second, there is the production method of the fibres for the AF and the hydrogels for the NP. These factors are important for the choice of materials to use in the fabrication of the final artificial IVD.

4.2 Biomaterials

According to [40] by definition, a biomaterial is any substance (other than a drug) or a combination of substances, natural or synthetic, that can be used for a period of time, independently or as part of a system that treats, augments, or replaces any tissue, organ, or function of the body. Materials for implant manufacturing must have several properties that do not change after long periods of contact with a biological environment. This means that the material cannot cause cell death, chronic inflammation, or damage the function of cells [40].

The choice of materials to use in an implant is not easy to do, in addition to being able to comply with the requirements of biomaterials, the mechanical properties of the material, such as tensile strength, Young's modulus hardness, elasticity, and density, are also essential because these parameters influence the capabilities of the implants. According to their nature, biomaterials can be classified as polymers, ceramic materials, metals, and composites [40].

In the fabrication of artificial IVD, the most widely used biomaterials are polymers and metals. In the proposal for this project, the goal is to use polymeric fibres to mimic the AF structure, and hydrogels to mimic the NP and titanium for the endplates, and that is the focus of this bibliographic review. As said by [63] the mechanical characteristics of a tissue engineering polymer should ideally be suited to mimic the regenerating tissue, providing the closest environment to the native ECM. As previously seen in Chapter 3, these two types of materials are used due to the mechanical capabilities and the

acceptance they achieve within the human body.

Polymers are considered to be one of the most suitable materials for use in medicine and tissue engineering because of the numerous technological possibilities for production. Some types of polymers can degrade inside the human body and eventually be eliminated. Besides this, the production of polymers holds numerous technological possibilities, presenting a wide array of opportunities for innovation and advancement [40].

There are two types of polymers, natural and synthetic. Natural polymers are more attractive for medical and tissue engineering due to their lower cost, availability, and the fact that most of them are non-toxic [64]. Natural polymers, derived from biological systems including microorganisms, plants, and animals [65]. This type of polymer has pros and cons. Pros such as resemblance to host tissue, communication capabilities with biological systems, metabolic compatibility, non-toxicity, minimal inflammatory reactions, enzymatic degradation, and utilization of degradation products in cellular metabolism are among the notable attributes of natural polymers. On the contrary, they are sensitive to temperature, which often leads to decomposition prior to reaching the melting point, and their complex structure makes it difficult to process [65]. Examples of natural polymers are chitosan, gelatin, collagen, alginate, and agarose.

Synthetic polymers are used in orthopaedics, dental medicine and tissue replacements, and are obtained by the polymerization of monomers. The mechanical and chemical properties of these polymers, are easily controllable, allowing for customization. The production can be low-cost, the availability is high and often exhibit non-toxic characteristics. Additionally, their processing can be conducted under mild conditions that are compatible with cellular environments [66]. PLA and derivatives, PEG, PU and PCL are some examples of synthetic polymers and these are approved by the Food and Drug Administration [63].

4.2.1 Fibres

According to [12] there are several research groups that have used the electrospinning approach to fabricate and assemble nanofiber scaffolds as a potential for tissue engineering for AF. These studies have had various success levels, but the progression from these studies to the actual implementation has not yet occurred. So there are still different concepts and approaches that need to be tested, as well as different materials that can be used. Currently, there is no common opinion about the materials to be used or the techniques to be performed in order to facilitate the patient's life.

The different teams used the following materials to produce fibres: PCL, PLLA and PCL with PU. PCL is the most common material used for biodegradable scaffolds [67]. In addition to the material, fibre alignment also influences the mechanical properties of scaffolds. According to [67] comparing the stress and Young's modulus of the randomly orientated and orientated PCL fibres scaffolds, both parameters are higher in the case of orientated fibres, so the mechanical properties of the scaffold are related not only to the material used but also to the orientation of the fibre. No single polymer has proved to be the optimal scaffold for AF tissue regeneration [12]. So to overcome this a blend between fibres is being studied to meet the properties mechanical properties of the IVD. According to two studies, [12,67] and the blend between PCL and PLLA can improve the mechanical performance of scaffolds and meet the requirements of the AF. This study proved that this mixture of materials did not affect the degradability of the materials.

4.2.1.1 PCL

PCL, a polyester known for its biocompatibility, bioabsorbable nature, and biodegradability, finds diverse applications in the medical field. It is utilized as a material for medical implants, dental splints, and targeted drug delivery systems. Additionally, PCL plays a significant role in tissue engineering, contributing to the development of innovative solutions [65]. Ensuring satisfactory mechanical properties is a crucial requirement for the utilization of electrospun nanofibrous scaffolds in biomedical applications.

Several studies were researched in order to find more about the mechanical properties of the PCL electrospun fibres.

Mechanical testing of electrospun PCL fibres was made by [68]. The PCL solution was electrospun for 25 minutes, resulting in the formation of fibre scaffolds. During the electrospinning, the fibres were not oriented at any point. These scaffolds were then cut into rectangular samples measuring 3 x 0.5 cm using scissors and a cardboard pattern as a guide. Macro-tensile measurements were conducted using an electromechanical tensile tester with the samples mounted between holders at a 1 cm distance. The test and was performed at a rate of 5 mm/min at room temperature. The mean Young modulus for different fibre diameters was 3.8±0.8MPa and the mean strain break was at 170±10%.

Another study was made by [69], with the goal of developing for the first time a chemically graded laminate porous device composed of a PLA-based core and a PCL-based shell in the form of a monolith. In this work a PCL-only sample was made and tested, being the one of interest to the ongoing project. The PCL samples had a 3mm in height. A morphological analysis of the sample in the scanning electron microscopy was made. The samples were mechanically tested to compressive load and tensile load at a rate of 1mm/min with a 1kN load cell. The tensile test results revealed that Young's modulus of the PCL samples was approximately 19 MPa. Additionally, at a compression test, Young's modulus was found to be around 7 MPa.

[70] did a master's thesis to study different types of scaffold geometries using PCL electrospun fibres. Samples of three different geometries, each with different electrospinning parameters that would change the properties of the scaffold. All the different samples are mechanically tested to compression. The results for compression would vary between 0.15 and 0.9 MPa.

4.2.2 Hydrogels

Hydrogels are three-dimensional network polymers, characterized by their hydrophilic structure, with the remarkable ability to absorb water up to thousands of times their dry weight [71]. Moreover, hydrogels offer exceptional versatility, as their physical properties such as degradability, mechanical strength, gelation time, and gelation temperature can be easily modified. They can be prepared through either physical crosslinking, which involves hydrophobic interactions, hydrogen bonding, electrostatic forces, and similar mechanisms, or through chemical crosslinking, which relies on covalent bonding [72]. The distinctive characteristics have led to their extensive utilization in various fields, including contact lens manufacturing, cell encapsulation, drug delivery systems, and scaffold fabrication [71].

Because of the ability to absorb, and retain water and easily tunable mechanical properties, hydrogels make an ideal candidate to mimic the NP.

As hydrogels are polymeric materials, as previously said, they can be classified by their origin, as natural or synthetic.

Natural hydrogels are hydrogels formed by natural polymers. As previously said, these type of polymers comes from natural resources, with high availability. Despite the good biodegradability and biocompatibility, these types of hydrogels often are not able to meet the mechanical requirements to be used in all applications [71]. Several natural hydrogels, such as alginate, collagen, chitosan, hyaluronic acid, and agarose, have been used in the mimicking of the native NP.

Alginate is a polymer extracted from algae, it has high biocompatibility and low cytotoxicity. The application of alginate hydrogel in mimicking the NP is restricted due to challenges associated with its uncontrollable gelation process. When in the gelation process the boundaries tend to tends to form tight bonds, resulting in a loss of homogeneity within the hydrogel structure, which results in mechanically weak hydrogel [71]. Usually this alginate hydrogel are combined with other polymers.

Collagen, a crucial component of the extracellular matrix, and found in the composition of the NP, is a naturally occurring biological material that is widely distributed in various tissues such as skin, bone, cartilage, blood vessels, teeth, and tendons. It is biocompatible, biodegradable, and minimally stimulates the immune system [65, 73]. It has the ability to resemble the behaviour of the NP. In most cases this hydrogel require other biomaterial to to improve their applications in mimicking the NP [73].

Chitosan, a cationic polymer derived from chitin, is abundantly found in the exoskeletons and wings of arthropods. It possesses remarkable biodegradability, biocompatibility, antibacterial properties. Due to its abundant hydroxyl and amino groups, chitosan exhibits exceptional water absorption properties, making it an ideal material for hydrogel preparation [71, 73]. Biomechanical aplications of this hydrogel is limitted due to the relative long gelation time [71].

Agarose is a polysaccharide composed of monomers consisting of D-galactose and 3,6-anhydro-l-galactose, extracted from algae and it has none to a small immunological responses [73]. These hydrogel can be produced with a 3D spiral structure when mixed with water, and is commonly used to mimick NP, alongside a synthetic electrospinning polymer that mimicks the AF.

Synthetic hydrogels, are made from synthetic polymers. Typically they have better mechanical properties, lower batch to batch variations better water absorption, durability, and tunability but poor biocompatibility and potential cytotoxicity, when compared with natural hydrogels [71]. Examples of synthetic hydrogels are poly(ethylene glycol) (PEG) mand polyurethane (PU).

PEG is a biocompatible, nonimmunogenicity, degradable, and modifiable polymer that is most commonly used in wound healing and drug delivery. It has been reaserched to be used in the IVD regeneration as a non-toxic hydrogel crosslinker [71].

PU is composed by hydroxyl and isocyanate groups. It can react with hydrogen compounds and present its capability for tissue adhesion, are generally biodegradable and applied for cartilage repair [71, 73].

4.3 Fabrication process

As previously said in section 2.2.2 the AF comprises 15-25 concentric fibrous lamellae surrounding the NP. To replicate the structural fibrous architecture of the native AF, it is necessary that the artificial AF also has a fibrous structure. Electrospinning is a technique used in biomaterials and regenerative medicine that produces nanofibers subtracted that can mimic the architecture of the extracellular matrix [12, 74]. Using this method, it can be possible to replicate the fibrous structure of the AF.

Looking at the constitution of NP given in section 2.2, it is mainly composed of proteoglycan, water, and Type II collagen. A good initial substitute is a hydrogel, which is widely used in nucleus pulposus regeneration and repair [72].

4.3.1 3D electrospinning

Electrospinning is a versatile and simple technology that uses high voltage to pull micro- and nanofibers from polymer solutions [74]. By tuning the electrospinning parameters as well as the properties of the polymer solution, one can have a large degree of control over the shape and morphology of the fibres [74]: diameter, length, surface roughness, porosity, pore interconnectivity, degree of fibre alignment, beads-in-fibres.

The core of a 3D electrospinning system is a high voltage electrostatic generator, metal collector, syringe pump, and needle or nozzle [67]. The electrospinning process is initiated by a polymer solution being pumped through the tip of an electrically charged needle/nozzle to form a droplet, the electrical potential of the nozzle increases until the electrical forces exceed the surface tension of the liquid droplet, deforming into a cone, called the "Taylor cone" [75]. The resulting imbalance of these forces causes the jet to launch from liquid droplets and travel through the air gap in an electric field. During flight, as it moves toward the grounded collector surface, the solvent in the liquid jet evaporates as the liquid jet dries, leaving a solid polymer fibre [12].

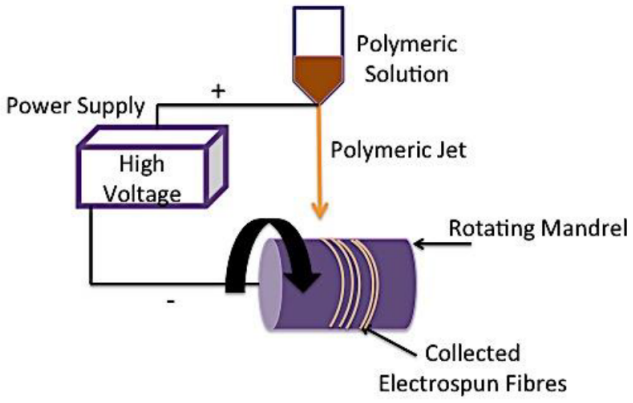

Figure 4.1: Diagram of electrospinning system. Taken from [12]

4.3.2 Hydrogel preparation

After the research about the types of hydrogels available, it was decided to investigate more about agarose and alginate hydrogels, to then do an experimental phase with them and try to reach the best result possible since it was unclear what was the best way to process in relation to the hydrogel choice. The description of the hydrogel base solution and the mechanical properties found in the bibliography is described below.

4.3.2.1 Agarose

Lazebnik et al. [76] did an experiment combining the fabrication of an artificial IVD using agarose as mimicking the NP. The author dissolved agarose in boiling phosphate buffered saline (PBS) at 2% (w/v) solution. The solution was continuously stirred until the dissolution of agarose. Then the mixture was poured into moulds and tested. This solution had the addiction of P1 chondrocytes but for this project that part was not necessary.

The samples were compressed to test the mechanical properties. Before testing, the samples were hydrated in PBS for 24h. The test was performed in a PBS bath at 37 ºC. It applied a load until 20% strain at a rate of 1%/min.

Another study made by Buckley et al. [77] used a different agarose preparation with different concentrations. Agarose was mixed with PBS and autoclaved at 121ºC at four concentrations 2%, 3%, 4% and 6% (w/v). The agarose was poured into moulds to be mechanically tested. The samples were left to cool at room temperature and then divided into 3 test groups: (1) samples maintained overnight at room temperature and tested at room temperature (2) samples maintained overnight at 37 C, allowed to cool for 60 min prior to testing at room temperature (3) samples maintained overnight at 37 C and tested at 37 C. For comparison to this project, only case study 1 was relevant.

The mechanical properties of the samples were evaluated using a 5 N load cell in combination with a PBS bath. Stress relaxation tests were conducted, involving a ramp and hold cycle with a displacement ramp rate of 0.001 mm/s until a 10% strain was achieved. This strain level was maintained until equilibrium was reached. The compressive equilibrium modulus was determined by dividing the stress measured at complete force relaxation by the applied strain.

The test retrieved an equilibrium modulus, for compressive tests around 18 kPa for 2% agarose, 45 kPa for 4% agarose, and 90 kPa for 6% agarose. In this case, the higher the agarose concentration, the higher the equilibrium modulus.

4.3.2.2 Alginate

A study by Kaklamani [78], to characterise the gelation time and Young's modulus of agarose hydrogel was carried out using different cations Mg2 +, Ca2 + and Sr2 + to promote gelation.

Hydrogels were prepared using an external gelation method. Aqueous sodium alginate solution was poured into a poly(styrene) mould with specific dimensions and a liquid height of 6 mm. The gelation process occurred in the presence of an aqueous solution of cation chloride, which was held at the upper and lower boundaries by porous microcellulose sheets. Stainless steel cylindrical spacers were placed at regular intervals along the inner edge of the mould to support the upper sheet. The required volume

of the aqueous sodium alginate solution was 81.75 mL. A polystyrene support, filled with water, was used to hold the upper sheet in place, ensuring close contact between the upper sheet and the sodium alginate solution to prevent shrinkage at the sample edges. The dissolution of sodium alginate powder in water was performed under agitated conditions at a temperature of 70°C. Sodium alginate solutions with concentrations ranging from 2.5% to 5.0% (w/v) were prepared. Aqueous cation chloride solutions with concentrations between 1 M and 5 M were created by gradually dissolving the cation chloride powder in water under agitation at room temperature. Microcellulose sheets were trimmed to match the shape of the poly (styrene) mould and immersed in aqueous chloride solutions before use. The gelation of the samples occurred at a temperature of 18 ° C for up to 60 minutes.

The mechanical properties of the hydrogels were evaluated using spherical indentation, using a 5N load cell. Force-displacement data were recorded at a crosshead velocity of 0.1 mm/s for indentations with depths less than 50 μm.

Among the solutions tested, the one with 5% (w/v) alginate concentration and Ca2+ as the gelation agent exhibited the highest Young's modulus. Young's modulus was approximately 550000 Pa for the 5M Ca2+ solution, 400000 Pa for the 2M Ca2+ solution, and 250000 Pa for the 1M Ca2+ solution.

Intentionally blank page.

Chapter 5

Design and fabrication of cervical disc

5.1 Introduction

This chapter describes the design of the artificial cervical disc, the production methods, mechanical characterisation and, finally, the results. The approach taken was to describe the design and the computational analysis of each design. It concluded with the results and discussion of this first phase. Then, the fabrication process, along with the processes involved and the mechanical characterisation were developed. Finally, the presentations of the results followed by a discussion in which the results are compared with the native IVD, along with the artificial discs previously mentioned, and the results from the computational analysis.

5.2 Cervical disc design and simulation

5.2.1 Introduction

Concept generation and 3D modelling followed the initial research. Starting with concept generation based on the anatomy of the native IVD. The concept was 3D modelled using CAD software *SolidWorks*. A mimic of the cervical IVD was made based on the dimensions and areas of the native IVD. From this first model, several iterations were tested using computational simulation. To improve the performance of the disc, different parameters were tested in the numerical models. Three different parameters were tested: (1) the use of different areas of the artificial annulus fibrosus; (2) the use or not of a pocket on the endplates to contain and protect the core; and to understand how the material properties would affect each component, (3) use of different values for the mechanical properties. All models were simulated using *3DEXPERIENCE SIMULIA*. A discussion of the results followed.

5.2.2 Materials and methods

5.2.2.1 Concept generation and 3D modelling

The project is based on the fabrication of an artificial IVD using 3D electrospinning for the AF and the use of a hydrogel for the NP to mimic the native IVD. For this

purpose, the concept had to have the three fundamental features of the native IVD: an artificial nucleus pulposus, an artificial annulus fibrosus, and two endplates (Figure 5.1). The design is "D-shaped", mimicking the general shape of the native IVD. The core is also shaped as NP in the native IVD. To encapsulate the two previous structures and provide better bone adhesion, two endplates at the top and bottom of the disc were included. With the general idea of how the disc would look like, the next step was to use *SolidWorks* to 3D model the disc.

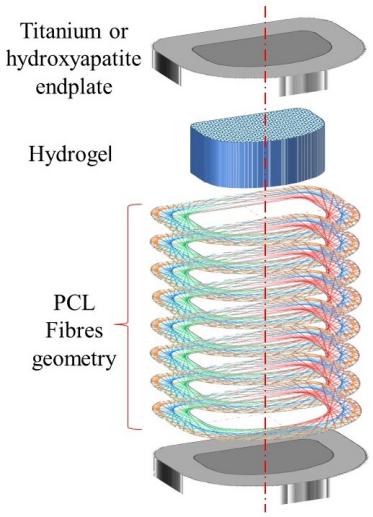

Figure 5.1: Idealized concept for the artificial disc fabrication.

The first model (Figure 5.2) was made based on the dimensions and areas of the native IVD of Table 2.1, as well as, the study of conventional and non-conventional implants mentioned in Chapter 3. The artificial IVD had the following dimensions: 17.1 mm in width, 14,1 mm in depth, and 7 mm in height. Taking into consideration the bone removal to place the artificial disc during surgery the height of the disc was greater than the native IVD. The endplates were 2mm in height. The artificial nucleus pulpous (ANP) was 3mm high, had an area of 78.7 mm^2 and was surrounded by the artificial annulus fibrosus (AAF). The AAF had 3mm in height and an area of 132,6 mm^2. Adding the two previous areas, the disc had an area of 211.3 mm^2, which was in the range of areas for cervical native IVD seen in Table 2.1. In Figure 5.2 all the components of the disc are shown.

Since the goal was to make an artificial disc that can fit a wide range of people, these models will have different sizes in all previous dimensions. Still, for testing and fabrication of the disc, these were the chosen dimensions.

With the concept modelled, two more iterations were made to test the different configurations of the components. For better understanding, each iteration will have a designation to be easily identified.

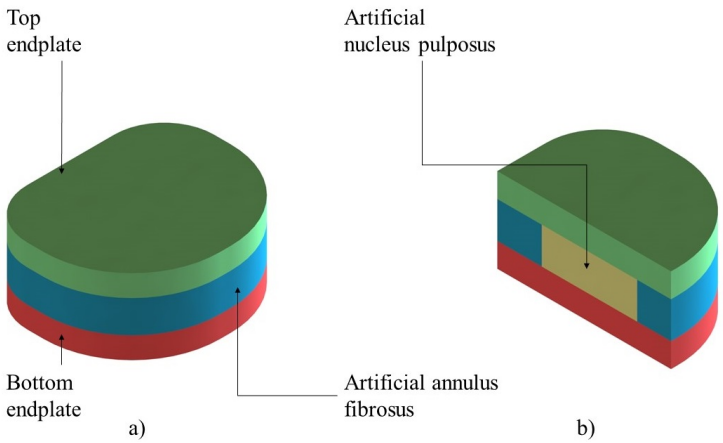

Figure 5.2: Model designed in SolidWorks. On the left side, a) an isometric view of the artificial disc with the components identified, and on the right side b) the model cut to show the ANP.

In the first iteration, the cross-sectional area of the AAF was increased, to understand the effect that the area of the AAF has on the overall design of the disc. This increase in area forced the ANP area to be reduced since the overall area was not changed. The area of the AAF was increased by creating an offset of 1mm in its geometry. The increment was from 132,6 mm^2 to 162,6 mm^2 (Figure 5.3). The designation for this iteration was G_AAF_B. Here, AAF represents the modified component, and B denotes a bigger area.

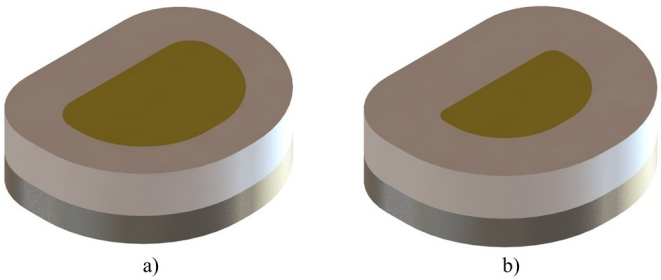

Figure 5.3: a) shown the original size of the AAF and b) is the increase in the area of the AAF from 132.6 mm^2 to 162.6 mm^2.

In the second iteration, a pocket to encapsulate and to better secure the ANP was introduced. The objective was to check if this was beneficial to the ANP and, consequently, if there was any improvement in the overall performance of the disc. The pocket had a depth of 0.5 mm (Figure 5.4). In this iteration, the model was designated as G_AEP_05.

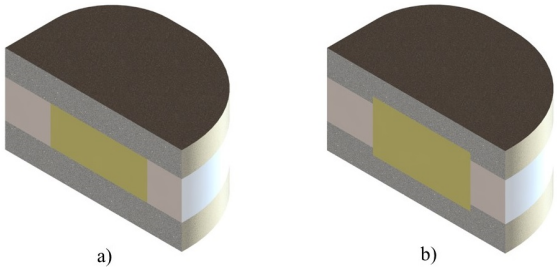

Figure 5.4: a) the original size of the endplate pocket. b) the increase in depth of the endplate pocket from 0mm to 0.5mm.

A table was created to provide a comprehensive description of all the models, their respective areas and the pocket depth (Table 5.1).

Table 5.1: Dimensional characteristics of the various geometric model iterations analysed.

Model description	Model Designation	Area of the AAF (mm^2)	Area of the ANP (mm^2)	Pocket depth in the endplate (mm)
Lower area in the annulus fibrosus	G_AAF_S	132.6	78.7	0
Higher area in the annulus fibrosus	G_AAF_B	162.6	48.8	0
With pocket in the endplates	G_AEP_05	132.6	78.7	0.5

All the CAD models were then imported to the *3DEXPERIENCE* (from Dassault Systemes) to be simulated. Inside the software, it was used *Mechanical Scenario Creation* (SIMULIA) to define all the necessary conditions and to run all the numerical simulations.

5.2.2.2 Material properties

The material properties for each component were established based on the bibliographic review. In these simulations, the end plates were defined as isotropic materials with linear elastic properties, ANPs were defined as incompressible isotropic materials, and AAFs were defined as transversely isotropic materials. The last component was defined differently to try to replicate the fibre material of the AAF.

AAF has a unique mechanical behaviour in tension and compression. When subjected to tension, the AAF demonstrates superior properties compared to compression, indicating a preference for being pulled rather than compressed. This transversely isotropic behaviour implies that the material possesses identical mechanical properties, such as stiffness or strength, along the longitudinal axis of the fibres. However, it exhibits different properties in the transverse directions. As a result, transversely isotropic materials are characterised by two Young's moduli: a transverse Young's modulus (E_p) [68, 69] and an axial Young's modulus [70], along with two Poisson's ratios: transverse (ν_p) and axial, and a transverse shear modulus (G_p). Calculation of the transverse shear modulus was determined using the formula provided in the reference [79].

$$G_p = \frac{E_p}{2(1+\nu_p)} \tag{5.1}$$

The material properties of the ANP were assumed to resemble those of an incompressible fluid, considering its gel-like liquid characteristics. As the specific hydrogel material for fabricating the ANP was yet to be determined, an experimental phase was planned to address this aspect. This phase was aimed at identifying the most suitable hydrogel formulation through experimental trials. Furthermore, selecting an appropriate material was crucial for studying the behaviour of the disc's geometry in the numerical simulations, so as previously said, it was chosen the material properties of the native NP, its Young modulus and Poisson's ratio defined in this study [62, 80].

The material properties for all components of the disc, and all iterations, are presented in Table 5.2.

Table 5.2: Material properties used for the artificial disc model.

Component	Iteration	Transverse Young modulus [MPa]	Transverse Poisson ratio	Axial Young modulus [MPa]	Axial Poisson ratio	Transverse Shear modulus [MPa]	Young modulus [MPa]	Poisson ratio
Annulus	AAF_L_YM	4	0.4	0.15	0.18	1.4	-	-
	AAF_H_YM	19	0.4	0.9	0.18	6.8	-	-
Nucleus	ANP_L_YM	-	-	-	-	-	1	0.49
	ANP_H_YM	-	-	-	-	-	4	0.49

5.2.2.3 Contact properties, boundary conditions and loading

Suitable boundary conditions were necessary to obtain an accurate simulation of the natural movement of the disc. In this case, the simulation was conducted differently from the studies mentioned in Chapter 3. The study was done using the disc itself and not a cervical spine segment. The main objective was not only to reduce computational efforts and simplify the model but also mechanical testing would be done only on the fabricated disc. This was necessary to be able to compare the computational simulations with the mechanical tests. Even with this simplification, it was taken into account in vitro studies and other computational studies to properly define the boundary and loading conditions and to be able to compare the results.

The numerical simulations were performed using explicit dynamic steps and in this case, two steps were performed in each model. Each of the steps has differences in terms of boundary conditions.

In Step 1, in the top endplate, a displacement of 0.6mm was applied in the superior/inferior direction to simulate 20% deformation. This is the average deformation of the native disc when compressed with a significant load [81]. The top endplate was also constrained in all degrees of freedom, except for superior-inferior translation. The bottom endplate was constrained in all degrees of freedom. This is shown in Figure 5.5 a).

In Step 2, in the top endplate the same displacement was applied as in Step 1, plus a rotation posterior/anterior (flexion) of 5.5° [24], simulating the full range of motion of

the cervical disc during flexion. It was allowed superior/inferior and anterior/posterior translation as well as rotation in the sagittal plane. The bottom endplate had the same boundary conditions as in Step 1. This is shown in Figure 5.5 b). All the boundary conditions are resumed in Table 5.3.

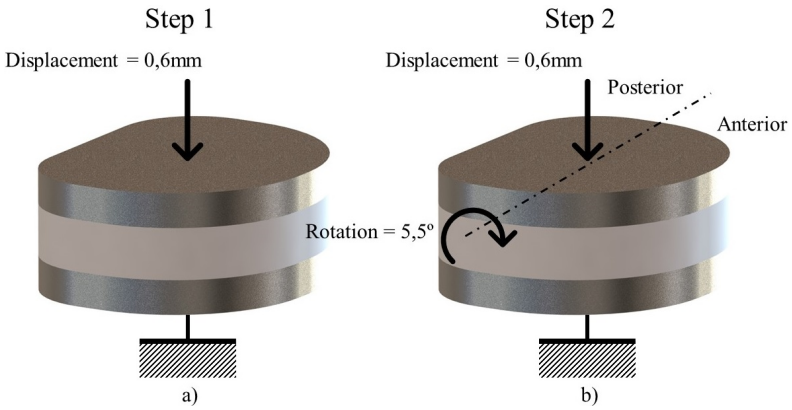

Figure 5.5: On the left side is Setp 1 with the displacement applied. On the right side is Step 2 with the displacement and applied 5.5°of flexion to the disc.

Table 5.3: Summary of all the applied boundary conditions to each step and component.

Disc feature	Boundary Condition	Physical Meaning
Bottom enplate	Restricted in all degrees of freedom	In both steps the bottom endplate was fixed to be able to simulate the disc as equal as possible to the mechanical testing.
Top endplate	Step 1: displacement of 0.6 mm applied and superior/inferior translation was allowed	The displacement applied to the top endplate corresponds to a 20% deformation, wich is the deformation value of the native IVD.
	Step 2: displacement of 0.6 mm; posterior/anterior rotation (flexion) of 5.5 ; superior/inferior and anterior/posterior translation was allowed, as well as rotation in the sagital plane	Besides the displacement, the applied rotation of 5.5 corresponds to the range of motion of the native disc during flexion

In order to properly simulate the models, it was also necessary to define the contact properties. In each model, all the components were rigidly connected, since, in reality, the components of the fabricated disc are connected in the same way. Additionally, both endplates were defined as rigid bodies to prevent distortions and uneven force distribution in the models. Creating the numerical model with these conditions allows for a more accurate representation. These conditions were applied to the models using the *3DEXPERIENCE, (SIMULIA)* to create the numerical models.

Finally, a thorough analysis of the von Mises stresses in the AAF and ANP for all models was performed. Additionally, the analysis of the reaction forces, and resistive moment on the bottom endplate: in one instance to understand what load was needed to deform the artificial disc by 20%; In another instance, to understand the moment that is needed to rotate the disc 5.5°. The results were then compared with the native

IVD. The following Table 5.4 presents a summary of all the examined cases along with their corresponding designations.

Table 5.4: Summary of analyzed cases, combined with geometry and material properties

Analyzed effects	Model description	Model iteration	Geometry		Material Properties	
			Annulus fibrosus	Endplate pocket	Artificial annulus fibrosus	Artificial nucleus pulposus
The effect of the area on the AAF and ANP	Smaller area in the AAF	AnF_L_A	G_AAF_S	G_AEP_0	AAF_L_YM	ANP_L_YM
	Bigger area in the AAF	AnF_H_A	G_AAF_B			
The effect of the endplate pocket	Endplate with 0.5mm pocket	EndPla_05	G_AAF_S	G_AEP_05	AAF_L_YM	ANP_L_YM
The effect of the material properties	AAF with higher mechanical properties	AnF_H_YM	G_AAF_S	G_AEP_0	AAF_H_YM	ANP_L_YM
	ANP with higher mechanicals properties	NuP_H_YM			AAF_L_YM	ANP_H_YM

5.2.2.4 Finite element mesh

In order to simulate the models, it was necessary to create meshes. The creation of meshes took into consideration different types of elements available for mesh generation. According to Silva et al. [62], two preferred elements, tetrahedral and hexahedral, were identified for the cervical spine. While tetrahedral elements facilitate meshing on curved surfaces, they can be computationally expensive and unnecessarily stiff. Based on the findings from the literature review, hexahedral elements were utilized.

For the ANP and AAF, an element size of 0.8mm was employed to ensure a more precise analysis without excessive computational efforts. In contrast, 1mm elements were used for the two endplates. All components were modelled using eight-node brick elements with reduced integration (C3D8R). The mesh size and element type were consistent across all models shown in Figure 5.6. The number of nodes and elements for each model can be found in Table 5.5.

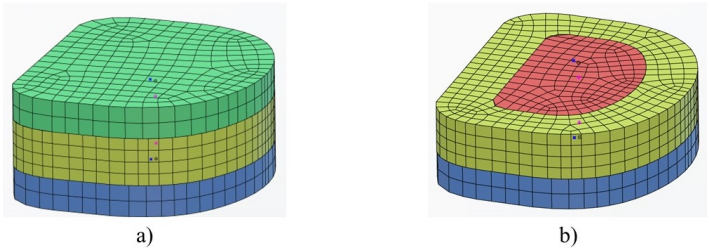

Figure 5.6: Example of the artificial disc with the mesh. On the left side a) both endplates and the AAF with the mesh. On the right side b), a cut view with the transverse plane, to show the ANP with the mesh.

Table 5.5: Number of elements and nodes for each model

Model designation	Number of elements	Number of nodes
AnF_L_A	2514	3935
AnF_H_A	2738	4175
EndPla_05	7683	13521
AnF_H_YM	2514	3935
NuP_H_YM	2514	3935

5.2.3 Results

5.2.3.1 AAF area iteration

The results of the models where the area was the variable are represented below. First, the AAF with the smaller area (AnF_L_A) and second the model where the area was increased (AnF_H_A). The von Mises stress is represented for each model. Also the plots for the evolution of the reaction force and reaction moment in the bottom endplate, for Step 1 and Step 2. The stiffness for each of the numerical simulations was calculated.

Figure 5.7 represents the von Mises stress for the AAF of the models AnF_L_A and AnF_H_A for Step 1. The maximum von Mises stress for the AnF_L_A was 0.848 MPa and for the AnF_H_A was 0.711 MPa. During the compressive displacement of 0.6 mm, the stress in the AAF for the model with the bigger area was lower.

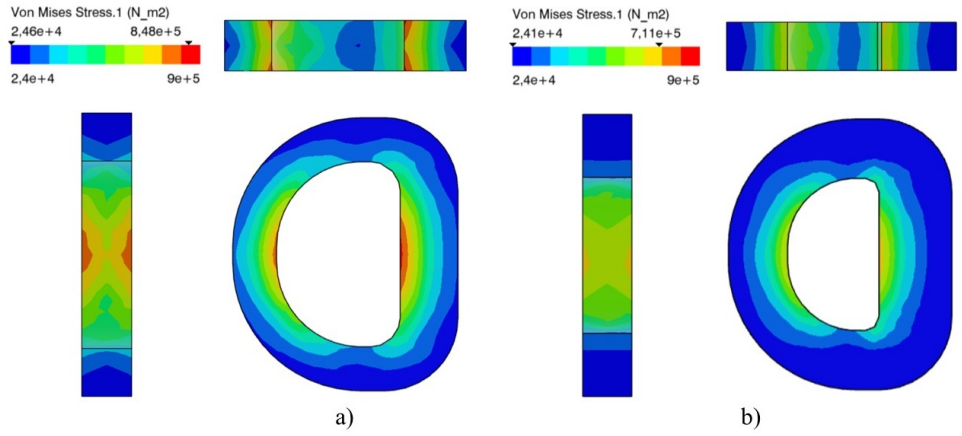

Figure 5.7: von Mises stress for the AAF of the models a) AnF_L_A and b) AnF_H_A for step 1.

Figure 5.8 represents the von Mises stress for the ANP of the models AnF_L_A and AnF_H_A for Step 1. The maximum von Mises stress for the AnF_L_A was 0.557 MPa and for the AnF_H_A was 0.487 MPa.

Figure 5.9 represents the von Mises stress distribution for the AAF in the AnF_L_A and AnF_H_A models during Step 2. The maximum von Mises stress recorded for the AnF_L_A model was 1.08 MPa, while for the AnF_H_A model, it was 0.884 MPa. Notably, the application of rotation resulted in a stress concentration zone within the AnF_L_A model. This zone exhibited a higher level of deformation compared to the AnF_H_A model.

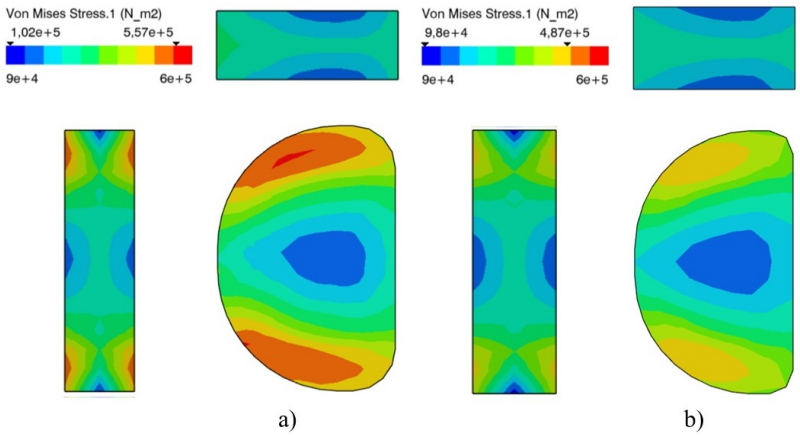

Figure 5.8: von Mises stress for the ANP of the models a) AnF_L_A and b) AnF_H_A for step 1.

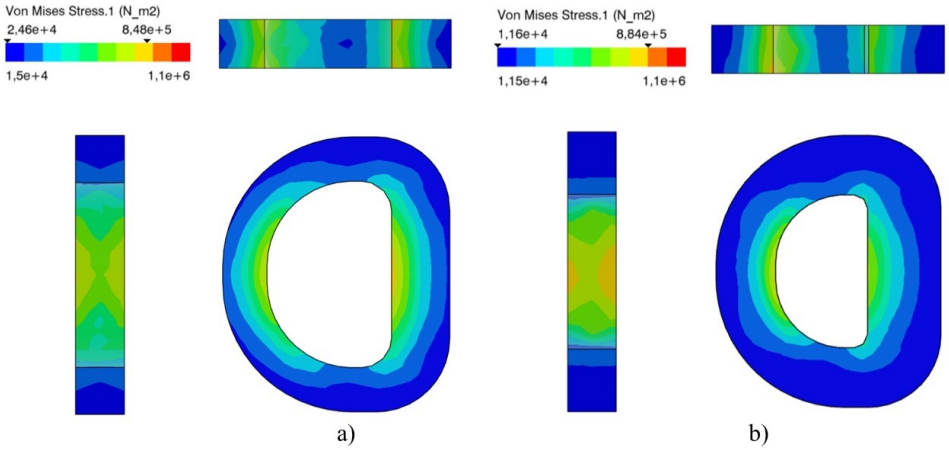

Figure 5.9: von Mises stress for the AAF of the models a) AnF_L_A and b) AnF_H_A for step 2.

Figure 5.10 represents the von Mises stress distribution for the ANP in the AnF_L_A and AnF_H_A models during Step 2. The maximum von Mises stress recorded for the AnF_L_A model was 0.812 MPa, while for the AnF_H_A model, was 0.599 MPa. The same result observed in the AAF of AnF_L_A happens for the ANP. The application of flexion resulted in a stress concentration zone within the AnF_L_A model.

Figure 5.11, two plots are represented. Plot a) represents the evolution of the reaction force during Step 1 of the numerical simulations for the AnF_L_A model (AAF with a smaller area). The maximum recorded reaction force, in this case, was 95.3N. On the other hand, plot b) shows the evolution of the reaction force during Step 1 of the AnF_H_A model (bigger area), with a maximum reaction force of 55.3 N.

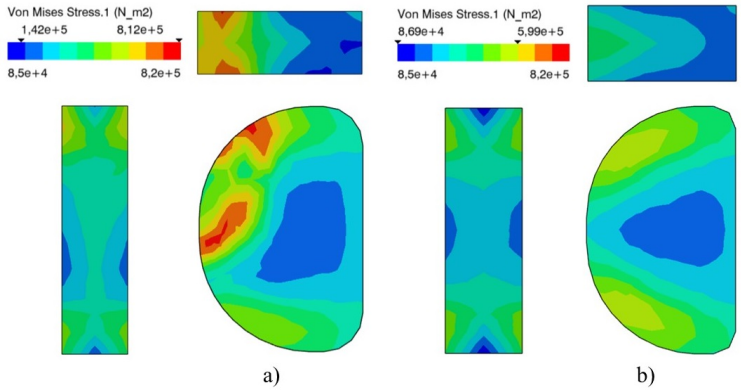

Figure 5.10: von Mises stress for the ANP of the models a) AnF_L_A and b) AnF_H_A for step 2.

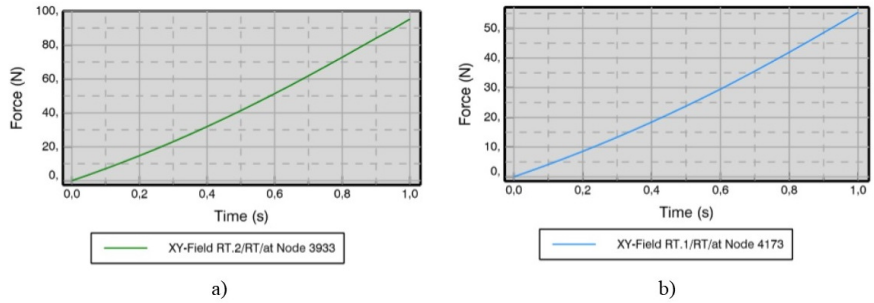

Figure 5.11: Reaction forces in the bottom endplate for the models a) AnF_L_A and b) AnF_H_A.

Figure 5.12, two plots are presented. Plot a) represents the evolution of the reaction moment during Step 2 for the AnF_L_A model. The maximum recorded reaction moment before reaching 5.5°of flexion was 0.11 Nm. It is worth noting a slight decrease in the reaction moment, which coincides with the onset of deformation observed in both Figure 5.9 and Figure 5.10. On the other hand, plot b) illustrates the reaction moment at Step 2 for the AnF_H_A model, with a maximum moment of 0.07 Nm occurring at 5.5°of flexion.

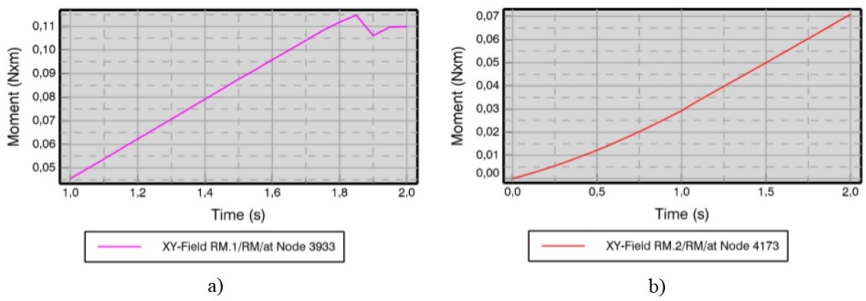

Figure 5.12: Reaction moments in the bottom endplate for the models a) AnF_L_A and b) AnF_H_A.

With the resulting force is possible to calculate the stiffness of the models. Model AnF_L_A had a maximum stiffness of 158.8 N/mm. Model AnF_H_A had a maximum stiffness of 92.2 N/mm.

5.2.3.2 Endplate pocket iteration

Figure 5.13 are represented the von Mises stress for the AAF of the models AnF_L_A and EndPla_05 (model with a 0.5 mm pocket in the endplate) for Step 1. The maximum von Mises stress for the AnF_L_A was 0.848 MPa and for the EndPla_05 was 1.12 MPa.

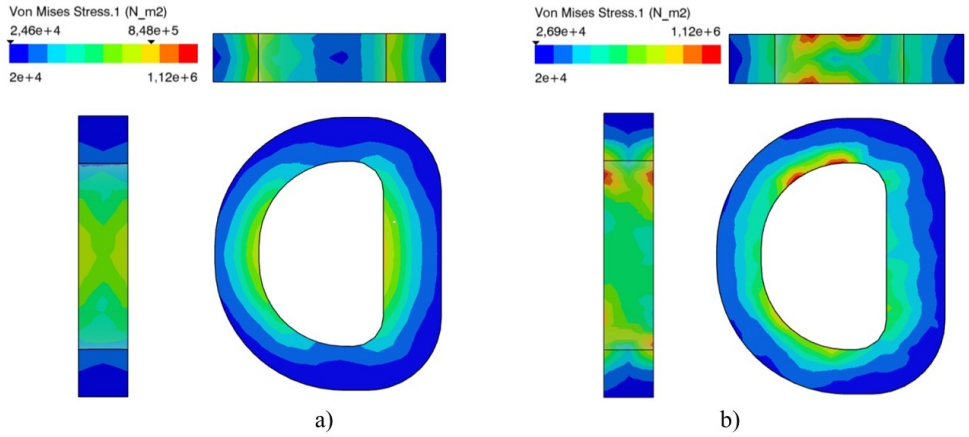

Figure 5.13: von Mises stress for the AAF of the models a) AnF_L_A and b) EndPla_05 for step 1.

Figure 5.14 represents the von Mises stress for the ANP of the models AnF_L_A and EndPla_05 for Step 1. The maximum von Mises stress for the AnF_L_A was 0.557 MPa and for the EndPla_05 was 1 MPa.

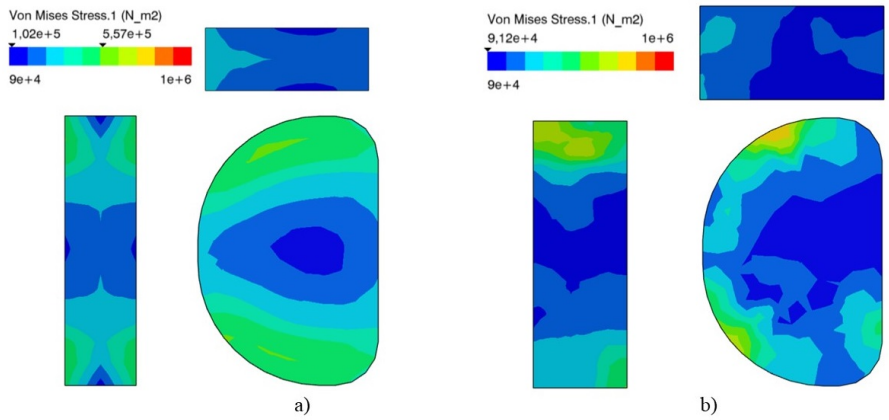

Figure 5.14: von Mises stress for the ANP of the models a) AnF_L_A and b) EndPla_05 for step 1.

Figure 5.15 represents the von Mises stress distribution for the AAF in the AnF_L_A and EndPla_05 models during Step 2. The maximum von Mises stress recorded for the AnF_L_A model was 1.08 MPa, while for the EndPla_05 model, it was 1.45 MPa.

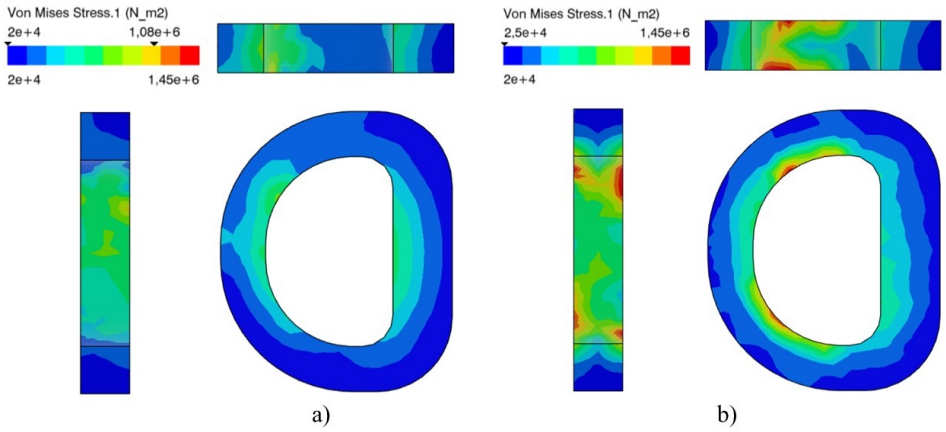

Figure 5.15: von Mises stress for the AAF of the models a) AnF_L_A and b) EndPla_05 for step 2.

Figure 5.16 represents the von Mises stress distribution for the ANP in the AnF_L_A and EndPla_05 models during Step 2. The maximum von Mises stress recorded for the AnF_L_A model was 0.812 MPa, while for the EndPla_05 model, it was 1.02 MPa.

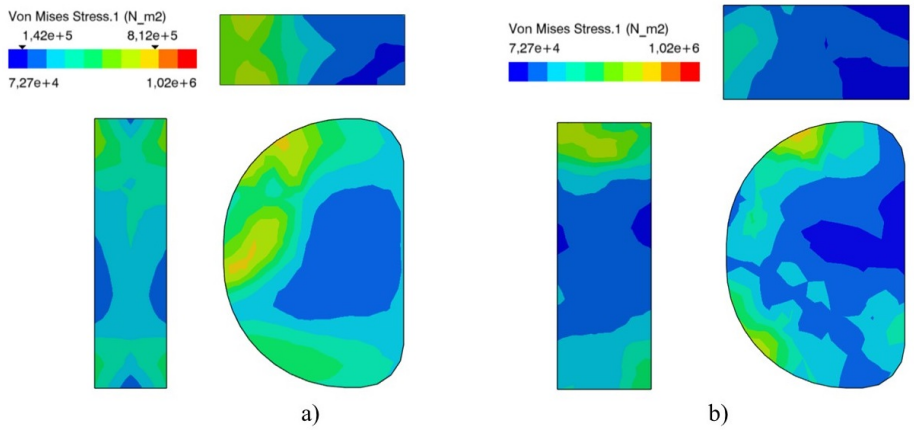

Figure 5.16: von Mises stress for the ANP of the models a) AnF_L_A and b) EndPla_05 for step 2.

Figure 5.17, two plots are exhibited. Plot a) represents the evolution of the reaction force during Step 1 of the numerical simulations for the AnF_L_A model. The maximum recorded reaction force, in this case, was 95.3 N. On the other hand, plot b) shows the evolution of the reaction force during Step 1 of the EndPla_05 model, with a maximum reaction force of 75.8 N.

Figure 5.18, two plots are displayed. Plot a) represents the evolution of the reaction moment during Step 2 for the AnF_L_A model. The maximum recorded reaction moment before reaching 5.5°of flexion was 0.115 Nm. On the other hand, plot b) illustrates the reaction moment at Step 2 for the EndPla_05 model, with a maximum moment of 0.105 Nm occurring at 5.5° of flexion.

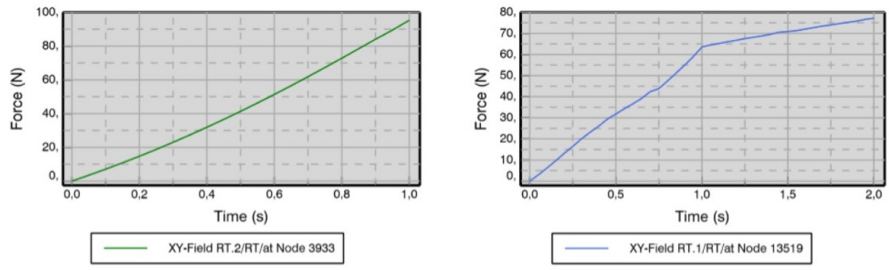

a) b)

Figure 5.17: Reaction forces in the bottom endplate for the models a) AnF_L_A and b) EndPla_05.

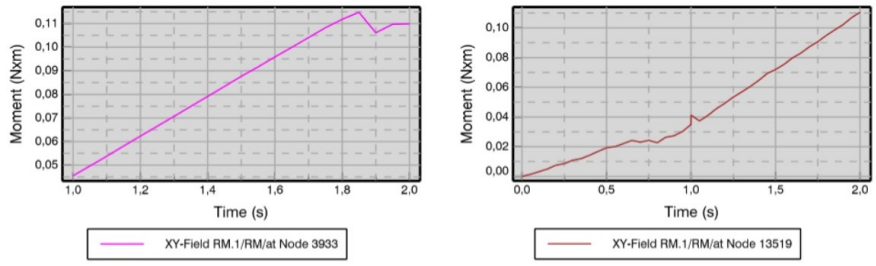

a) b)

Figure 5.18: Reaction moments in the bottom endplate for the models a) AnF_L_A and b) EndPla_05.

With the resulting force is possible to calculate the stiffness of the models. Model AnF_L_A had a maximum stiffness of 158.8 N/mm. Model AnF_H_A had a maximum stiffness of 126.3 N/mm.

5.2.3.3 Material properties variations

Lastly, the results of the numerical simulations is presented with different material properties for the AAF and ANP. AnF_H_YM is the model where the values of the Young modulus of AAF are higher. NuP_H_YM is the model where the Young modulus of the NP is higher.

Figure 5.19 the von Mises stress for the AAF of the models AnF_L_A and AnF_H_YM for Step 1 are exhibited. The maximum von Mises stress for the AnF_L_A was 0.848 MPa and for the AnF_H_YM was 2.33 MPa.

In Figure 5.20 the von Mises stress for the ANP of the models AnF_L_A and AnF_H_YM for Step 1 are exhibited. The maximum von Mises stress for the AnF_L_A was 0.557 MPa and for the AnF_H_YM was 0.536 MPa.

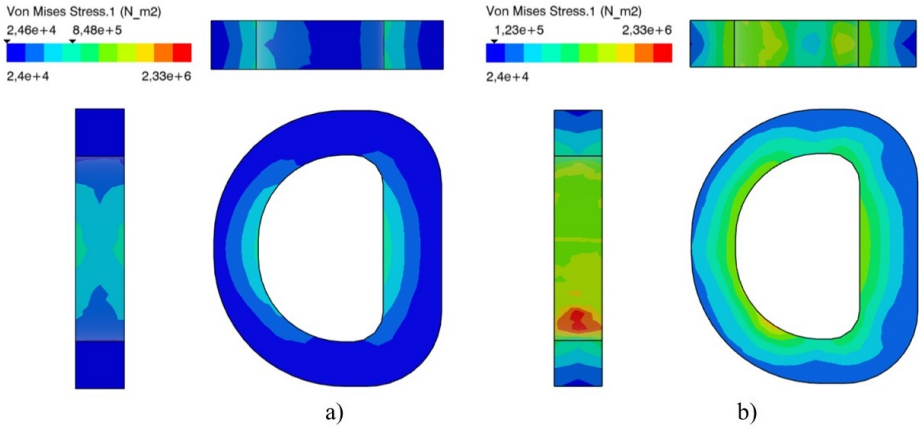

Figure 5.19: von Mises stress for the AAF of the models a) AnF_L_A and b) AnF_H_YM for step 1.

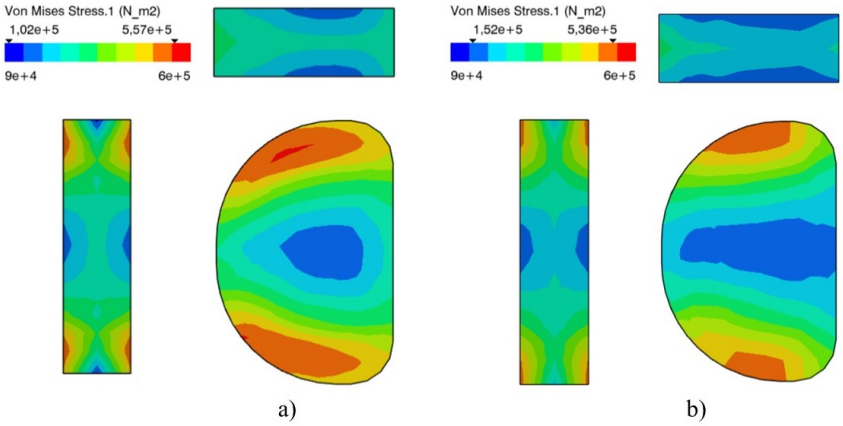

Figure 5.20: von Mises stress for the ANP of the models a) AnF_L_A and b) AnF_H_YM for step 1.

In Figure 5.21 the von Mises stress distribution for the AAF in the AnF_L_A and AnF_H_YM models during Step 2 are presented. The maximum von Mises stress recorded for the AnF_L_A model was 1.08 MPa, while for the AnF_H_YM model, it was 3.33 MPa.

Figure 5.22 the von Mises stress distribution for the ANP in the AnF_L_A and AnF_H_A models during Step 2 are presented. The maximum von Mises stress recorded for the AnF_L_A model was 0.812 MPa, while for the AnF_H_A model, it was 0.622 MPa.

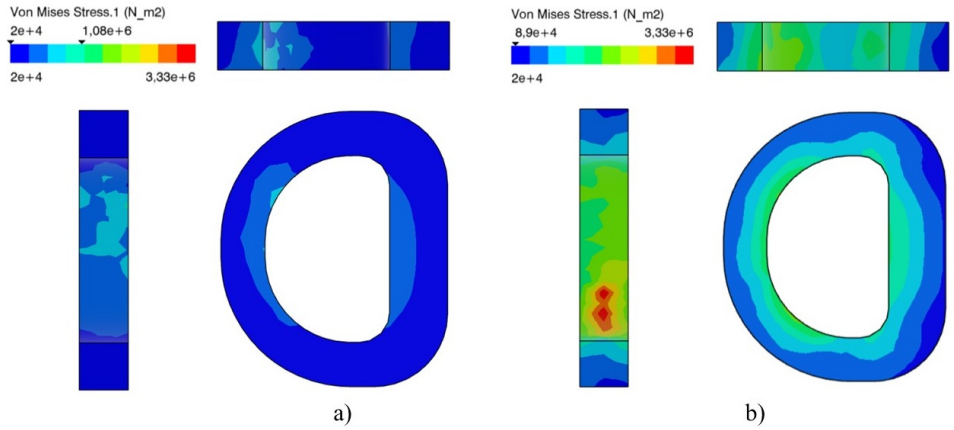

Figure 5.21: von Mises stress for the AAF of the models a) AnF_L_A and b) AnF_H_YM for step 2.

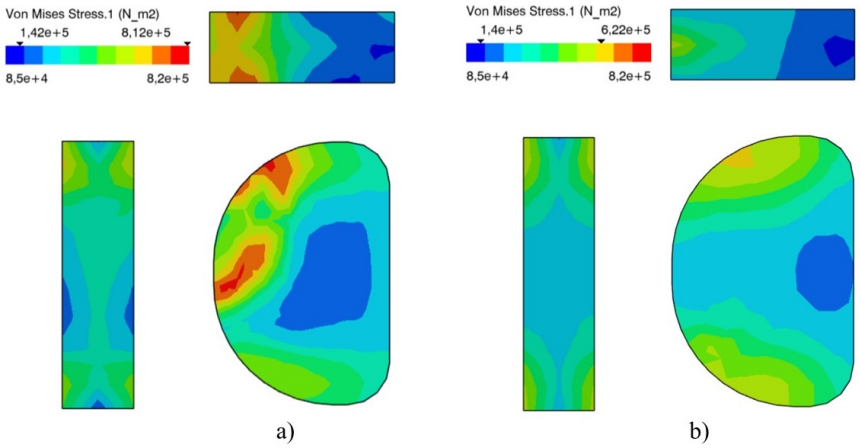

Figure 5.22: von Mises stress for the ANP of the models a) AnF_L_A and b) AnF_H_YM for step 2.

In Figure 5.23, two plots are displayed. Plot a) represents the evolution of the reaction force during Step 1 of the numerical simulations for the AnF_L_A model. The maximum recorded reaction force, in this case, was 95.3 N. On the other hand, plot b) shows the evolution of the reaction force during Step 1 of the AnF_H_YM model, with a maximum reaction force of 181.6 N.

In Figure 5.24, two plots are displayed. Plot a) represents the evolution of the reaction moment during Step 2 for the AnF_L_A model. The maximum recorded reaction moment before reaching 5.5°of flexion was 0.11 Nm. On the other hand, plot b) illustrates the reaction moment at Step 2 for the AnF_H_YM model, with a maximum moment of 0.26 Nm occurring at 5.5° of flexion. With the resulting force is possible to calculate the stiffness of the models. Model AnF_L_A had a maximum stiffness of 158.8N/mm. Model AnF_H_YM had a maximum stiffness of 302.6 N/mm.

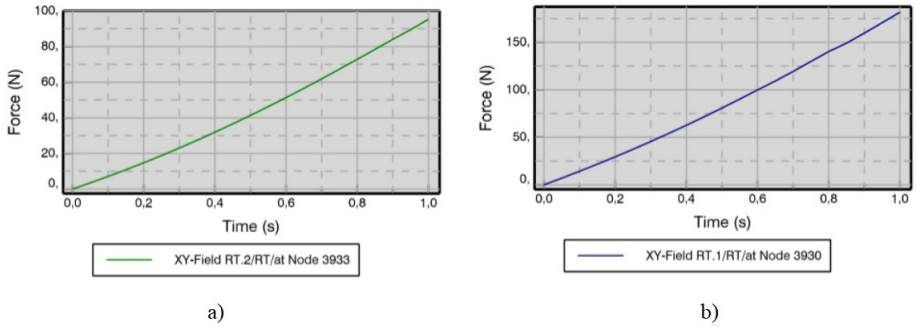

a) b)

Figure 5.23: Reaction forces in the bottom endplate for the models a) AnF_L_A and b) AnF_H_YM.

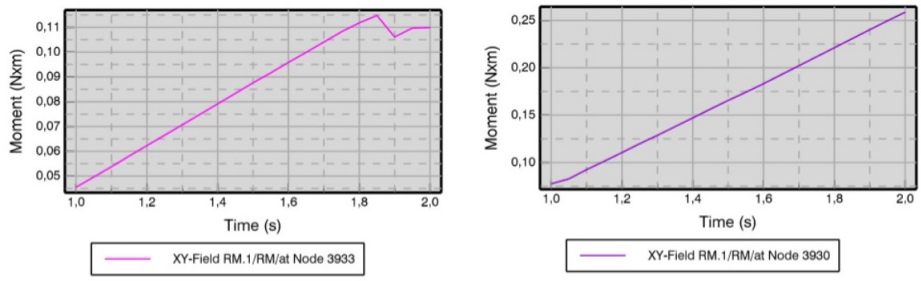

a) b)

Figure 5.24: Reaction moments in the bottom endplate for the models a) AnF_L_A and b) AnF_H_YM.

The second variation in the material properties was in the ANP. Figure 5.25 presentes the von Mises stress for the AAF of the models AnF_L_A and NuP_H_YM for Step 1. The maximum von Mises stress for the AnF_L_A was 0.848 MPa and for the NuP_H_YM was 1.91 MPa.

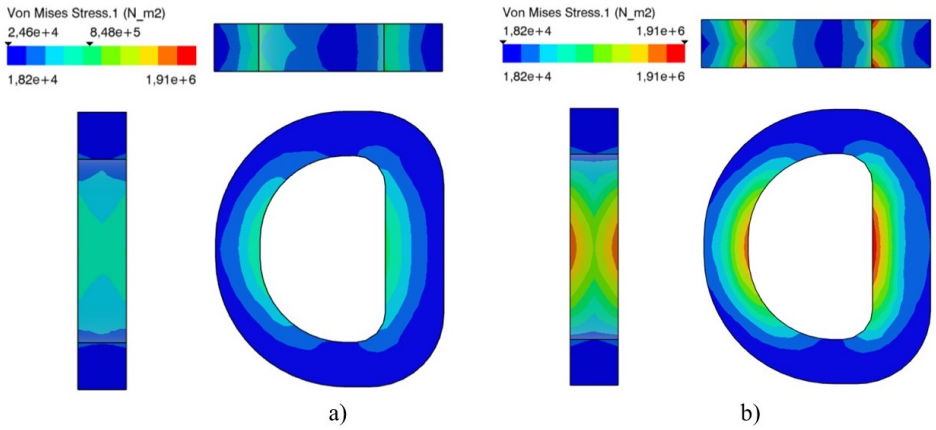

a) b)

Figure 5.25: von Mises stress for the AAF of the models a) AnF_L_A and b) NuP_H_YM for step 1.

Figure 5.26 presents the von Mises stress for the ANP of the models AnF_L_A and NuP_H_YM for Step 1. The maximum von Mises stress for the AnF_L_A was 0.557 MPa and for the NuP_H_YM was 1.95 MPa.

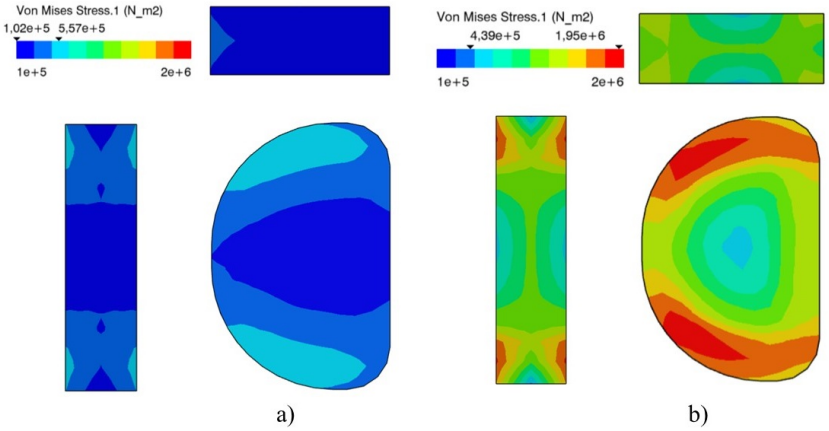

Figure 5.26: von Mises stress for the ANP of the models a) AnF_L_A and b) NuP_H_YM for step 1.

Figure 5.27 presents the von Mises stress distribution for the AAF in the AnF_L_A and NuP_H_YM models during Step 2. The maximum von Mises stress recorded for the AnF_L_A model was 1.08 MPa, while for the NuP_H_YM model, it was 2.63 MPa.

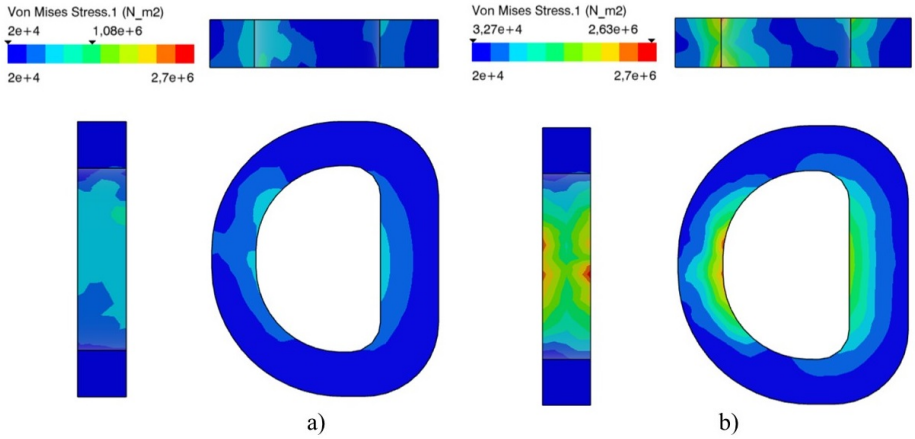

Figure 5.27: von Mises stress for the AAF of the models a) AnF_L_A and b) NuP_H_YM for step 2.

Figure 5.28 presents the von Mises stress distribution for the ANP in the AnF_L_A and NuP_H_YM models during Step 2. The maximum von Mises stress recorded for the AnF_L_A model was 0.812 MPa, while for the NuP_H_YM model, it was 2.81 MPa.

In Figure 5.29, two plots are presented. Plot a) represents the evolution of the reaction force during Step 1 of the numerical simulations for the AnF_L_A model. The maximum recorded reaction force, in this case, was 95.3 N. On the other hand, plot b) shows the evolution of the reaction force during Step 1 of the NuP_H_YM model, with a maximum reaction force of 266.8 N.

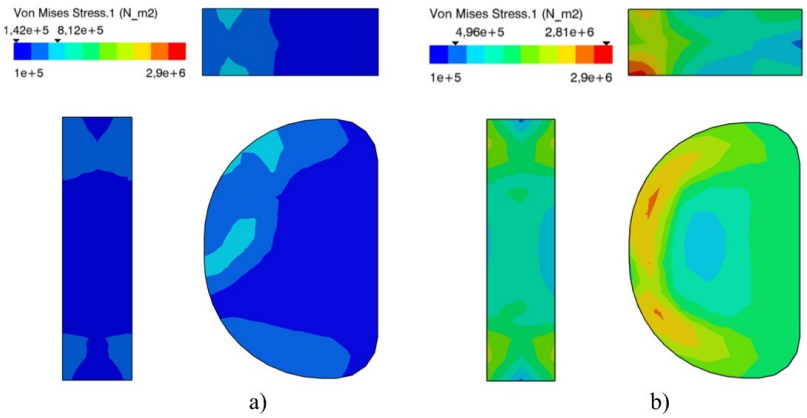

Figure 5.28: von Mises stress for the ANP of the models a) AnF_L_A and b) NuP_H_YM for step 2.

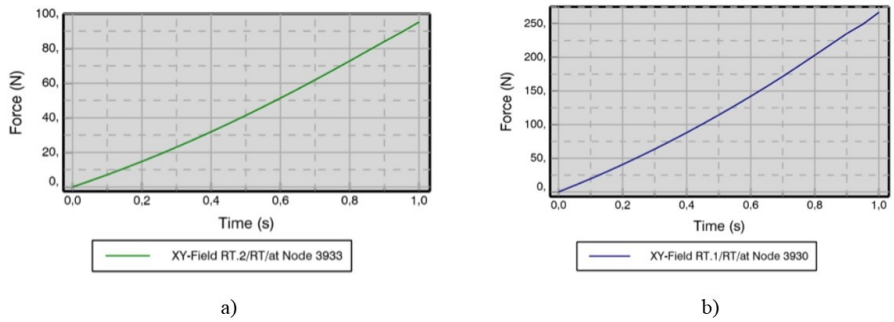

Figure 5.29: Reaction forces in the bottom endplate for the models a) AnF_L_A and b) NuP_H_YM.

In Figure 5.30, two plots are presented. Plot a) represents the evolution of the reaction moment during Step 2 for the AnF_L_A model. The maximum recorded reaction moment before reaching 5.5°of flexion was 0.11 Nm. On the other hand, plot b) illustrates the reaction moment at Step 2 for the NuP_H_YM model, with a maximum moment of 0.32 Nm occurring at 5.5° of flexion.

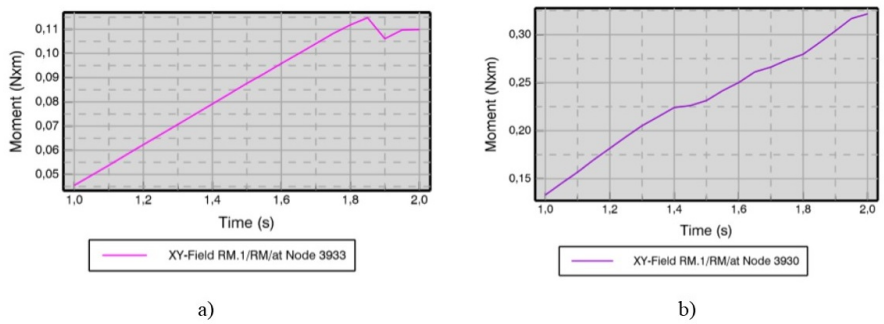

Figure 5.30: Reaction moment in the bottom endplate for the models a) AnF_L_A and b) NuP_H_YM.

With the resulting force is possible to calculate the stiffness of the models. Model AnF_L_A had a maximum stiffness of 158.8 N/mm. Model NuP_H_YM had a maximum stiffness of 444.7 N/mm.

5.2.4 Discussion

These numerical simulations were used to optimize the final model to be fabricated, as well as, to understand what happens when the mechanical properties of the AAF and ANP change.

The AnF_L_A can hold almost double the load for the same displacement (95.3 N compare to 55.3 N), which in this case was necessary because it means that the stiffness is higher (158.8 N/mm compared to 92.2 N/mm). This load difference was also shown in the von Mises stress that was higher for the AnF_L_A in all the cases. With the only difference being the area of the AAF, the increase in the area didn't help the overall performance of the disc.

The same happens when the comparison turns to the EndPla_05. The stiffness in this model is lower than in the AnF_L_A (158.8 N/mm compared to 126.3 N/mm). This time the von Mises stress was higher in the EndPla_05. The analysis of the result shows the stress concentration in the area where the ANP is encapsulated in the endplates. The ANP cannot deform in a homogeneous way due to this contact with the lateral walls of the endplate pocket increasing the stress. Due to this, the disc cannot perform as well as the AnF_L_A. In conclusion, it is proven that the use of the pockets in the endplates, is not beneficial.

When the changes were applied in the material properties, the model performed better, as expected. The stiffness in both cases increased, compared to the AnF_L_A. It was 302.6 N/mm for the AnF_H_YM and 444.7N/mm for the NuP_H_YM. The increase in the mechanical properties of the ANP increases the performance of the disc more drastically than the increase in the mechanical properties of the AAF. This means that to achieve a better performance disc, according to this result, the choice of hydrogel to mimic the native NP can have a greater impact on the disc.

The native IVD has a compressive stiffness of around 600 N/mm [20]. The AnF_L_A was a model with mechanical properties close to the ones that reassemble the construction of the AAF and ANP in the experimental phase, which is far off the goal stiffness of the native IVD. It would be necessary to increase this stiffness in order to achieve this. Even with the increase in material properties values, the stiffness was still lower than in the native IVD.

Comparing this result with [62], which is a computational study of the cervical spine, it can be seen that applying a load of 1Nm to promote flexion in the segment, resulted in a range of motion of 2.03°. Also, an in vitro study made by [24] reported a rotation of around 3.2°for the same moment of 1 Nm. In this project, in none of the models, the reaction moment was close to 1 Nm for the 5.5°of flexion, meaning that the models underperformed in comparison with these studies.

Cervical implants already in the market [48–50, 61], have better properties to the compressive load. For example, the M6-C has a failure load of 6714 N. Comparing the AnF_L_A model to the M6-C, it can be concluded that AnF_L_A is not near in terms of mechanical properties.

Overall, this study, as expected, was decisive to put to test the different ideas for

the model, as well as to help understand the different effects of the model, when using different materials, with different mechanical properties. It is possible to conclude that, is necessary to find materials with better mechanical properties than the ones used, in order to replicate the native IVD.

5.3 Automatic manufacture and experimental characterisation of the cervical disc

5.3.1 Introduction

As stated in the bibliographic review, the AF is composed of 15-25 concentric lamellae which surround the NP and confines its pressure. Each lamella is composed of organized collagen fibres. In order to mimic the native IVD, it was proposed to construct an artificial disc comprising an AAF composed of electrospun polycaprolactone (PCL) fibres, using the 3D electrospinning system [82], surrounding a hydrogel ANP. This system allows the construction of the disc geometry with fibre orientation automatically, as proposed.

Several steps were undertaken to realize this proposed concept. Firstly, the preparation of the endplates and PCL solution, and the selection of the appropriate hydrogel needed to be determined. Next, the fabrication parameters of the 3D electrospinning system were defined, and the system's trajectories were set to automate the disc fabrication process. After the AAF was fabricated, the hydrogel deposition was performed. Subsequently, mechanical testing was conducted to characterize the properties of the disc and evaluate its performance.

5.3.2 Materials and methods

5.3.2.1 Materials preparation

The numerical simulations guided the selection of a specific model for fabrication in this project, which featured a smaller area in the AAF and did not include a pocket on the endplates. This chosen model had precise geometric specifications, with an AAF area measuring 132.6 mm^2 and an ANP area measuring 78.7 mm^2.

Endplate preparation

Initially, two options were considered for the endplates: titanium and hydroxyapatite. However, after conducting a thorough literature review and analyzing the results of numerical simulations, the focus shifted to the AAF and ANP, as their material properties were found to be weaker than expected. Consequently, the decision was made to utilize metal endplates due to their ease of fabrication.

Since the material used for the endplates was not a major concern, aluminium was chosen for its advantages in machining, accessibility, and cost-effectiveness. The endplates were manufactured by a collaborator from the university's machining laboratory. To accommodate their small size and facilitate the holding in the CNC machine, the machined endplates featured a small hole. Besides that, they are the same as in the

concept (Figure 5.31). The hole was patched so the endplate could contain the hydrogel ANP.

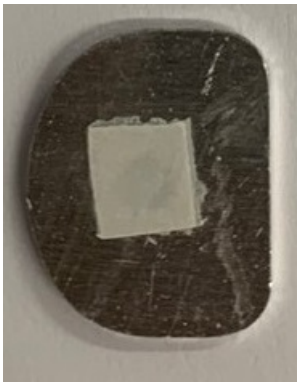

Figure 5.31: The aluminium endplates after machining and the centre hole patched.

Preparation of the PCL solution

Polymeric solutions of polycaprolactone (PCL; Sigma-Aldrich) and porcine skin gelatin (GEL; Sigma-Aldrich) were separately dissolved in 2,2,2-trifluoroethanol (TFE) 99+% at a concentration of 12% (w/v), agitated with a magnetic stirrer at room temperature overnight and mixed in a volume ratio of 80:20 with 0.2% (v/v) of acetic acid. The resulting solution was poured into a 5 mL plastic syringe with a diameter of 12mm.

Hydrogel preparation

A hydrogel was the material that makes up the ANP of the disc and its main function was to resist compressive loads; however, from the bibliographic review, the mechanical properties of the hydrogels were far from the needs of an artificial NP. With this in mind, and since the hydrogel choice was a variable in this project, an exploratory phase was initiated to replicate some hydrogels found in the review or to try to develop a new one. Afterwards, the fabricated hydrogels underwent mechanical characterization to assess their performance and properties.

It began by making agarose-based hydrogels, as this is the most commonly used hydrogel in the application of scaffolds for the intervertebral disc. Agarose (AG) (GRS agarose LMT) was dissolved in phosphate-buffered saline (PBS) at two different concentrations, 5% and 7% (w/v), by agitation with a magnetic stirrer at 80°C. In order to test if the mechanical properties of the hydrogel could be improved, a solution of graphene oxide (GO) was added, since this nanomaterial is frequently used as a mechanical reinforcing agent. The selected concentrations were at concentrations of 0.05% and 0.1% (v/v), by adding GO to PBS before adding AG. The solutions were poured into moulds while they were hot and allowed to gel there, to make samples for mechanical characterisation (Figure 5.32). After being extracted from the mould the samples were left in a PBS bath for a day. Four samples of each type of hydrogel solution were tested.

Following the mechanical characterization and analysis of the results (Table 5.6) obtained from previous hydrogel solutions, additional attempts were made to improve the

a) b)

Figure 5.32: Hydrogel samples preparation. On the left side a), the hydrogel was poured into the moulds. On the right side b), the hydrogel samples after extraction from the moulds.

outcomes. Agarose served as the base material, and blending it with different hydrogels was explored as a potential solution to achieve the desired properties. Among the hydrogels considered for blending, alginate (Alg) and collagen hydrogels were selected. The total polymer concentration was consistently maintained at 7% (w/v) as it yielded superior results in terms of Young's modulus within the range of 10-20% deformation in the previous mechanical tests.

Table 5.6: Results of the first experimental testing performed on the agarose hydrogels.

Agarose (%)	Graphene oxide (%)	Young's Modulus [Pa]	
		Mean	Standard deviation
5	0	107050	36728
5	0.1	38230	20180
7	0	96606	60253
7	0.05	125150	97085
7	0.1	208890	20234

To ensure comparability and address certain issues such as air bubbles in the hydrogel samples, the 7% AG hydrogel formulation was repeated both with and without the reinforcement of GO. This approach aimed to rectify previous errors and enable a more comprehensive evaluation of the hydrogel properties.

The same as before, AG (GRS agarose LMT) and alginic acid sodium salt (Sigma-Aldrich) was dissolved in PBS at a total concentration of 7% (w/v) (75% AG, 25% Alg), by agitation with a magnetic stirrer at 80°C. The solution was poured into moulds while hot and allowed to gel. For the other case, collagen from bovine Achilles tendon (Sigma-Aldrich), previously methacrylated (Col-MA) for UV-crosslinkable hydrogel, and a photoinitiator, Lithium phenyl-2,4,6-trimethylbenzoylphosphinate (Sigma-Aldrich) were dissolved in PBS for 24h by agitation with a magnetic stirrer. After this time, AG (GRS agarose LMT) was added and dissolved in the PBS with Col-MA, by agitation with a magnetic stirrer at 80°C. The solution was poured into moulds while hot, and a UV light was used to gel the Col-MA in the solution, while the agarose was gelled by cooling. Some samples were reinforced with 0.1% (v/v) GO with the same method as before, making AG+Alg+GO and AG+Col-MA+GO hydrogels.

Prior to conducting mechanical testing, the hydrogel samples were immersed in a PBS solution for a day. However, certain samples of AG+Alg and AG+Alg+GO were treated

differently. These particular samples were submerged in a calcium chloride (CaCl2) solution to facilitate alginate gelation and enable a comparison with the samples immersed in the PBS solution. This variation in treatment aimed to investigate and evaluate any differences in gelation behaviour between the two solutions. Four samples of each type of hydrogel solution were tested.

Results of the mechanical testing of the hydrogels are presented in Table 5.7. Three parameters were evaluated: Young´s modulus [Pa], Yield strength [Pa] and strain at yield [%].

Table 5.7: Results of the mechanical tests performed on the hydrogels.

Sample	Young's Modulus [Pa]		Yield strength [Pa]		Strain at yield [%]	
	Mean	Standard deviation	Mean	Standard deviation	Mean	Standard deviation
7% AG	470905	80536	103373	14909	26.08	2.49
7% AG+0,05%GO	446000	149916	87216	37308	23.68	5.59
7% AG+0,1%GO	294693	187892	82206	38000	32.83	5.60
AG+Alg-PBS	170155	144483	55800	42665	33.2	17.52
AG+Alg-CaCl2	162324	54744	63835	28793	51.53	3.56
AG+Alg+0.1%GO-PBS	266763	104547	43806	7502	18.34	3.21
AG+Alg+0.1%GO-CaCl2	283410	75006	53600	10573	22.63	4.94
AG+Col-MA	411821	121954	78742	26066	24.03	4.44
AG+Col-MA+0.1%GO	190850	55278	37114	6940	22.43	6.25

Among the tested hydrogel solutions, the 7% AG hydrogel exhibited the highest mean Young's modulus (470905 Pa) and mean yield strength (103373 Pa). However, the AG+Alg-CaCl2 hydrogel, while displaying a lower Young's modulus and yield strength compared to the 7% AG hydrogel, demonstrated the highest strain at yield. This characteristic could potentially be advantageous when working with the AAF. However, due to concerns regarding the behaviour of PCL in a CaCl2 bath, and this would add an uncontrollable variable, the decision was to abandon the idea of using the AG+Alg-CaCl2 hydrogel.

Following the test phase and analysis of the mechanical results, three hydrogel formulations were selected for incorporation into the disc: (1) 7% agarose, chosen for its higher Young's modulus; (2) AG+Alg, selected for its greater deformation at yield; and (3) AG+Col-MA, which had Young's modulus not far from the best-performing hydrogel. Additionally, the inclusion of collagen in AG+Col-MA aimed to enhance biocompatibility, considering the presence of collagen in the native NP composition. Table 5.8 provides a summary of the hydrogels and their compositions.

Table 5.8: Hydrogel composition used in the fabricated discs. All the hydrogels were made to 7% (w/v).

Hydrogel	Composition (%)		
	Agarose	Alginate	Collagen
AG	100	-	-
AG+Alg	75	25	-
AG+Col-MA	75	-	25

5.3.2.2 Fabrication parameters

Figure 5.33 illustrates the electrospinning equipment [82] utilized for conducting the experiments. This equipment incorporates a system designed to automate the production of three-dimensional matrices by precisely aligning nanofibers. The system comprises three modules: Module A, responsible for nanofiber formation through electrospinning; Module B, responsible for collecting the resulting nanofibers; and Module C, responsible for depositing the collected nanofibers. Additionally, a computational unit is included in the system to facilitate control and coordination.

Module A consists of a syringe containing the polymeric solution, connected to an injector bomb, which, in turn, connects to an electrospinning capillary tube with a positive polarity. This module is aligned perpendicular to the axis of the collector cylinders in Module B.

Module B comprises two coaxial collector cylinders/disks positioned perpendicular to the electrospinning tube, as depicted in Figure 5.33. Each cylinder is connected to an electrical motor, controlled by the computational unit, enabling continuous rotation. The cylinder surfaces are made of conductive material and can be negatively or neutrally charged. In this particular case, the voltage applied to the collector disks was -5 kV.

Module C incorporates a deposition table situated between the collector disks. It can execute both linear and rotational movements. The linear movement is parallel to the surface of the table and aligned with the axis of the electrospinning tube. The rotational movement occurs around the longitudinal axis of the table. The electrospun fibres are collected on the surfaces and in the spaces between these cylinders, as shown in Figure 5.33. The combined functionality of these modules ensures a continuous and automated electrospinning process, resulting in three-dimensional scaffolds with well-aligned nanofibers while maintaining control over the spacing between the fibres.

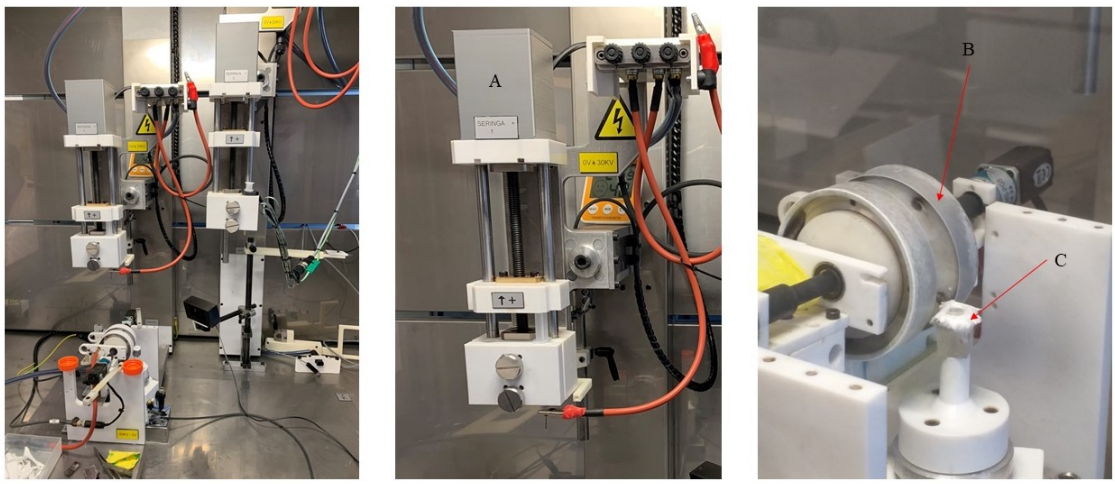

Figure 5.33: (a) 3D electrospinning system [82]; (b) Module A; (c) modules B and C. In these images, it is shown one of the AAF being fabricated.

Electrospinning parameters

The electrospinning parameters are essential for the success of the fabrication of the fibrous ring. These parameters have been optimized by the coordinator of the project Professor António Completo in previous works with the system. In table 5.9 are shown all the parameters of the electrospinning system used in the fabrication process.

Table 5.9: Electrospinning parameters used for construction E307.

Fabrication parameters	
Negative polarity	-5 kV
Positive polarity	+15 kV
Syringe diameter	12
Flow rate	3mL/h
Distance: needle to collector	110mm
Distance: between collectors	12mm
Z initial position	18mm
Collector speed	800
Needle	21G
Program	E307_1p403_35_3ml_10052023
Temperature and humidity	25ºC - 57%

Equipment programming/trajectories

The electrospinning system is programmed based on the ISO language (G-code). In this code, there are the trajectories that the system needs to follow in order to fabricate the fibrous ring. It was necessary to create a construction strategy that fulfilled the requirements of the AAF.

The construction strategy involved initiating the fabrication with a first layer of tangential lines (left side of Figure 5.34), conforming to the geometry of the ANP. This initial layer aimed to create a high fibre density in contact with the endplates, enhancing the adhesion between the fibres and the endplates. The construction proceeded by following the trajectory shown in Figure 5.34 (middle figure), designed to facilitate efficient height increment of the disc. For the final layer, the same trajectory as the first layer was employed, again with the objective of creating a higher fibre density to ensure better adhesion to the top endplate (depicted on the right of Figure 5.34).

In the middle trajectories shown in Figures 5.34, the fibres were not only oriented to gain height but also aligned to have good tensile strength. This alignment is crucial because, during the compression of the disc, the ANP undergoes compression and transfers a portion of the load to the AAF, which effectively contains it. The ability to achieve such a geometry was made possible by utilizing the 3D electrospinning system, which allowed for the alignment of fibres and the creation of the desired geometry simultaneously.

Alternative trajectories were explored in an attempt to construct the AAF. However, these trajectories proved to be unsuccessful in achieving the desired height. Some of the attempted trajectories even took more than a day to fabricate an AAF and not sufficient

height was achieved. Consequently, these trajectories were deemed impractical and were ultimately abandoned for the purpose of this project.

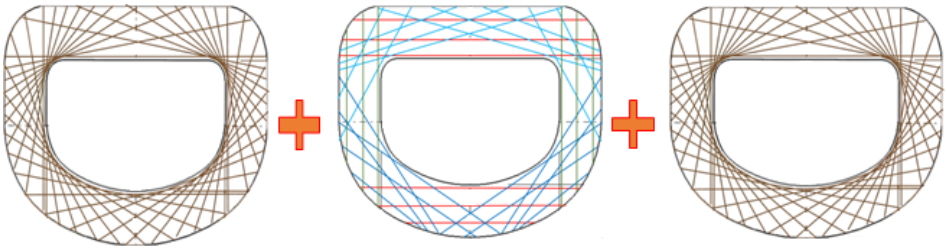

Figure 5.34: Construction E307 trajectories. On the left side the first layer, on the middle, the trajectory used to build height, and on the right side the last layer.

After the decision on how the fibres were going to be aligned, it was necessary to get the coordinates to manually create the program that the system was going to run. Since there was no automatic way to produce the program, it was necessary to create a 2D model of collector cylinders and the deposition table to scale, and then a 2D model of the endplates was imported and centred in the deposition table. The zero of the endplates was calculated and from there the coordinates for each trajectory were taken and the G-code was written. Table 5.10 is an example of the G-code used.

Figure 5.35 shows a disc being fabricated with the trajectory and G-code used. Each AFF fabricated had a mean thickness of 3.5 mm.

a) b) c)

Figure 5.35: A fabricated AAF where it is clearly seen the trajectories used for fibre deposition.

Hydrogel deposition

Following the fabrication of the AAF, the hydrogel is deposited into the central cavity left in the disc. For that, once the hydrogel is prepared, it is transferred to a syringe and carefully deposited into the disc cavity. After, a PCL+GEL solution is applied to the top endplate to "glue" the endplate to the disc and the disc is closed.

The process described above is visually shown in Figure 5.36, illustrating the sequential steps involved in the closure of the disc.

Table 5.10: Program (G-code) used for the fabrication of the AAF

E307 G-code program						
#200=0	N520 M2	X5.85	X4.75	G4 P1.1	X4 C-180	X5 C0
G90	O1001	C-100	C10	X5.65	G4 P40.3	G4 P40.3
#141= 12	G0 X4.25	G4 P1.1	G4 P1.1	C120	X5.4 C124	X6.75 C-60
#142= 12	C0	X5.75	X5.5	G4 P1.1	G4 P40.3	G4 P40.3
#182=1	G4 P1.1	C-110	C20	X5.4	X5.6 C90	X6.8 C-90
G4 P0.1	X4.75	G4 P1.1	G4 P1.1	C130	G4 P40.3	G4 P40.3
#200=0	C-10	X5.65	X6	G4 P1.1	X8.10 C62	X6.20 C-127
G4 P0.1	G4 P1.1	C-120	C30	X5	G4 P40.3	G4 P40.3
#121=-5	X5.5	G4 P1.1	G4 P1.1	C140	X5.14 C15	X6 C-18
G4 P0.1	C-20	X5.4	X6.4	G4 P1.1	G4 P40.3	G4 P40.3
#122=15	G4 P1.1	C-130	C40	X4.65	X8 C90	X5 C-180
G4 P0.1	X6	G4 P1.1	G4 P1.1	C150	G4 P40.3	G4 P40.3
#100=800	C-30	X5	X6.65	G4 P1.1	X4.6 C147	X5.6 C-148
G4 P0.1	G4 P1.1	C-140	C50	X4.25	G4 P40.3	G4 P40.3
F20000	X6.4	G4 P1.1	G4 P1.1	C160	X6 C-180	X6 C18
#151=3 G4 P0.1	C-40	X4.65	X6.75	G4 P1.1	G4 P40.3	G4 P40.3
#162=1	G4 P1.1	C-150	C60	X4.15	X4.6 C-147	X6.20 C127
G4 P0.1	X6.65	G4 P1.1	G4 P1.1	C170	G4 P40.3	G4 P40.3
#161=-0.5	C-50	X4.25	X6.65	G4 P1.1	X8 C-90	X6.80 C90
G4 P0.5	G4 P1.1	C-160	C70	G0 X9	G4 P40.3	G4 P40.3
G0 X15 Y0 C0	X6.75	G4 P1.1	G4 P1.1	C0	X5.14 C-15	X5.60 C148
G4 P3	C-60	X4.15	X6.4	M99	G4 P40.3	G4 P40.3
M98 P1001 L1	G4 P1.1	C-170	C80	G4 P0.1	X6.25 C0	X6.75 C60
M98 P1002 L1	X6.65	G4 P1.1	G4 P1.1	O1003	G4 P40.3	G4 P40.3
M98 P1003 L1	C-70	X4.1	X6.1	G0 X4 C0	X6.85 C-19	G0 X9
M98 P1001 L1	G4 P1.1	C-180	C90	G4 P40.3	G4 P40.3	C0
M98 P1002 L1	X6.4	G4 P1.1	G4 P1.1	X8.10 C-62	X7 C-143	M99
G0 X15 C0	C-80	G0 X9	X5.85	G4 P40.3	G4 P40.3	G4 P0.1
G4 P1	G4 P1.1	C0	C100	X5.6 C-90	X7 C143	
N490 #181= [#181 + 1]	X6.1	M99	G4 P1.1	G4 P40.3	G4 P40.3	
N500 M47	C-90	G4 P0.1	X5.75	X5.40 C-124	X6.85 C19	
N510 #200=1 G4P0.1	G4 P1.1	O1002	C110	G4 P40.3	G4 P40.3	

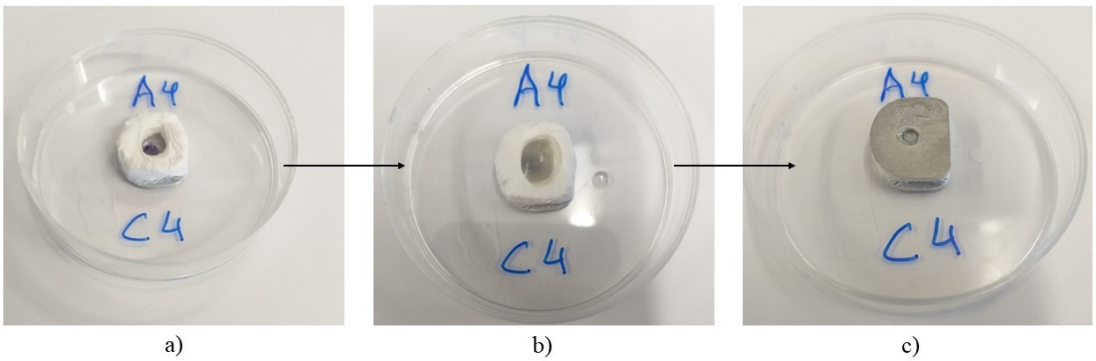

a) b) c)

Figure 5.36: Sequence of the hydrogel deposition process into the nucleus cavity for the Agarose variants. a) Disc ready for the hydrogel deposition. b) Hydrogel deposited in the nucleus cavity. c) Disc closed with the top endplate.

In the case of the AG+Col-MA hydrogel, an additional step is required. This hydrogel requires photopolymerization with UV light (Figure 5.37). Therefore, before closing the disc, UV light is applied to facilitate the crosslinking of the collagen, promoting gelation within the AG+Col-MA hydrogel.

Figure 5.37: Crosslinking of the AG+Col-MA hydrogel with the UV light

5.3.2.3 SEM analysis - Fiber diameter

Fibre diameter in the superficial layer was evaluated using scanning electron microscopy (SEM) with a Hitachi TM4000 plus instrument from Japan. The measurements were conducted in mode 3, with an accelerating voltage of 15 kV. The vacuum condition was set to standard, and the Backscattered-electron (BSE) detector was utilized for imaging and analysis. The equipment is presented in Figure 5.38 a).

One sample of the AAF was analysed. It was placed in the table of the equipment (Figure 5.38 (b)), and images at 30x, 120x, 400x, 1200x and 2500x of magnification were taken. With the sample in the SEM, the fibre diameter was measured manually in the equipment in different areas of the sample. For retrieved values, the mean and standard deviation was calculated.

5.3.2.4 Micro-CT analysis - Analysis of the AAF architecture

Micro-CT was executed in one AAF sample using the SkyScan1275 by Bruker Micro-CT (Figure 5.38 (c)). The sample was reconstructed, and projection and sectional images were performed in order to evidence the structural organization of fibres in the AAF sample.

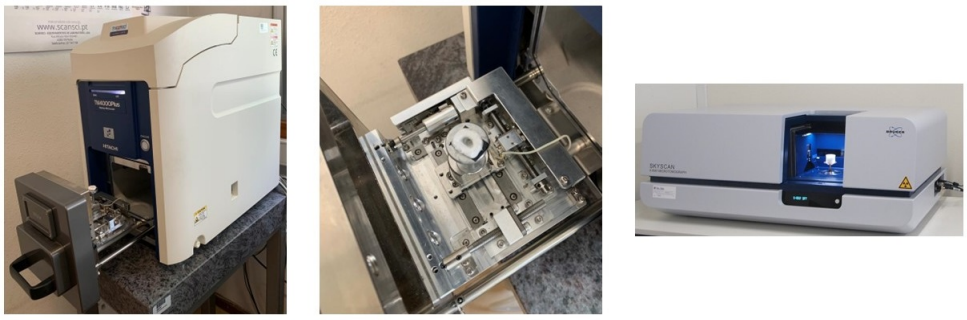

a) b) c)

Figure 5.38: a) SEM equipment (Hitachi TM4000 plus). b) AAF sample in the SEM table. c) Micro-CT equipment (SkyScan1275 by Bruker)

5.3.2.5 Mechanical tests

The mechanical characterization of the samples was carried out through a series of compression tests at different stages of fabrication and disc states. These tests were performed using the Shimadzu MMT-101N (Shimadzu Scientific Instruments, Japan) equipment (Figure 5.39 (a)).

To conduct the test, the sample was positioned at the base of the equipment, and the load cell was carefully lowered until it made minimal contact with the sample (Figure 5.39 (b)). The compression test was then initiated at a load speed of 1mm/min. The goal was to achieve a deformation between 15% to 20%, which corresponds to the typical deformation of the native intervertebral disc when subjected to loading.

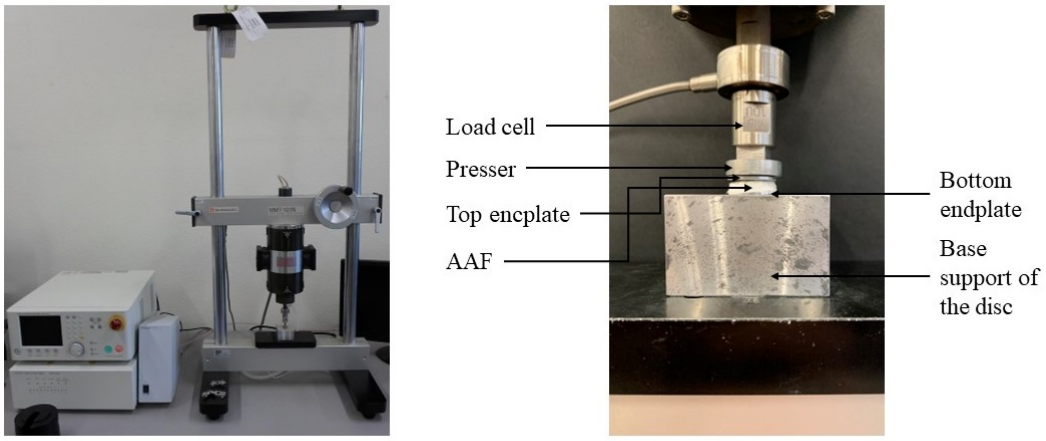

a) b)

Figure 5.39: Shimadzu MMT-101N. The equipment used to perform the compressive loading tests.

After the fabrication of the AAF (12 samples), a compression test was performed until a thickness of 2.6 mm was reached, corresponding to a deformation of approximately 15% of the nominal final disc thickness value (3 mm). These samples were used in the fabrication of the discs (without hydration), with their cores filled with three different

types of hydrogel. Three samples were used for each hydrogel type. These discs were also subjected to a simple compression test until a residual disc thickness of 2.6 mm. In the final stage, the discs were hydrated for 48 hours and then subjected to compression testing until a disc height of 2.6 mm was achieved.

The disc samples that exhibited inconsistent or non-conforming results in the previously described tests were excluded from the statistical analysis.

Based on these tests, force-thickness curves, stress-strain relationships, and stiffness-displacement profiles were established for the discs. With these curves, the Young modulus, stiffness, maximum force and maximum stress were calculated. For the calculations, it was used the theoretical area from the CAD models. The AAF area was 132.6 mm^2 and the disc total area was 211.3 mm^2.

Statistical Analysis

After having all the results of the parameter mentioned above, the statistical analysis of the result was performed. The mean, standard deviation and coefficient of variation were calculated for every group sample, with the goal of comparing of the results.

Additionally, a t-test was performed between different states of fabrication of the disc, independently of the hydrogel used, and a t-test between the different hydrogels used in the discs, at the non hydrated state.

This statistical analysis test is used to determine if there is a significant difference between the means of the sample groups. In this case is an independent t-test, due to the sample groups being in different parts of the fabrication of the disc, or being not hydrated. From this test, a p-value was obtained for each of the groups. This value indicates how the differences between the groups affect the output parameters. This is a calculated number that represents the probability to find a set of differences between group samples, with the initial assumption that there are no true differences. When the p-value$<$0.05 it means that in fact there are differences between the group samples in the output parameters, and these differences are statistically significant. When the p-value$>$0.05 it doesn't mean that there are no differences between the group samples, simply these differences are not statistically significant.

5.4 Results

5.4.1 SEM

The SEM analysis results revealed the superficial layer of fibres in the AAF, showcasing the aligned fibres in accordance with the construction trajectory employed (Figure 5.40).

By analyzing the SEM images (Figure 5.41), the fibre diameter was calculated, yielding a mean value of 1.75 µm with a standard deviation of 0.15. These measurements were obtained from two distinct areas of the AAF, ensuring a representative analysis of the fibre size and uniformity. These provide valuable insights and contribute to the overall understanding of the AAF's structural characteristics.

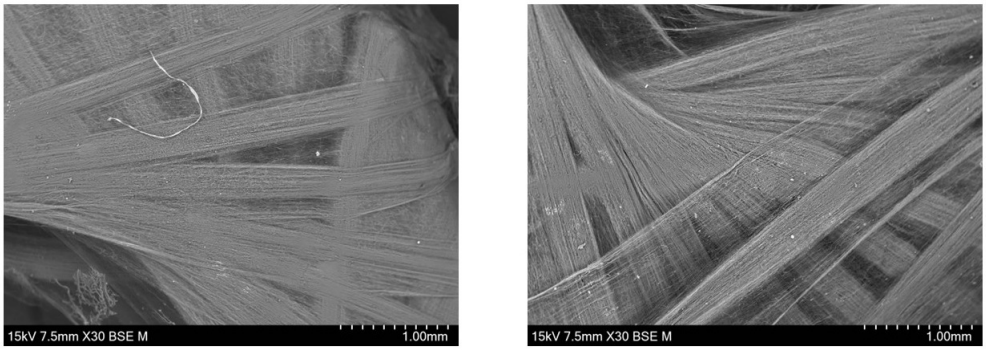

a) b)

Figure 5.40: Images resulted from the SEM analysis on one of the AAF. Both of the images were captured at 30x magnification.

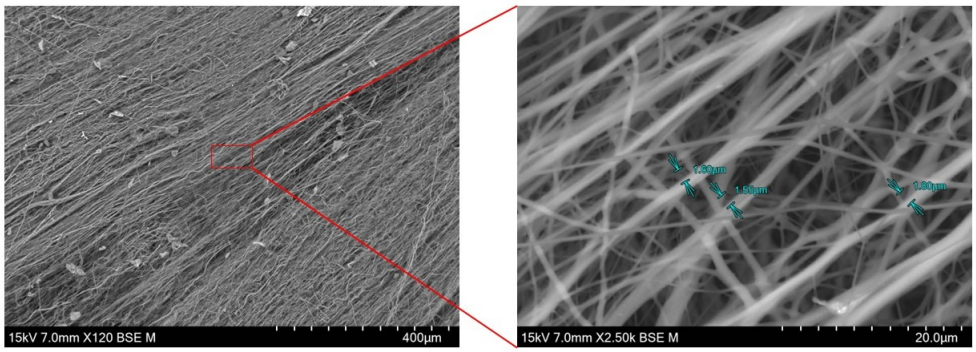

a) b)

Figure 5.41: Images resulted from the SEM analysis on one of the AAF. a) image was taken at 120x magnification. b) image was taken at 2500x magnification. b) image also has the measurements taken from the SEM.

5.4.2 Micro-CT

Figure 5.42, 5.43, 5.44 showcases the results of the AAF, before hydrogel deposition, in Micro-CT, providing insight into the fibre organisation and the cavity intended for hydrogel deposition. From the perspective view (Figure 5.42) and top view (Figure 5.43) is seen the geometry of the fibres used in the disc fabrication. Additionally, the anterior / posterior and medial / lateral cuts (Figure 5.44) reveal all the deposited layers that form the AAF, along with the designated hydrogel cavity. Each layer is a cycle of deposition in the 3D electrospinning system.

Based on these images, it is evident that the construction of the fabricated AAF aligns with the idealized trajectories. Previously in the SEM analysis, the top layer aligned with the defined trajectory, which is further confirmed by the Micro-CT analysis.

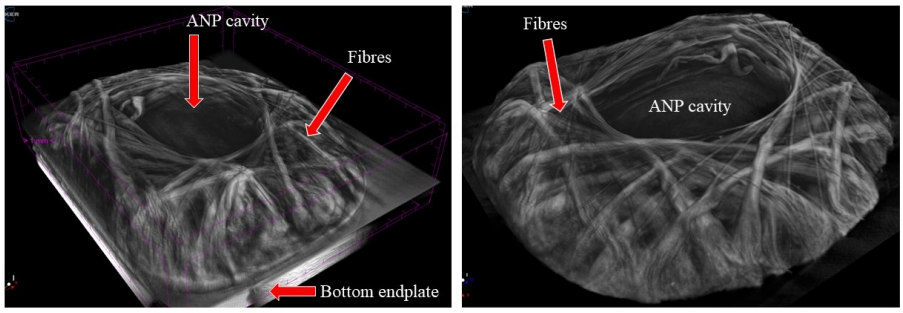

Figure 5.42: Images acquired from the Micro-CT. Both a) and b) images are a view in perspective of the AAF. a) showcases the cavity for the hydrogel deposition.

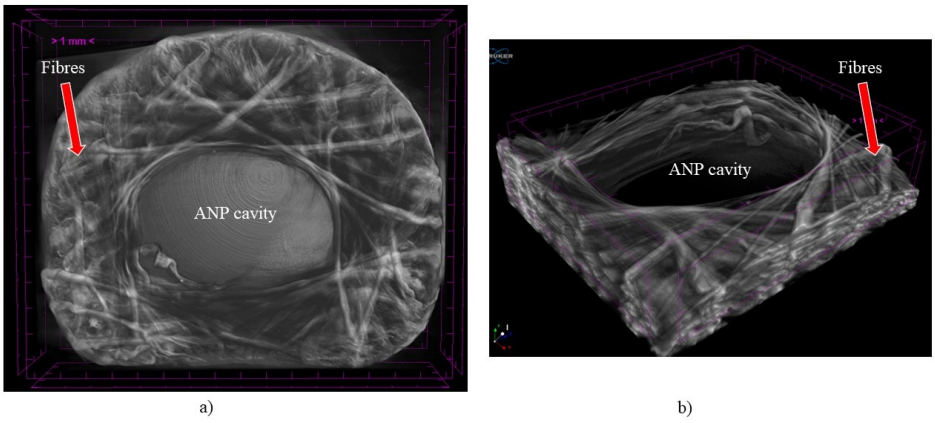

Figure 5.43: Images acquired from the Micro-CT. a) Top view from the fabricated AAF, b) AAF in perspective view with cuts to show the inside of the fibre construction.

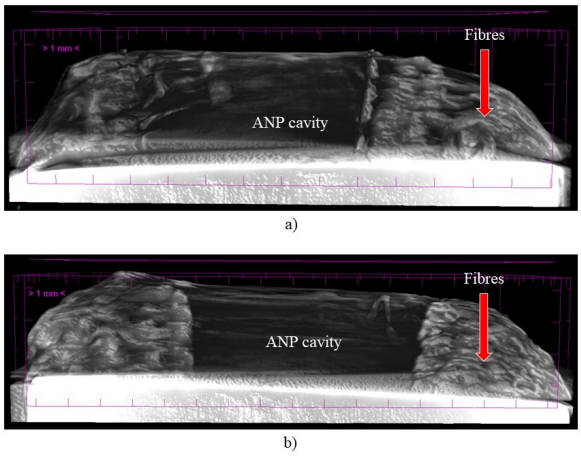

Figure 5.44: Images acquired from the Micro-CT. a) Anterior/posterior cut of the AAF, b) Medial/lateral cut of the AAF.

5.4.3 Mechanical test

AAF only samples

From the mechanical test, as mentioned, the force-thickness curve, stress-strain and stiffness-displacement were profiled. Figure 5.45 represents the results for AAF sample number 6 (referred to as A6), showcasing these profiles. Additionally, the stress-strain curve was analysed within the strain range of 10% to 20% to calculate the Young modulus by determining the slope of the trendline.

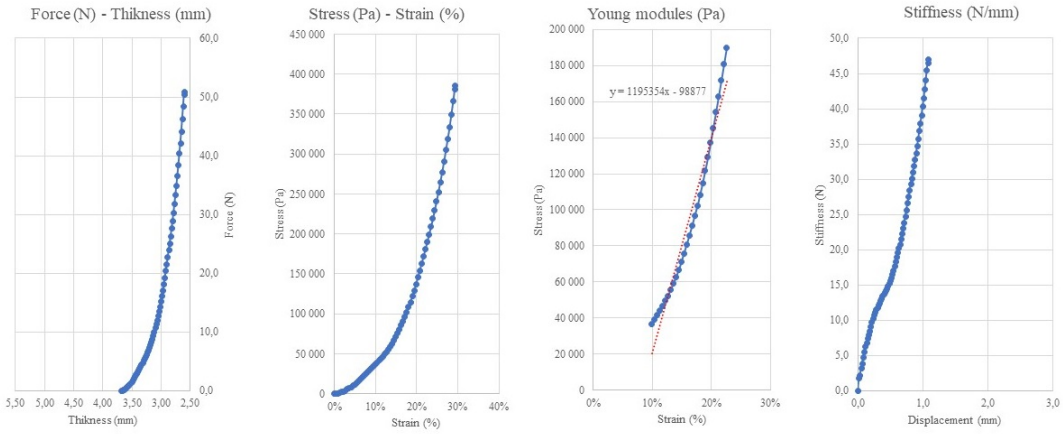

Figure 5.45: The result for the A6 sample. a) Force-Thickness plot. b) Stress-strain plot. c) Trendline to calculate the Young modulus. d) Stiffness.

This procedure was performed for all 12 samples of the AFF. Table 5.11 shows the results of maximum force, stiffness, Young modulus and maximum strain for all the samples, as well as the mean and standard deviation.

Table 5.11: Compressive tests on PCL80-GEL20 AAF samples up to a thickness of 2,6mm (15% of 3mm).

Sample	Maximum Force [N]	Stiffness [N/mm]	Young modules [Pa]	Maximum Stress [Pa]
A1	10.5	5.3	122560	79585
A2	36.0	19.4	349875	272820
A3	5.9	3.0	74063	44640
A4	28.0	13.0	124553	212332
A6	50.4	46.4	1195354	381489
A7	3.5	3.4	102992	26452
A8	2.8	3.4	118540	21427
A9	2.9	1.6	35206	22322
A10	5.1	2.5	79493	38892
A11	2.9	1.8	41562	22015
A12	4.9	3.8	108631	37034
Mean	**13.9**	**9.4**	**213893.5**	**105364.5**
Standard Deviation	**16.5**	**13.5**	**336124.1**	**125013.4**

From the analysis of Table 5.11, sample A6 demonstrated the best performance in the test. It had a maximum force of 50.4 N, a stiffness of 46.4 N/mm, a Young modulus

of 1195354 Pa and could withstand maximum stress of 381489 Pa. On the other hand, sample A9 had the lowest Young modulus with 35206 Pa and the lowest stiffness with 1.6 N/mm. Sample A8 has the lowest maximum stress 21427 Pa and the lower maximum force applied 2.8 N.

The observed variation in these parameters studied is reflected in the standard deviation, which is higher than the mean in all parameters studied. This high dispersion indicates that there was significant variability in the values obtained for each sample. This dispersion in the results could be attributed to external factors, such as temperature and humidity of the room where the system is, which may influence the mechanical properties of the samples despite using the same fabrication parameters and construction strategies. Control of the humidity and temperature of the room could give more consistent samples.

Non hidrated disc samples

From the mechanical test, as said, the force-thickness curve, stress-strain, and stiffness-displacement were profiled. Figure 5.46 presents the results for a complete disc sample number 6 (referred to as C6), showcasing these profiles. This disc had the NP cavity filled with AG hydrogel, the disc was not hydrated in this test.

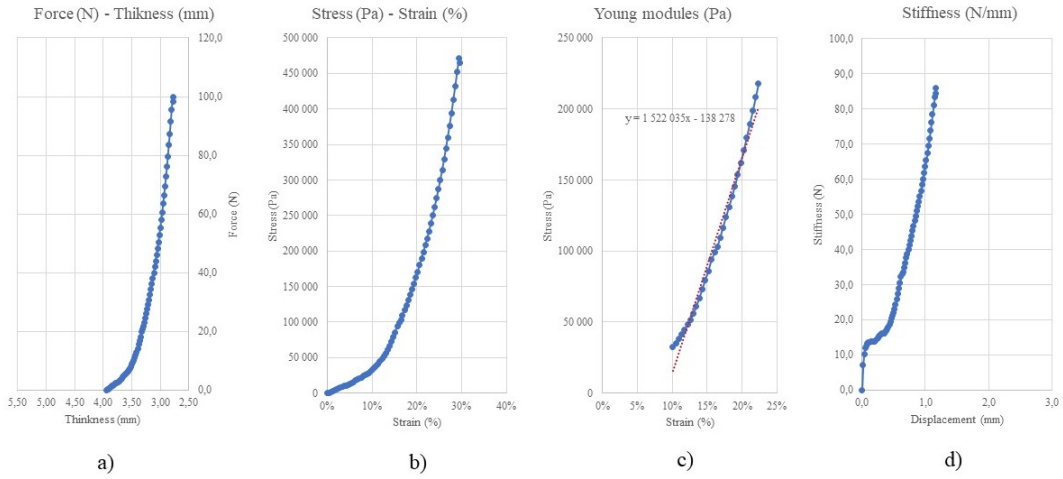

Figure 5.46: The result for the C6 sample. a) Force-Thickness plot. b) Stress-strain plot. c) Trendline to calculate the Young modulus. d) Stiffness.

Table 5.12 shows the results for the complete disc with their respective hydrogels, for the same study parameters as in the previous case. The mean, standard and deviation were calculated for each of the different hydrogels used. There are missing samples that were excluded from the study, which is going to be explained later.

Analysing Table 5.12, the overall performance of the discs with the agarose hydrogel, was the best when compared with the other, it had a mean maximum force of 88.5 N, a mean stiffness of 73.8 N/mm and a mean Young modulus of 1469589 Pa. The sample with the best performance was the C6. The AG+Alg hydrogel discs had the lowest mean values for the maximum force 42.7 N, and the AG+Col-MA had the lowest values in terms of mean stiffness, with 36.6 N/mm, and Young modulus, with 635470 Pa.

Table 5.12: Simple compression tests on disc specimens up to a thickness of 2.6 mm (15% of 3mm) without hydration.

Sample	Maximum Force [N]	Stiffness [N/mm]	Young modules [Pa]	Maximum Stress [Pa]	Hydrogel
C4	40.7	37.7	748,847	192,093	75% agarose + 25% Alginate
C12	44.7	40.7	684,512	210,932	75% agarose + 25% Alginate
Mean	**42.7**	**39.2**	**716,680**	**201,512**	-
Standard Deviation	**2.8**	**2.2**	**45,492**	**13,322**	-
C6	98.4	84.4	1,522,036	464,779	100% agarose
C8	78.7	63.2	1,417,142	371,711	100% agarose
Mean	**88.5**	**73.8**	**1,469,589**	**418,245**	-
Standard Deviation	**13.9**	**15.0**	**74,171**	**65,809**	-
C1	54.2	21.5	387,533	255,867	75% Agarose + 25% Collagen
C2	99.2	51.7	883,407	468,471	75% Agarose + 25% Collagen
Mean	**76.7**	**36.6**	**635,470**	**362,169**	-
Standard Deviation	**31.8**	**21.3**	**350,636**	**150,334**	-

The variation in between samples C4 and C12, which utilized the AG+Alg hydrogel, exhibited the lowest standard deviation among all the group samples. None of the parameters analyzed presented a standard deviation higher than 10%, indicating a high level of consistency in the fabrication of the complete disc. On the other hand, samples C1 and C2 displayed higher standard deviation values, being the lowest 41% of the mean. During the tests on these samples, it was observed that the collagen component of the hydrogel was not fully crosslinked, resulting in some hydrogel spilling from the bottom endplate. This hydrogel had to be crosslinked with the UV light, but it may not have adequately reached the bottom layer, leading to incomplete crosslinking. This event likely contributed to the dispersion in the results obtained for these samples. The samples were examined and were apparently good to hydrate and repeat the test.

Hydrated disc samples

From the mechanical test, as mentioned, the force-thickness curve, stress-strain, and stiffness-displacement were profiled. Figure 5.47 presents the results for a complete disc sample number 6 (referred to as C6h), showcasing these profiles. This disc had the NP cavity filled with AG hydrogel, the disc this time was hydrated in this test.

Table 5.13 shows the results for the complete disc with their respective hydrogels, with the same study parameters as in the previous case, hydrated this time. The mean and standard deviation were calculated for each of the different hydrogels used.

Analysing Table 5.13, the overall performance of the disc with the agarose hydrogel was better when compared with the others. It had a mean maximum force of 79.7 N, a mean stiffness of 72.4 N/mm and a mean Young modulus of 1376802 Pa. The sample with the best performance was the C6h.

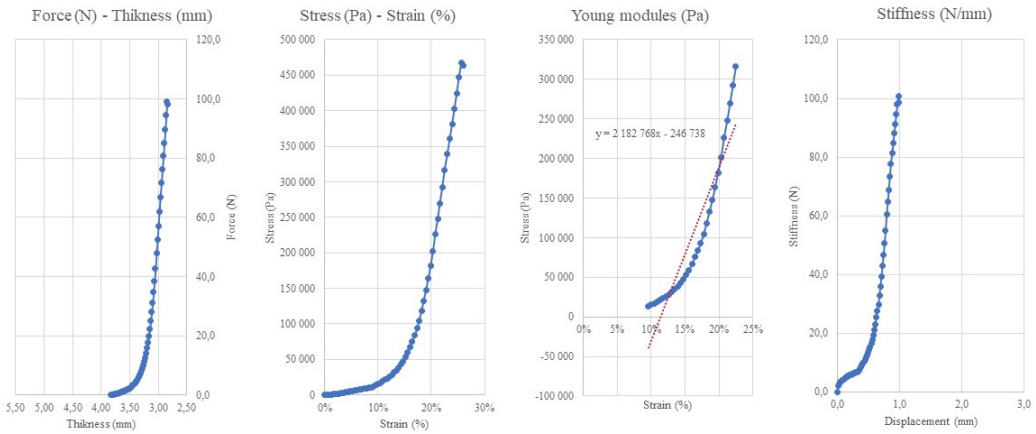

Figure 5.47: The result for the C6h sample. a) Force-Thickness plot. b) Stress-strain plot. c) Trendline to calculate the Young modulus. d) Stiffness.

Table 5.13: Simple compression tests on disc specimens up to a thickness of 2.6 mm (15% of 3mm) with hydration.

Sample	Maximum Force [N]	Stiffness [N/mm]	Young modulus [Pa]	Maximum Stress [Pa]	Hydrogel
C4h	35.1	34.6	607,055	165,400	75% agarose + 25% Alginate
C12h	40.6	47.0	1,033,457	191,432	75% agarose + 25% Alginate
Mean	**37.8**	**40.8**	**820,256**	**178,416**	-
Standard Deviation	**3.9**	**8.8**	**301,512**	**18,407**	-
C6h	98.2	98.7	2,182,728	463,661	100% agarose
C8h	61.2	46.0	570,875	288,943	100% agarose
Mean	**79.7**	**72.4**	**1,376,802**	**376,302**	-
Standard Deviation	**26.1**	**37.3**	**1,139,752**	**123,544**	-
C1h	49.9	28.1	620,633	146,330	75% Agarose + 25% Collagen
C2h	85.3	48.3	237,427	402,744	75% Agarose + 25% Collagen
Mean	**67.6**	**38.2**	**429,030**	**274,537**	-
Standard Deviation	**25.0**	**14.3**	**270,968**	**181,312**	-

Samples excluded from the analysis

Several samples were excluded from the statistical analysis during the mechanical tests based on predefined criteria. These criteria included the presence of visible defects in the samples that prevented further testing, as well as cases where the performance of the complete disc was found to be similar to that of the samples with only the AAF. In such cases, it indicated that the addition of the hydrogel did not improve the disc's performance as expected. Table 5.14 provides an overview of the excluded samples along with the corresponding reasons for their exclusion.

Among the samples, only one AAF sample, A5, was excluded from the analysis. The remaining excluded samples were complete discs, indicating that the issues were related to the fabrication or deposition of the hydrogel. In certain cases shown in Table 5.14, the hydrogel cavity was not completely filled despite appearing so initially. This incomplete filling was attributed to contractions that occurred during the cooling process of the hydrogel. This effect could prevent the disc from performing as expected in the test

Table 5.14: Samples excluded from statistical analysis - Exclusion criteria (visible defect in the annulus or maximum force values identical to or lower than the compression test of the annulus only)

Sample	Maximum Force [N]	Status or Material	Reason for exclusion
A5	3.1	AAF only (PCL+Gel)	Exclude - visible defect (detachment)
C10	6.3	75% Agarose + 25% Alginate	Exclude - Values identical to only the AAF
C11	4.5	100% Agarose	Exclude - Values identical to only the AAF
C9	1.6	75% Agarose + 25% Collagen	Exclude - Values less than just the AAF
C3	6.8	75% Agarose + 25% Alginate	Exclude - Values identical to only the AAF
C7	3.7	100% Agarose	Exclude - Values identical to only the AAF

parameters. When compressing the disc to a thickness of 2.6 mm, the hydrogels were not being compressed due to the incomplete filling of the cavity. Consequently, the values obtained were similar to those of the AAF samples alone. Appendix B showcases the results of all the studied parameters for the samples that were excluded from the analysis. It's important to note that even after their exclusion from the statistical analysis, these samples were subjected to compressive tests under all the previous conditions.

Result comparison between AAF only and non hydrated discs

In Table 5.15 are the comparison between the result of only the AAF and the complete disc.

Table 5.15: Variation between only the annulus and the annulus nucleus (disc).

Sample	Maximum Force [N]	Stiffness [N/mm]
C4	+45%	+189%
C12	+815%	+970%
Mean	**+430%**	**+579%**
C6	+95%	+82%
C8	+2681%	+1763%
Mean	**1388%**	**+922%**
C1	+416%	+307%
C2	+175%	+166%
Mean	**296%**	**236%**

The results demonstrate a noticeable increase in the maximum force and stiffness for all samples. This finding is significant as it indicates that the addition of the hydrogel ANP resulted in improved performance of the disc. Even when the AAF alone did not exhibit the best performance in terms of the studied parameters, the incorporation of the ANP hydrogel "levelled the field" among samples within the same group. This is evident when comparing the increments observed in samples C6 and C8.

Sample A8, consisting of only the AAF, exhibited considerably lower compression values compared to sample A6. However, with the addition of the ANP hydrogel, the properties of samples C8 and C6 became closer together. Specifically, sample C6 demonstrated a 95% increase in maximum force and an 82% increase in stiffness, while sample C8 showed a remarkable 2681% increase in maximum force and a 1763% increase in stiffness.

Result comparison between non hydrated and hydrated discs

In Table 5.16 are the comparison between the result of non hydrated discs and hydrated discs.

Table 5.16: Variation between non hydrated disc and hydrated disc.

Sample	Maximum Force [N]	Stiffness [N/mm]
C4	-14%	-8%
C12	-9%	+15%
Mean	**-12%**	**+4%**
C6	0%	+17%
C8	-22%	-27%
Mean	**-11%**	**-5%**
C1	-8%	+30%
C2	-14%	-7%
Mean	**-11%**	**+12%**

The results indicate that disc hydration had a slight negative impact on disc performance. The mean maximum force exhibited a decrease of approximately 11% to 12%, while the stiffness decreased by 5% in the agarose hydrogel group. On the opposite side, the AG+Alg hydrogel group showed a slight improvement of 4%, and the AG+Col-MA hydrogel group demonstrated an increment of 12% in stiffness.

Statistical analysis - t-test

With all the previous results obtained, the t-test analysis was performed. The t-test was performed for stiffness at 2.6mm and maximum force to the AAF-only, non hydrated disc and hydrated disc samples. Additionally, a third t-test was performed on the different types of hydrogel used in the discs.

In table 5.17, are presented the results of the t-test for the stiffness at 2.6 mm of thickness for the AAF-only. the non hydrated disc and the hydrated disc. As shown, the addition of the ANP in the disc has a significant impact on the disc stiffness, and that is proved by this analysis, $p<0.05$, in this case, is 0.004. As seen above the stiffness is improved with the addition of the ANP, and this statistical test proves that that improvement is significant. In the second case, analysing the hydration effect in the disc, it can be concluded that there is no significant impact on the disc stiffness, $p>0.05$ in this case 0.901.

Table 5.17: T-test for stiffness at 2.6mm [N/mm] thickness.

Sample	AAF only	Non hydrated disc	Hydrated disc
A1/C1	5.3	21.5	28.1
A2/C2	19.4	51.7	48.3
A4/C4	13.0	37.7	34.6
A6/C6	46.4	84.4	98.7
A8/C8	3.4	63.2	46.0
A12/C12	3.8	40.7	47.0
		AAF vs. Disc	Non hydrated disc vs. Hydrated disc
Significance (p<0.05)		**0.004**	**0.901**

In Table 5.18 are presented the results of the t-test for the maximum force at 2.6 mm of thickness for the AAF-only, the non hydrated disc and the hydrated disc. As shown, the addition of the ANP in the disc has a significant impact on the disc maximum force, and that is proved by this analysis, $p<0.05$, in this case, is 0.002. The addition of the ANP has even more impact on the maximum force than on the stiffness, improving the output parameters in both cases. In the second case, analysing the hydration effect in the disc, this time it can be seen that there is some impact in the output parameters ($p=0.037$). This time the effect is on the negative side, the hydration decreased the performance, and this test proves it statistically.

Table 5.18: T-test for the maximum force [N] at 2.6mm thickness.

Sample	AAF only	Non hydrated disc	Hydrated disc
A1/C1	10.5	54.2	49.9
A2/C2	36.0	99.2	85.3
A4/C4	28.0	40.7	35.1
A6/C6	50.4	98.4	98.2
A8/C8	2.8	78.7	61.2
A12/C12	4.9	44.7	40.6
		Ring vs. Disc	Non hydrated Disc vs. Hydrated
Significance (p<0.05)		**0.002**	**0.037**

The last t-test was performed to compare the effect of the different hydrogels used to fabricate the ANP. In Table 5.19 are presented the results. In this test is shown that there is only one study parameter that the output was impacted with the use of a different hydrogel. It was the case of the comparison between the AG+Alg and AG hydrogels. There was a variation in the Young modulus output which is proved by the $p=0.017$, which means there is a significant statistical impact on the studied parameters. There was a higher Young modulus when using the AG hydrogel compared with the AG+Alg hydrogel. The rest of the studied parameters did not have significant output changes with the use of the different types of hydrogel.

Table 5.19: T-test without hydration .

Hydrogels comparison	Stiffness [N/mm]	Young modulus between 10 to 20% [Pa]	Maximum Tension [Pa]
AG+Alg vs AG	0.215	**0.017**	0.161
AG+Alg vs AG+Col-MA	0.881	0.820	0.345
AG vs AG+Col-MA	0.385	0.220	0.776

5.5 Discussion

The results from the mechanical tests show some interesting findings about the fabricated models. The tests were performed in different phases of the fabrication of the disc with only the AAF, the complete disc not hydrated and the complete disc hydrated. Within the complete disc, there was the division between the hydrogels used, agarose, agarose and alginate (AG+Alg), and finally agarose and collagen (AG+Col-MA).

There were some interesting findings in the results obtained from the AAF-only samples. First, the mean Young modulus for the samples was 213893Pa. This was a compressive Young modulus. As previously mentioned, the behaviour of the AAF is different when in traction or compression, but [69] during compressive testing, achieved a mean Young modulus of 7 MPa for PCL fibres, meaning that improvements in the mechanical properties of the AAF are feasible. Another interesting finding was the highly dispersed values found for the models. The standard deviation in all the cases is higher than the mean value. Strangely the electrospinning parameters, the solution, and the used trajectories were the same for all the samples. The possible explanation for this is that the parameter that is harder to control, temperature and humidity, is a factor that influences the morphology of the fibres [75]. Hence a possible explanation for the differences between samples in terms of mechanical properties.

The results of the discs with the hydrogel indicate an increase in the mechanical capabilities of the disc with the insertion of the hydrogel. Sample C8 was the best case in terms of increasing the mechanical capabilities with the insertion of the hydrogel, with an increase of 2681% in the maximum force, and a 1763% in the stiffness. As a mean value, the best sample group still had an increase of 1388% in maximum force and 922% in stiffness. This is also proven in the t-testes that were performed to compare the significance in the stiffness and maximum force between the AAF-only and the non hydrated disc. The p=0.04 and p=0.02, respectively for this case. The hydrogel that had the best performance was the agarose. It had the highest values of all of the studied parameters. It is interesting to note that the stiffness of the best-performing sample was the C6 with 84.4 N/mm, and the same samples had the highest Young modulus of 1522036 Pa.

In this phase of the mechanical testing, it was noted that not all the discs had the same improvement in performance with the insertion of the hydrogel. As presented in the result, some of the samples were excluded from the statistical analysis due to the fact that the disc had basically the same performance when it was the AAF-only. These results were surprising. A plausible explanation would be the fact that the deposition of the hydrogel in the ANP cavity was not consistent. This means that the cavity could have not been totally filled, since the test result there did not indicate a failure in the disc, but it did show an underperformance until the desired displacement. Prior to

testing, it was noticed that there was a contraction in the samples, more in ones than in others, which could cause the supposed underfill of the discs. This could also be a parameter to take into account in future fabrications.

Another attention to take is when using the AG+Col-MA hydrogel. During the mechanical testing, one of the samples with this hydrogel had some of the hydrogels run between the bottom endplate and the AAF. That means that the crosslink of the collagen was not completely achieved. The crosslink with the UV light was made just on the top side of the hydrogel and was not strong enough to crosslink the whole hydrogel. In the future, there is a necessity to cross-link the hydrogel through the top and bottom. This only happens to one of the AG+Alg samples but is something to take into account when working with hydrogels that cross-link through photopolymerization.

The last phase of the fabrication was the hydration of the samples with PBS. The result of these samples showed that the hydration of the samples, for the most part, did not improve the output of the studied parameter. That is shown in the t-test made to the stiffness of the disc before and after hydration, the p=0.901 is higher than the significance. On the contrary, the t-test to the maximum force showed that the hydration had a significant influence on the output parameter, for the negative side, with the p=0.037. In this case, the values of the output parameter decreased, which meant that the hydration of the samples had a negative impact on the maximum force that the samples can withstand.

With the same statistical analysis, it was proven that the influence of the output parameter when comparing the different hydrogels used was not significant. The only case that was significant in the output parameter was the t-test between the AG and the AG+Alg hydrogel, in which there was a significant change in the studied parameter. The parameter was the Young modulus and a p=0.017. In general, that confirms that the hydrogel type didn't influence the performance of the disc in a significant way.

The performance of the fabricated disc still needs to be compared with the native IVD. The best-performing disc in terms of stiffness was the C6h with 98.7 N/mm. This value is far from the necessary to replace the native IVD. The native IVD has a stiffness for the same deformation of around 637.5 N/mm [20]. The same happens when comparing the maximum loads to this 20% of deformation. The best-performing disc in terms of the maximum load was the c6 with 98.4 N of force. For the same 20% deformation, the native IVD had a force of 602 N applied [20]. This proves that the disc at this stage of development does not have the necessary mechanical properties to replace the native IVD.

Since the goal is to fabricate a cervical disc to mimic the native IVD, and the results for stiffness and loads are significantly less than the native IVD, comparing this fabricated disc with the ones available in the market is redundant. The fabricated disc does not perform as well as these ones [48–51, 61] in terms of mechanical properties, stiffness and load-bearing capabilities. Has an example the [51] has a stiffness of 733 N/mm.

Overall, it was expected this difference between the disc developed in the project, the native IVD and the artificial discs available in the market. The numerical simulations preview this occurrence (model AnF_L_A) in terms of stiffness and maximum load and the experimental phase confirmed it. The intent was to prove the possibility of this fabrication method and to find room for improvement.

Intentionally blank page.

Chapter 6

Conclusions and future work

6.1 Conclusions

The electrospinning method has gained popularity in tissue engineering to develop scaffolds to mimic the native IVD. This process allows producing complex structures, with aligned fibres, that can change the mechanical properties of these scaffolds. The process is controlled by the electrospinning parameters that can change the morphology of the fibres, and affect the mechanical properties. These parameters can always be tuned to optimise the morphology of the fibres for the desired application.

The combination of the process with the use of hydrogels can allow endless possibilities and applications. An example is this present project. The hydrogels have a lot of tunability as well as the possibility to blend different compatible polymers to produce a final product with the wanted characteristics.

This project presented a study on the design and fabrication of an artificial cervical disc using the combination of a 3D electrospinning system and hydrogel techniques. To accomplish this it was necessary to develop 3D models of the disc and characterise the models using computational simulations, in order to explore the model possibilities prior to the fabrication. Through the computational simulations, it was possible to choose the model and to understand the behaviour of the model with different material properties. This was made in order to guide the rest of the experimental phase.

Prior to the fabrication of the disc, an exploratory phase of hydrogels preparation was performed to try to formulate a hydrogel solution that had the necessary mechanical properties and mimic the native NP. Also, the hydrogel had to be manageable in order to be able to gel inside the designated area in the disc, in contact with the fibres of the AAF, but at the same time not escape through them or degrade their mechanical properties. This last part was accomplished with the fabrication of the agarose-based hydrogel. Unfortunately, and that is mentioned in the discussion, the properties were not the desired [2].

The fabrication of the AAF with the electrospinning was accomplished too. Although the mechanical properties were not the desire [2]. The geometry used to construct the AAF has possibilities to improve and better mechanical properties could be achieved, using the same material solution. The use of different solutions or blends of solutions to be used to fabricate the AAF is also another possibility [12].

It was possible with this project to fabricate an experimental artificial cervical disc. The disc had the expected behaviour, of the AAF and the ANP working together. The

ANP increased the compression properties that the AAF-only didn't have, and that was shown in the results. The increase in the maximum force was 1388% for the best hydrogel, and the stiffness was increased by 922%. In the best-performing group sample, the disc with the 100% agarose had a mean stiffness of 73.8N/mm which was significantly lower compared to the 600N/mm of the native IVD [20].

The overall goal of the project was accomplished. There is a final prototype of the artificial disc, fabricated using the proposed methods, it was mechanically characterised and set a benchmark for the continuity of the exploratory works. There is room for improvement, and this work serves to highlight that this concept can still be enhanced in terms of materials and geometry in order to achieve the behaviour of the native IVD.

6.2 Future work

As said in the conclusion there is some room for improvement.

The 3D electrospinning system used has the capability to optimize the fibre geometry in the AAF, which could allow a better performance of the AAF. The use of different polymer solutions or blends could give better mechanical properties to the fibrous structure and still be biocompatible.

The optimization of the hydrogel, or even the use of different types of hydrogels, synthetics for example, could help to improve the disc performance. The optimization of the deposition and fabrication of the hydrogels need to improve in order to get more consistency of the fabricated discs. One of the problems with the work was that some samples had to be excluded due to this fact and that consistency needs to improve, to save money and resources.

These optimizations and more exploration could one day give us the chance to achieve the construction of an artificial disc using this 3D electrospinning system, which was key for this project.

Appendix A

Mechanical properties of the AFF-only and disc sampels

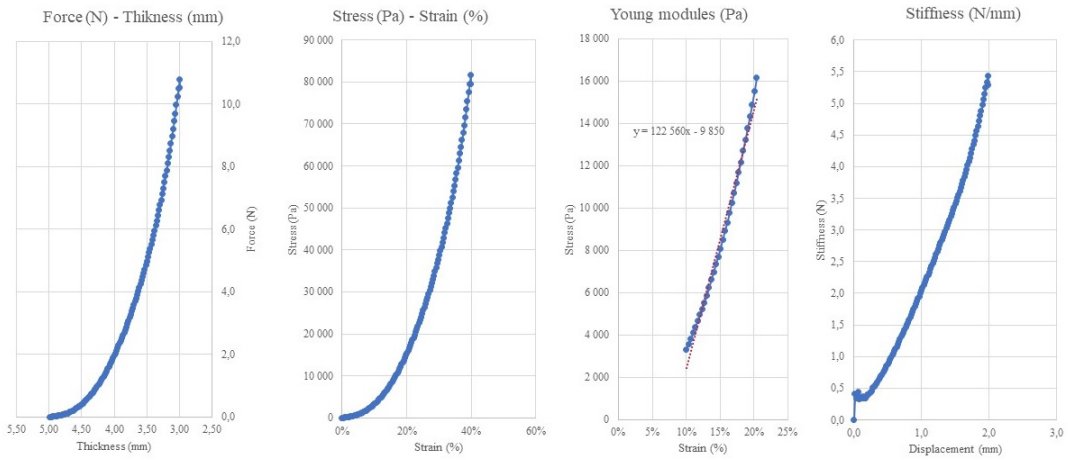

Figure A.1: The plotted results for the A1 sample.

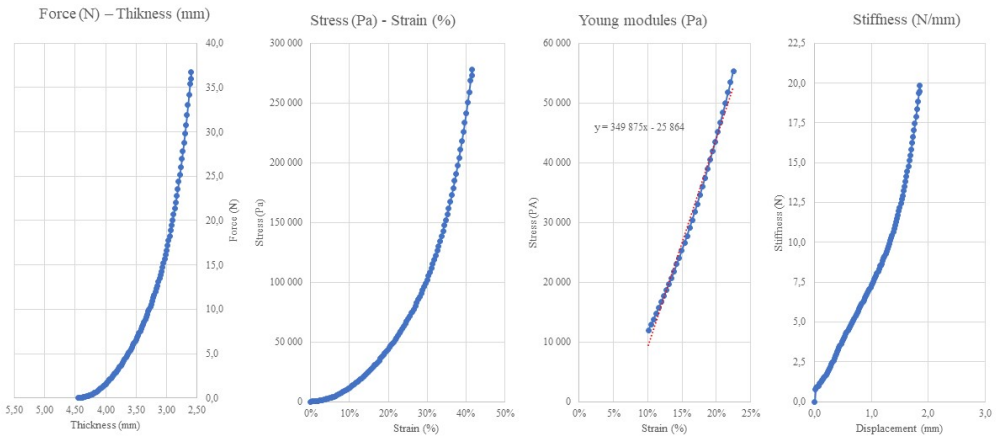

Figure A.2: The plotted results for the A2 sample.

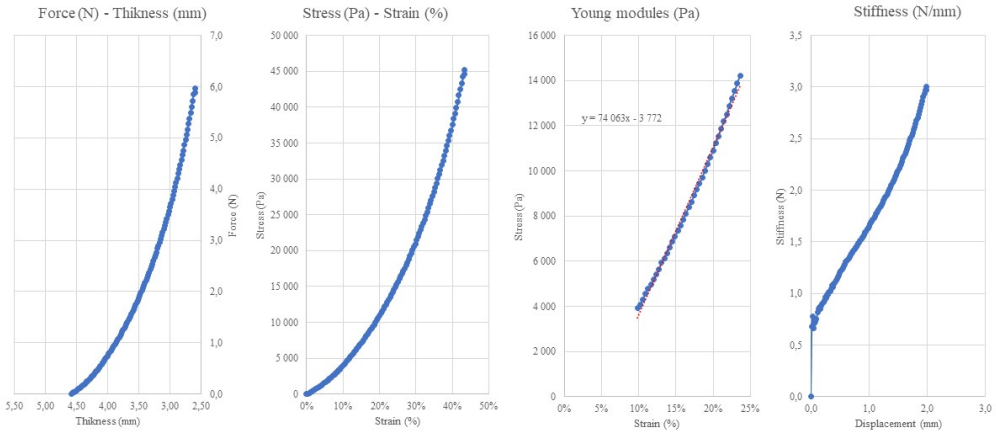

Figure A.3: The plotted results for the A3 sample.

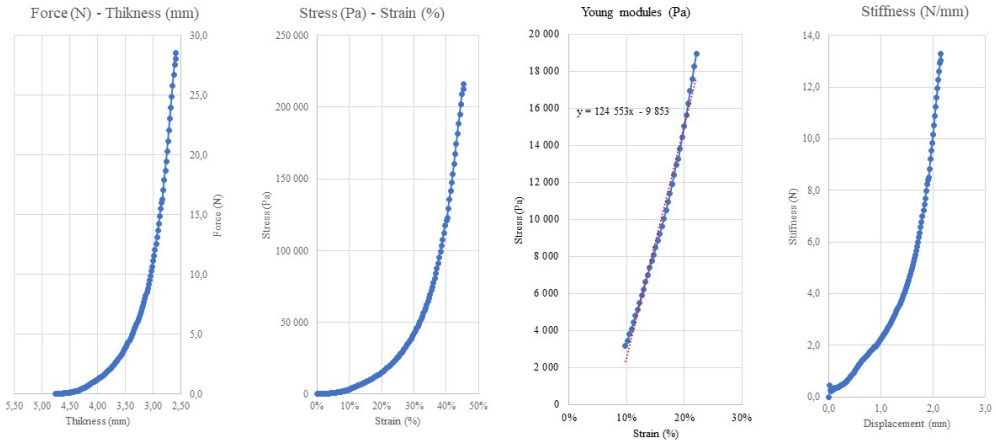

Figure A.4: The plotted results for the A4 sample.

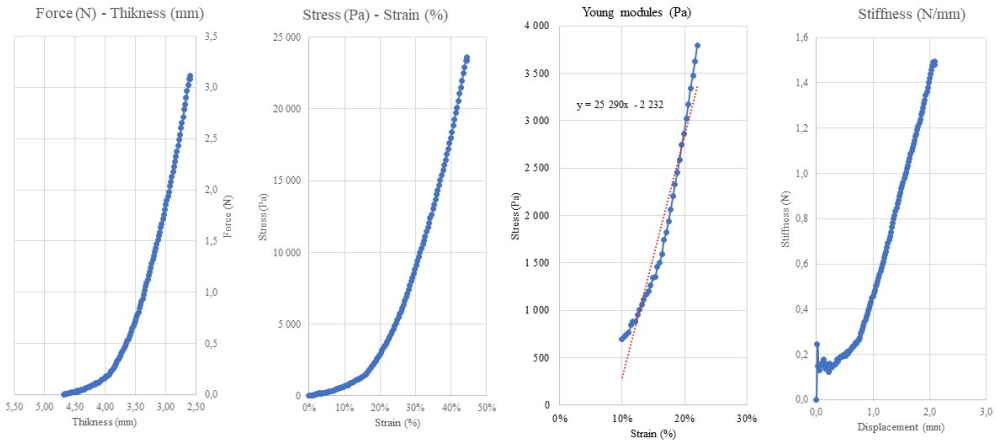

Figure A.5: The plotted results for the A5 sample.

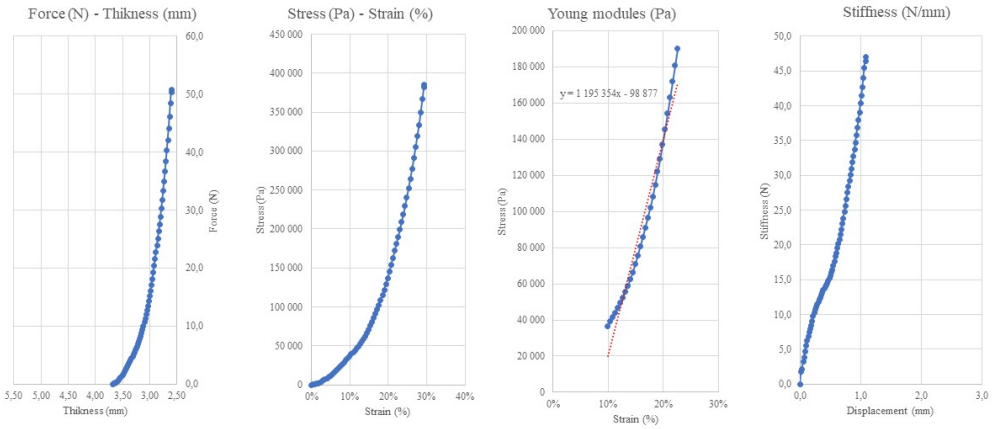

Figure A.6: The plotted results for the A6 sample.

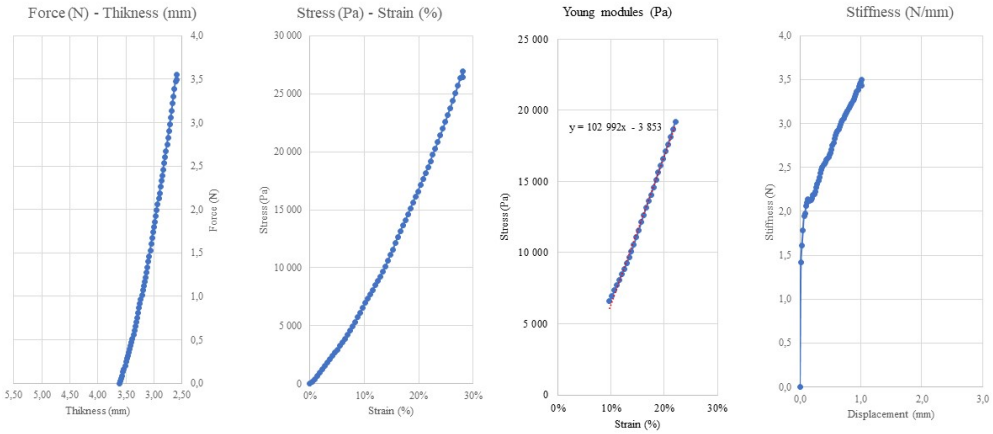

Figure A.7: The plotted results for the A7 sample.

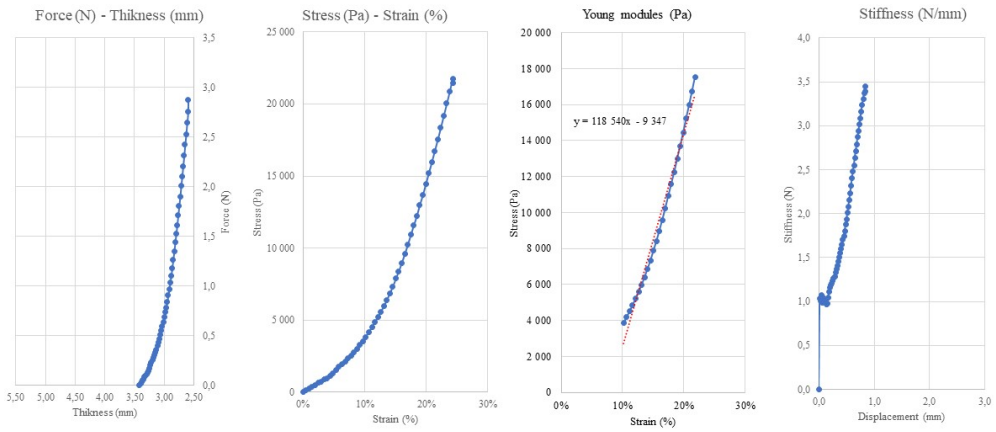

Figure A.8: The plotted results for the A8 sample.

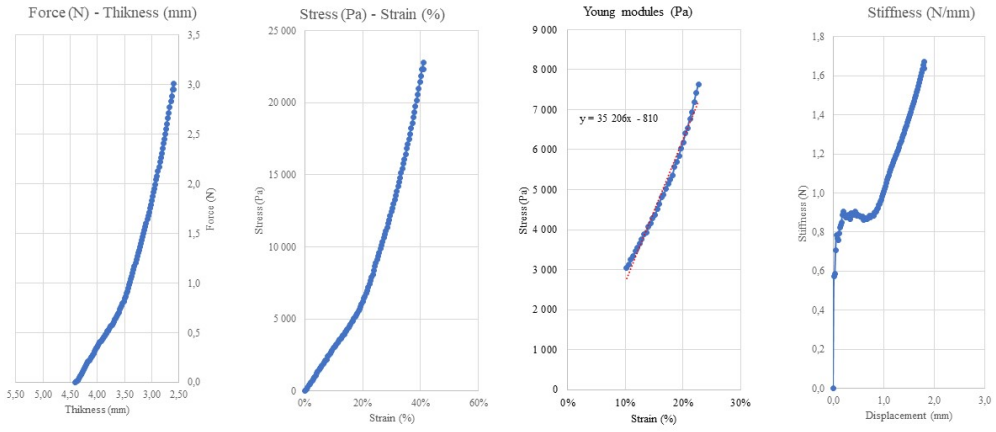

Figure A.9: The plotted results for the A9 sample.

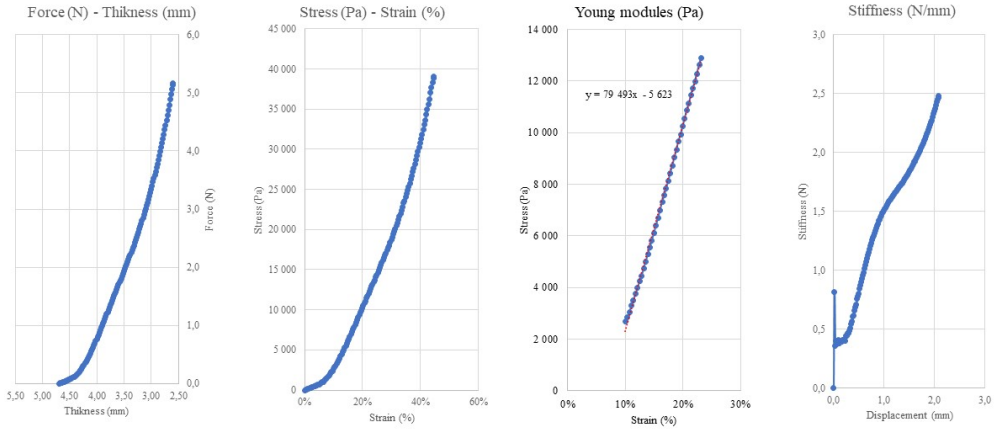

Figure A.10: The plotted results for the A10 sample.

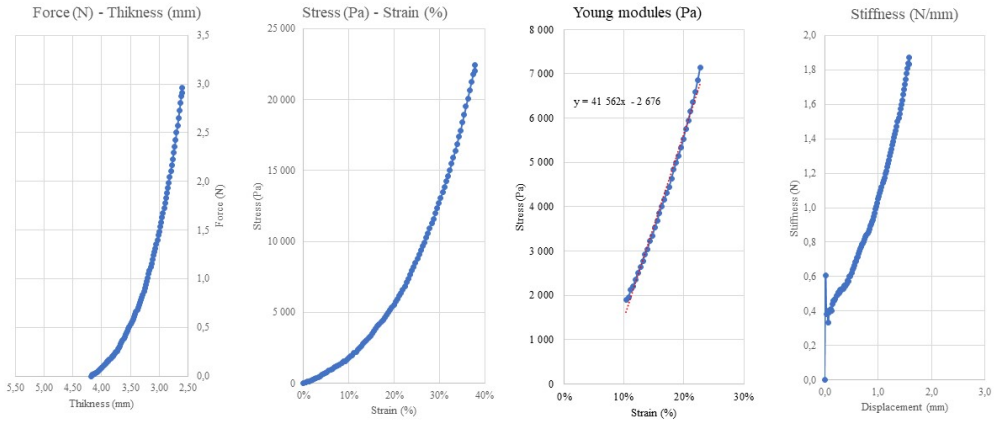

Figure A.11: The plotted results for the A11 sample.

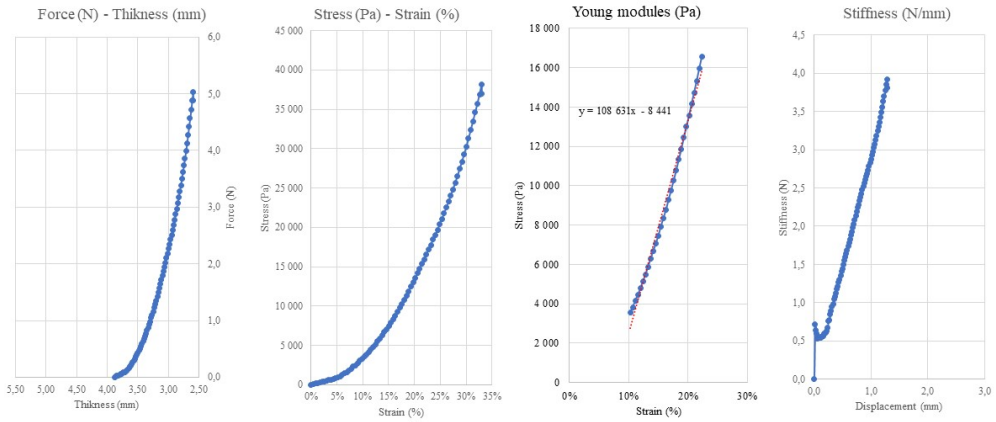

Figure A.12: The plotted results for the A12 sample.

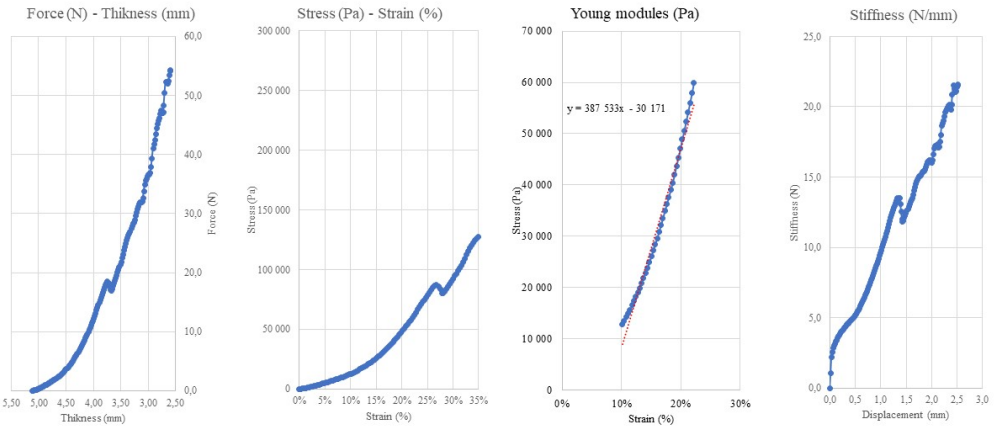

Figure A.13: The plotted results for the C1 sample.

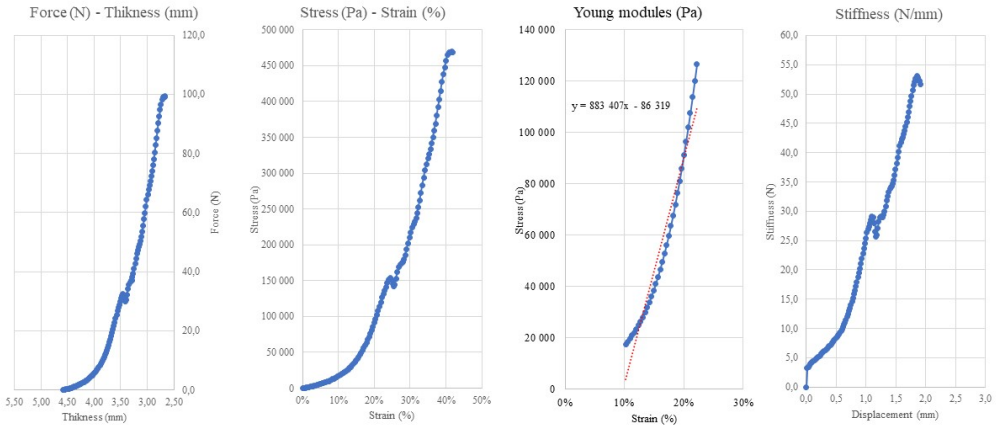

Figure A.14: The plotted results for the C2 sample.

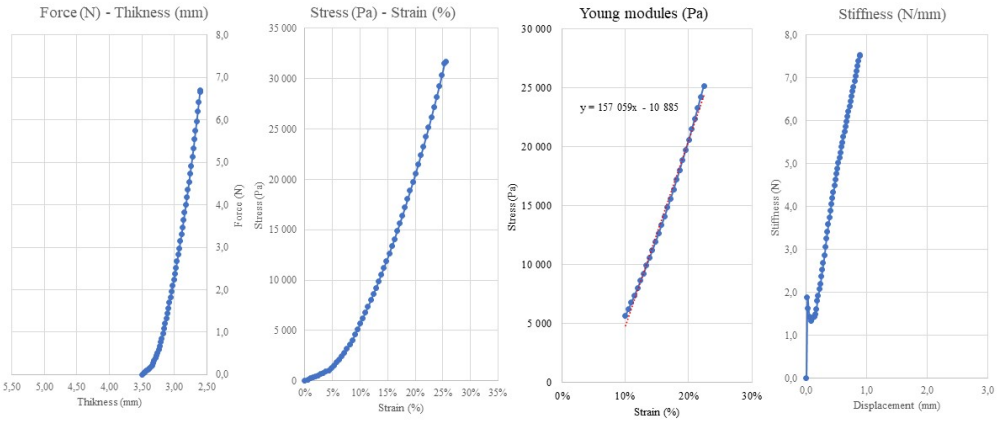

Figure A.15: The plotted results for the C3 sample.

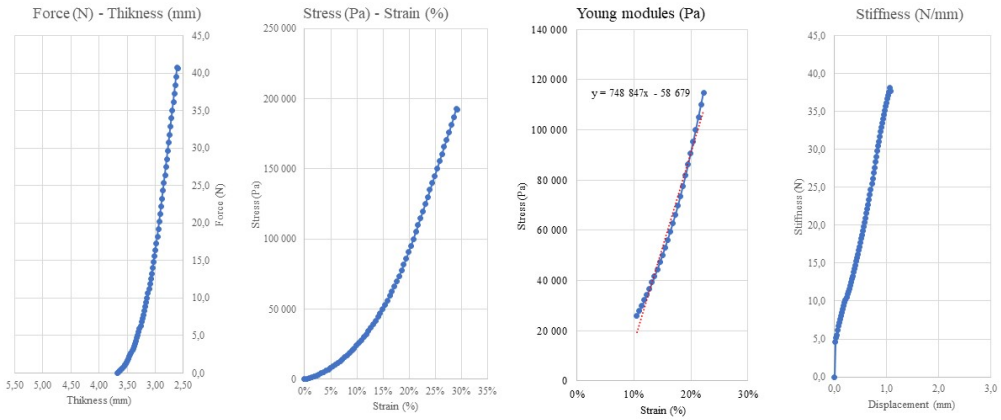

Figure A.16: The plotted results for the C4 sample.

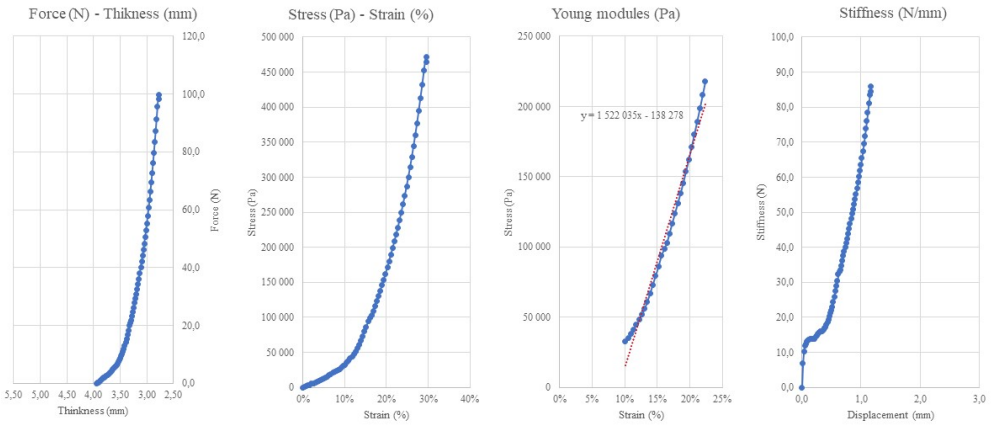

Figure A.17: The plotted results for the C6 sample.

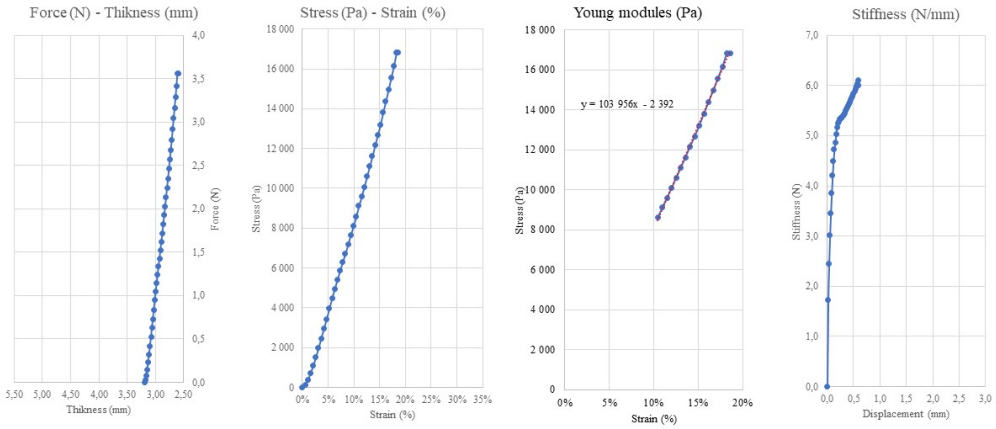

Figure A.18: The plotted results for the C7 sample.

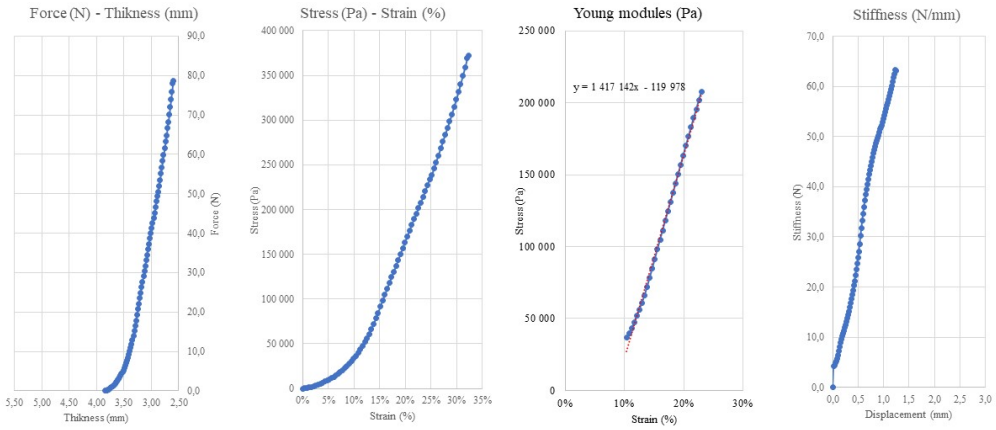

Figure A.19: The plotted results for the C8 sample.

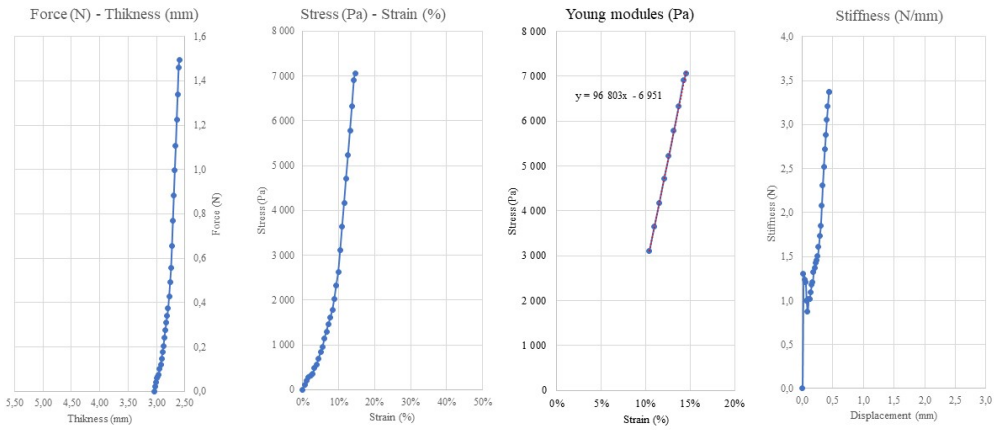

Figure A.20: The plotted results for the C9 sample.

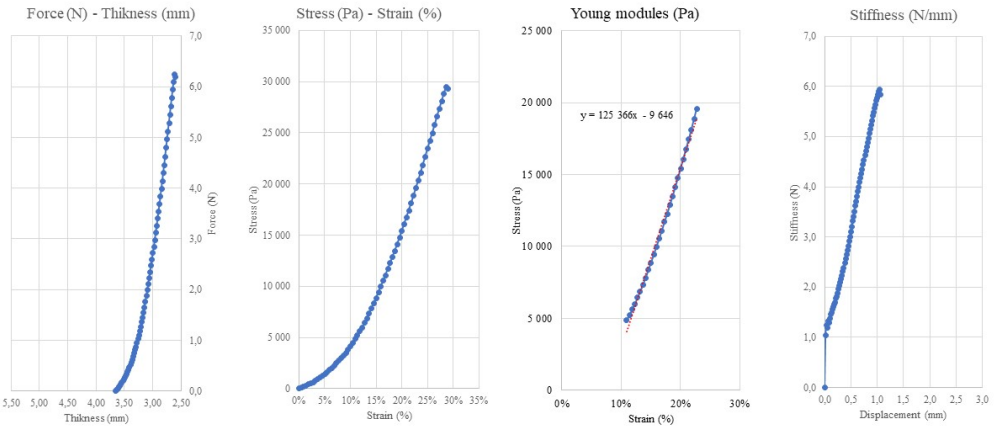

Figure A.21: The plotted results for the C10 sample.

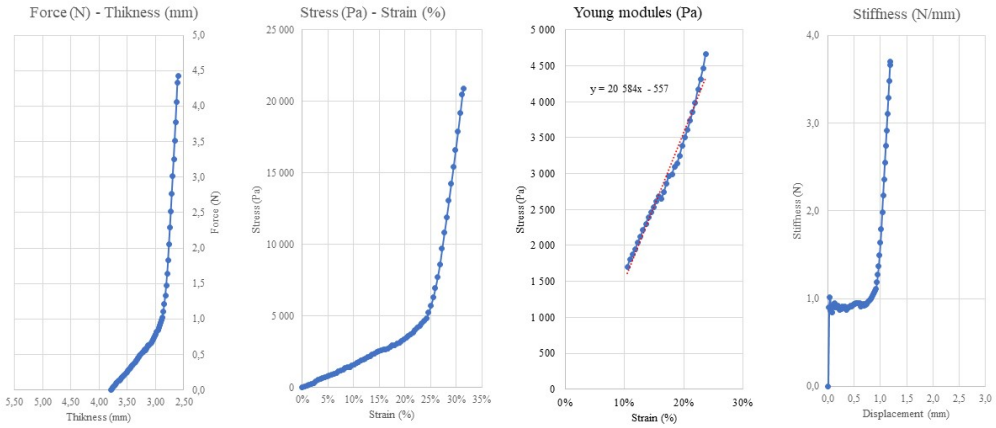

Figure A.22: The plotted results for the C11 sample.

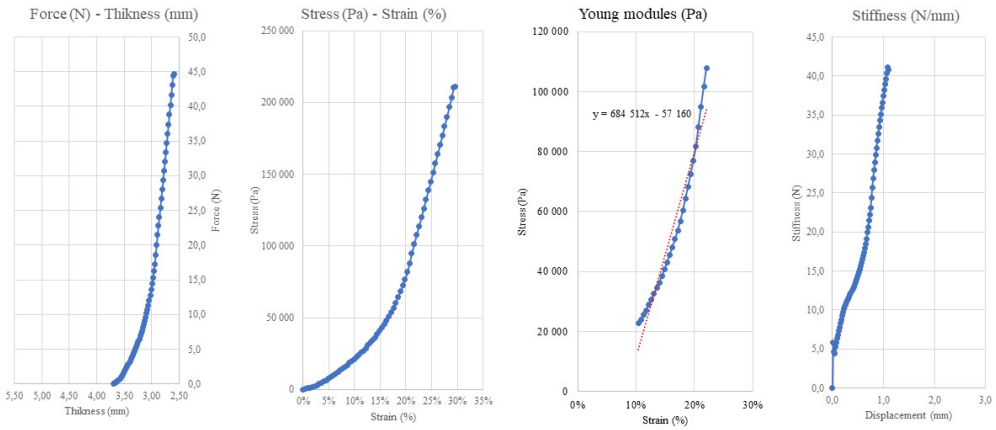

Figure A.23: The plotted results for the C12 sample.

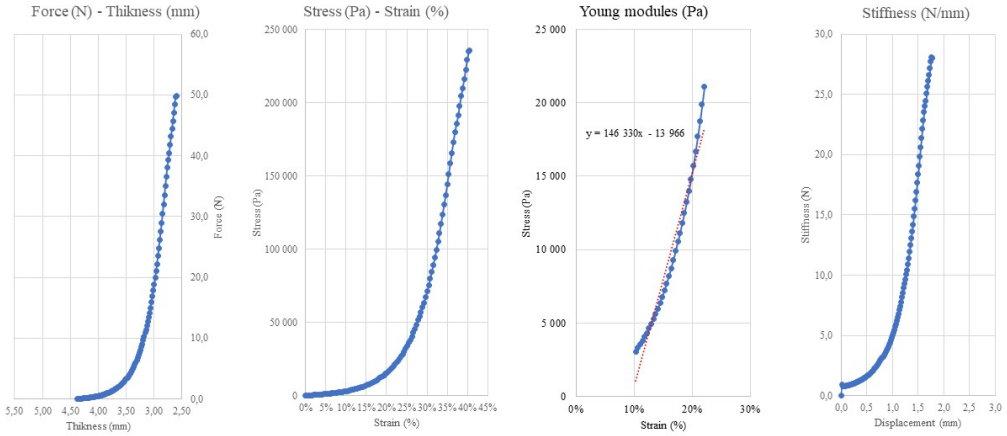

Figure A.24: The plotted results for the C1h sample.

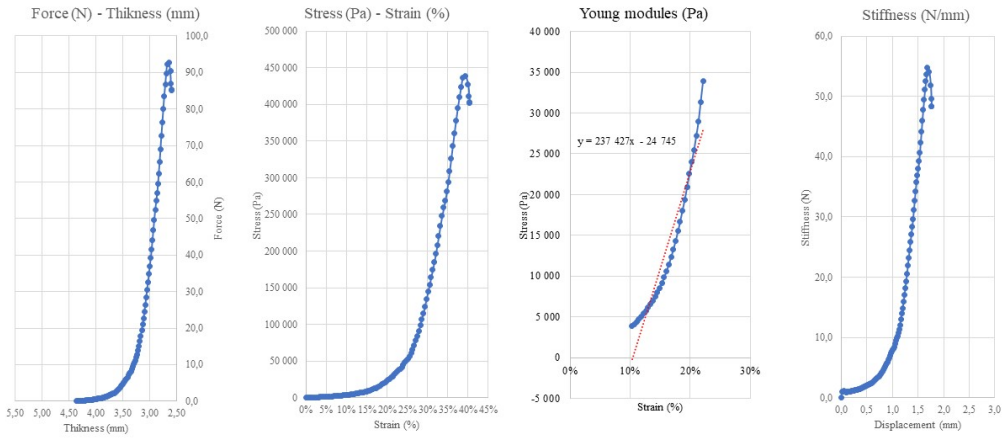

Figure A.25: The plotted results for the C2h sample.

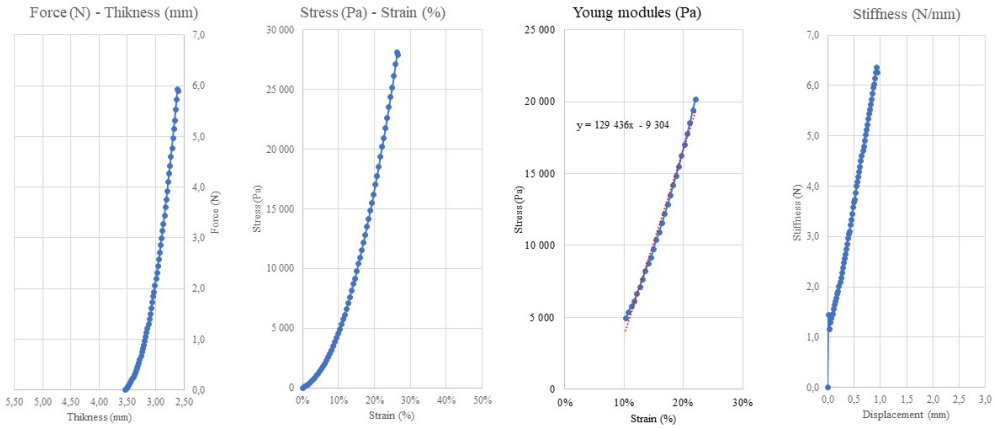

Figure A.26: The plotted results for the C3h sample.

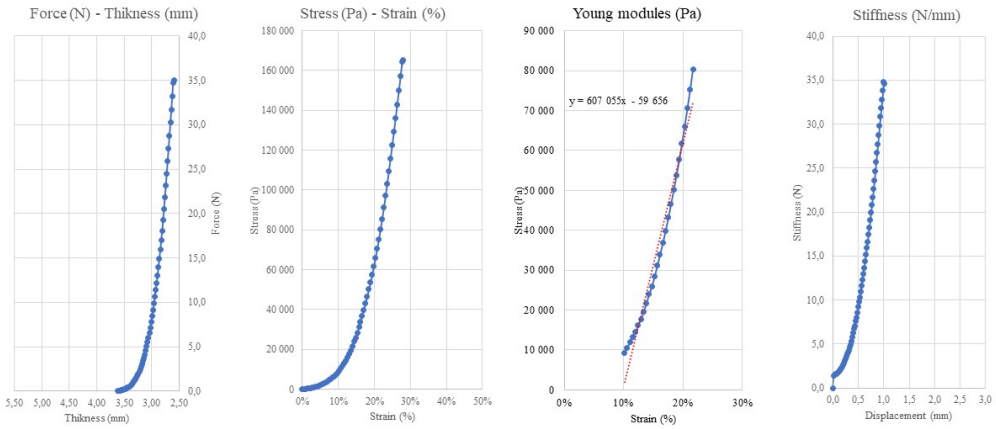

Figure A.27: The plotted results for the C4h sample.

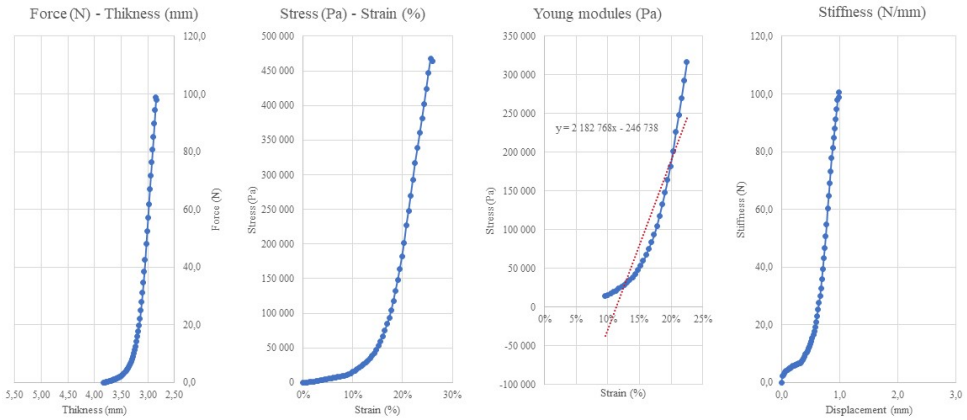

Figure A.28: The plotted results for the C6h sample.

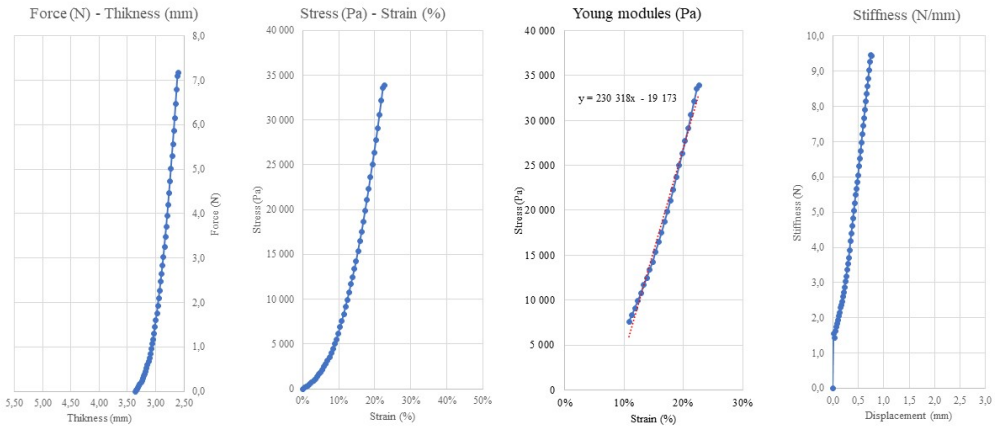

Figure A.29: The plotted results for the C7h sample.

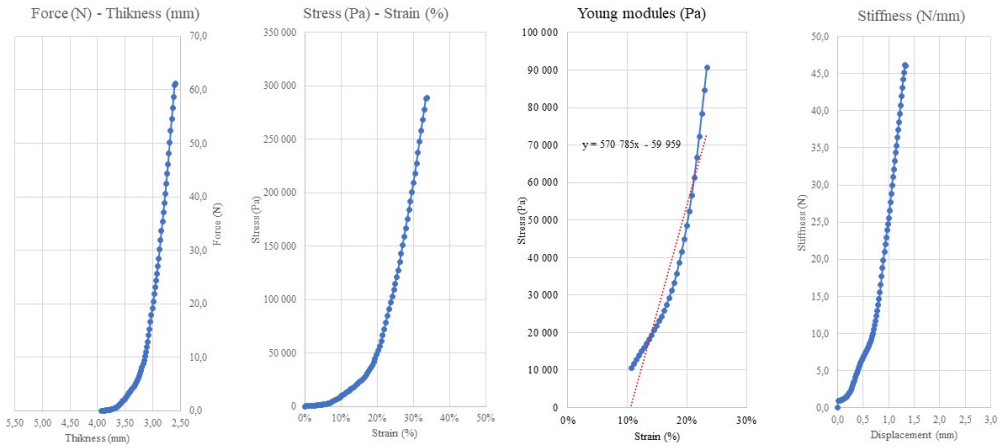

Figure A.30: The plotted results for the C8h sample.

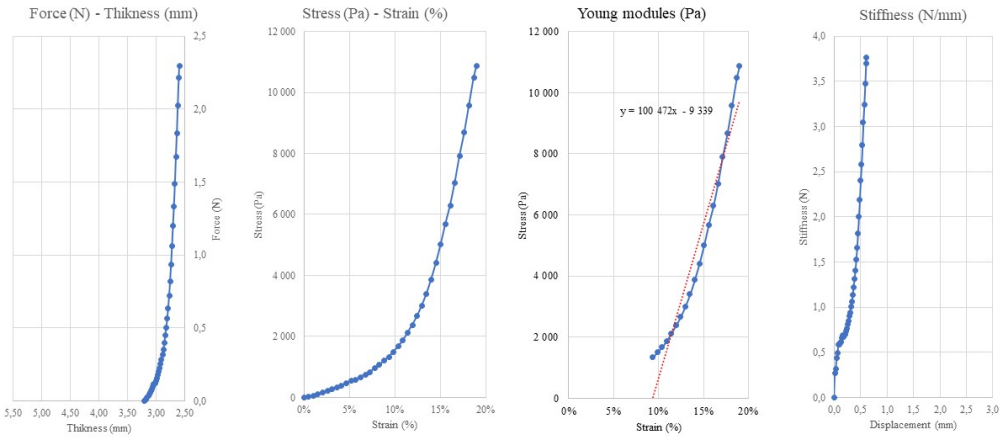

Figure A.31: The plotted results for the C9h sample.

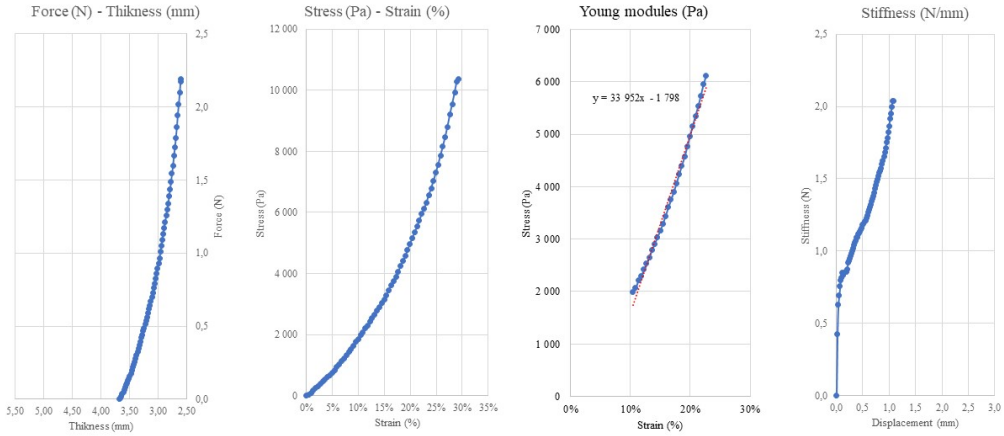

Figure A.32: The plotted results for the C10h sample.

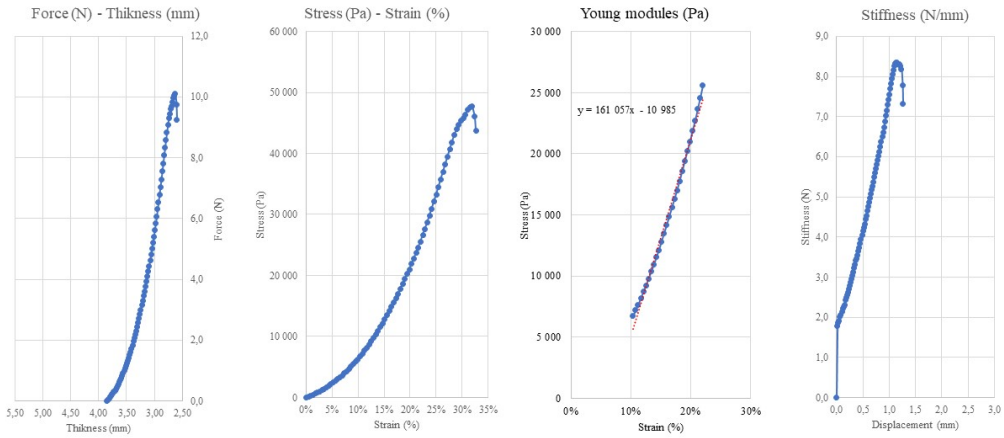

Figure A.33: The plotted results for the C11h sample.

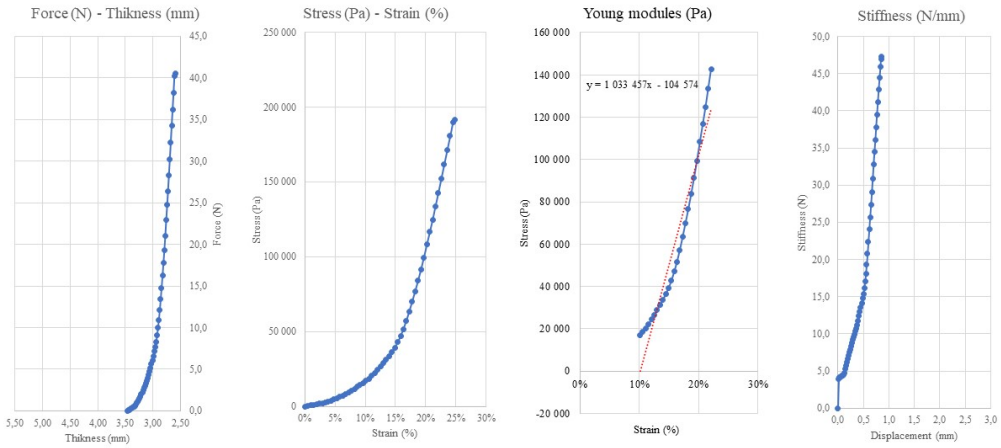

Figure A.34: The plotted results for the C12h sample.

Appendix B

Summary of the mechanical properties of the excluded samples

Table B.1: Simple compression tests on the disc up to a thickness of 2.6mm (15% of 3mm) without hydration.

Sample	Maximum Force [N]	Stiffness [N/mm]	Young modulus between 10 and 20% [Pa]	Maximum Stress [Pa]	Hydrogel
C10	6.3	5.8	125,366	29,285	75% Agarose + 25% Alginate
C3	6.8	7.5	157,069	31,727	75% Agarose + 25% Alginate
C7	3.7	6.0	103,956	16,845	100% Agarose
C11	4.5	3.7	20,584	20,899	100% Agarose
C9	1.6	3.4	96,803	7,059	75% Agarose + 25% Collagen

Table B.2: Simple compression tests on the disc up to a thickness of 2.6mm (15% of 3mm) with hydration.

	Maximum Force [N]	Stiffness [N/mm]	Young modulus between 10 and 20% [Pa]	Maximum Stress [Pa]	Hydrogel
C10h	2.3	2.0	33,952	10,365	75% Agarose + 25% Alginate
C3h	6.0	6.3	129,436	27,899	75% Agarose + 25% Alginate
C7h	7.2	9.4	230,318	33,888	100% Agarose
C11h	9.3	7.3	161,057	43,671	100% Agarose
C9h	2.4	3.8	100,472	10,868	75% Agarose + 25% Collagen

Intentionally blank page.

References

[1] Tucker Peabody and Joe M Das. Anatomy, back, vertebral canal. *StatPearls*, 4 2022.

[2] Brody A. Frost, Sandra Camarero-Espinosa, and E. Johan Foster. Materials for the spine: Anatomy, problems, and solutions. *Materials*, 12, 1 2019.

[3] Joshua A. Waxenbaum, Vamsi Reddy, and Bennett Futterman. Anatomy, back, cervical vertebrae. *StatPearls*, 7 2022.

[4] Anatomy Info. Cervical spine anatomy & clinical significances. `https://anatomyinfo.com/cervical-spine/`, 2021. [Acessed: 08/03/2023].

[5] Jānis Šavlovskis and Kristaps Raits. Typical cervical vertebrae (c3—c6). `https://www.anatomystandard.com/Columna_Vertebralis/Vertebrae_Cervicales/Typical_Cervical.html`, 2021. [Acsessed: 15/02/2023].

[6] Heleni Vastardis and Carla A. Evans. Evaluation of cervical spine abnormalities on cephalometric radiographs. *American Journal of Orthodontics and Dentofacial Orthopedics*, 109(6):581–588, 1996.

[7] Noboru Goto and Naruhito Otsuka. Development and anatomy of the spinal cord. *Neuropathology*, 17:25–31, 1997.

[8] Tracey A. Cho. Spinal cord functional anatomy. *CONTINUUM Lifelong Learning in Neurology*, 21:13–35, 2 2015.

[9] J S Pooni, Dwl Hukins, P F Harris, R C Hilton, and K E Davies. Surgical radiologic anatomy comparison of the structure of human intervertebral discs in the cervical, thoracic and lumbar regions of the spine comparaison de la structure des disques intervert6-braux humains dans les r6gions cervicale, thoracique et lombaire de la colonne vert6brale. *SRA*, 8:175–182, 1986.

[10] Yan Yu, Jing Sheng Li, Tao Guo, Zhao Lang, James D. Kang, Liming Cheng, Guoan Li, and Thomas D. Cha. Normal intervertebral segment rotation of the subaxial cervical spine: An in vivo study of dynamic neck motions. *Journal of orthopaedic translation*, 18:32–39, 7 2019.

[11] Isma Liza Mohd Isa, Seong Lin Teoh, Nurul Huda Mohd Nor, and Sabarul Afian Mokhtar. Discogenic low back pain: Anatomy, pathophysiology and treatments of intervertebral disc degeneration. *International Journal of Molecular Sciences 2023, Vol. 24, Page 208*, 24:208, 12 2022.

[12] Alyah H Shamsah. *Electrospinning Annulus Fibrosus Mimics: An In vitro Tissue Engineering Approach for Intervertebral Disc Repair*. PhD thesis, University of Manchester, 2019.

[13] Helium Mak. Biomaterial for cervical intervertebral disc prosthesis. *Electronic Thesis and Dissertation Repository*, 8 2021.

[14] Lee A. Tan, K. Daniel Riew, and Vincent C. Traynelis. Cervical spine deformity - part 1: Biomechanics, radiographic parameters, and classification. *Neurosurgery*, 81:197–203, 8 2017.

[15] Erik E Swartz, ; R T Floyd, and Mike Cendoma. by the national athletic trainers. *Journal of Athletic Training 155 Journal of Athletic Training*, 40:155–161, 2005.

[16] Musculoskeletal Key. Neck assessment. `https://musculoskeletalkey.com/neck-assessment/`, 2019. [Acessed: 2023/02/22].

[17] Roger W Nightingale, Daniel L Camacho, Andrew J Armstrong, Joseph J Robinette, and Barry S Myers. Inertial properties and loading rates a!ect buckling modes and injury mechanisms in the cervical spine, 2000.

[18] Jeff M. Barrett, Laura A. Healey, Colin D. McKinnon, Andrew C. Laing, Clark R. Dickerson, Steven L. Fischer, and Jack P. Callaghan. Head supported mass, moment of inertia, neck loads and stability: A simulation study. *Journal of Biomechanics*, 146, 1 2023.

[19] N. Newell, J. P. Little, A. Christou, M. A. Adams, C. J. Adam, and S. D. Masouros. Biomechanics of the human intervertebral disc: A review of testing techniques and results. *Journal of the Mechanical Behavior of Biomedical Materials*, 69:420–434, 5 2017.

[20] Narayan Yoganandan, Srirangam Kumaresan, and Frank A. Pintar. Biomechanics of the cervical spine. part 2. cervical spine soft tissue responses and biomechanical modeling. *Clinical Biomechanics*, 16:1–27, 1 2001.

[21] Srirangam Kumaresan, Narayan Yoganandan, Frank A. Pintar, and Dennis J. Maiman. Finite element modeling of the cervical spine: Role of intervertebral disc under axial and eccentric loads. *Medical Engineering and Physics*, 21:689–700, 12 1999.

[22] Christian M. Puttlitz, Marc Antoine Rousseau, Zheng Xu, Serena Hu, Bobby K.B. Tay, and Jeffrey C. Lotz. Intervertebral disc replacement maintains cervical spine kinetics. *Spine*, 29:2809–2814, 2004.

[23] MANOHAR PANJABI, JIRI DVORAK, JOANNE DURANCEAU, ISAO YAMAMOTO, MARCUS GERBER, WOLFGANG RAUSCHNING, and H ULRICH BUEFF. Three-dimensional movements of the upper cervical spine. *Spine*, 13:726–730, 7 1988.

[24] Manohar M. Panjabi, Joseph J. Crisco, Anita Vasavada, Takenori Oda, Jacek Cholewicki, Kimio Nibu, and Eon Shin. Mechanical properties of the human cervical

spine as shown by three-dimensional load-displacement curves. *Spine*, 26:2692–2700, 12 2001.

[25] N. Yoganandan, F. A. Pintar, D. J. Maiman, J. F. Cusick, A. Sances, and P. R. Walsh. Human head-neck biomechanics under axial tension. *Medical Engineering and Physics*, 18:289–294, 1996.

[26] Nandan L. Nerurkar, Dawn M. Elliott, and Robert L. Mauck. Mechanical design criteria for intervertebral disc tissue engineering. *Journal of biomechanics*, 43:1017–1030, 4 2010.

[27] T. P. Green, M. A. Adams, and P. Dolan. Tensile properties of the annulus fibrosus - ii. ultimate tensile strength and fatigue life. *European Spine Journal*, 2:209–214, 12 1993.

[28] J. C. Lotz, A. J. Fields, and E. C. Liebenberg. The role of the vertebral end plate in low back pain. *Global Spine Journal*, 3:153–163, 5 2013.

[29] Nikolaos Maniadakis and Alastair Gray. The economic burden of back pain in the uk. *Pain*, 84:95–103, 1 2000.

[30] William Rea, Sandeep Kapur, and Hirachand Mutagi. Intervertebral disc as a source of pain. *Continuing Education in Anaesthesia Critical Care & Pain*, 12:279–282, 12 2012.

[31] Akinobu Suzuki, Michael D. Daubs, Tetsuo Hayashi, Monchai Ruangchainikom, Chenjie Xiong, Kevin Phan, Trevor P. Scott, and Jeffery C. Wang. Magnetic resonance classification system of cervical intervertebral disk degeneration. *Clinical Spine Surgery*, 30:E547–E553, 5 2017.

[32] Maciej Radek, Barbara Pacholczyk-Sienicka, Stefan Jankowski, Łukasz Albrecht, Magdalena Grodzka, Adam Depta, and Andrzej Radek. Assessing the correlation between the degree of disc degeneration on the pfirrmann scale and the metabolites identified in hr-mas nmr spectroscopy. *Magnetic resonance imaging*, 34:376–380, 5 2016.

[33] Stephen M. Eisenstein, Birender Balain, and Sally Roberts. Current treatment options for intervertebral disc pathologies. *Cartilage*, 11:143, 4 2020.

[34] R. Bohinski. Anterior cervical discectomy & fusion. `https://mayfieldclinic.com/pe-acdf.htm`, 3 2023. [Acessed: 13/03/2023].

[35] Elizabeth Chong, Matthew H. Pelletier, Ralph J. Mobbs, and William R. Walsh. The design evolution of interbody cages in anterior cervical discectomy and fusion: A systematic review orthopedics and biomechanics. *BMC Musculoskeletal Disorders*, 16:1–11, 4 2015.

[36] Fadi Taher, David Essig, Darren R. Lebl, Alexander P. Hughes, Andrew A. Sama, Frank P. Cammisa, and Federico P. Girardi. Lumbar degenerative disc disease: current and future concepts of diagnosis and management. *Advances in orthopedics*, 2012:1–7, 2012.

[37] G. Matgé. Cervical cage fusion with 5 different implants: 250 cases. *Acta Neurochirurgica*, 144:539–550, 3 2002.

[38] Sean S. Rajaee, Hyun W. Bae, Linda E.A. Kanim, and Rick B. Delamarter. Spinal fusion in the united states: analysis of trends from 1998 to 2008. *Spine*, 37:67–76, 1 2012.

[39] Kevin Phan, Matthew H. Pelletier, Prashanth J. Rao, Wen Jie Choy, William R. Walsh, and Ralph J. Mobbs. Integral fixation titanium/polyetheretherketone cages for cervical arthrodesis: Evolution of cage design and early radiological outcomes and fusion rates. *Orthopaedic Surgery*, 11:52–59, 2 2019.

[40] Denitsa D. Kiradzhiyska and Rositsa D. Mantcheva. Overview of biocompatible materials and their use in medicine. *Folia medica*, 61:34–40, 3 2019.

[41] Jeremy C Wang and Regis W Haid. *Clinical Neurosurgery*, volume 52, chapter 20. Lippincott Williams & Wilkins, 2005.

[42] Michael D. Staudt, Kaushik Das, and Neil Duggal. Does design matter? cervical disc replacements under review. *Neurosurgical Review*, 41:399–407, 4 2018.

[43] Yahya A. Othman, Ravi Verma, and Sheeraz A. Qureshi. Artificial disc replacement in spine surgery. *Annals of Translational Medicine*, 7:S170–S170, 9 2019.

[44] John Reeks, Hong Liang, J Philippe Kretzer, and Amir Kamali. Materials and their failure mechanisms in total disc replacement. *Lubricants 2015, Vol. 3, Pages 346-364*, 3:346–364, 4 2015.

[45] Vincent C Traynelis. Cervical arthroplasty. *Clinical Neurosurgery*, 53:203, 2006.

[46] David Turkov, Alan Job, Cesar Iturriaga, and Rohit B Verma. Current concepts of cervical disc arthroplasty. *Downloaded from International Journal of Spine Surgery*, 60504:1174–1183, 2023.

[47] Timothy C. Chin-See-Chong, Pravesh S. Gadjradj, Robert J. Boelen, and Biswadjiet S. Harhangi. Current practice of cervical disc arthroplasty: a survey among 383 aospine international members. *Neurosurgical focus*, 42, 2017.

[48] Food and Drug Administration. P070001 summary of safety and effectiveness data (prodisc-c). `https://www.accessdata.fda.gov/cdrh_docs/pdf7/p070001b.pdf`, 12 2007. [Accessed: 27/03/2023].

[49] Food and Drug Administration. P090029b summary of safety and effectiveness data (prestige-lp). `http://www.accessdata.fda.gov/cdrh_docs/pdf9/P090029B.pdf`, 7 2016.

[50] Food and Drug Administration. P170036b summary of safety and effectiveness data (mc-6). `https://www.fda.gov/`, 2 2019.

[51] Jean yves Lazennec, Alain Aaron, Olivier Ricart, and Jean Patrick Rakover. The innovative viscoelastic cp esp cervical disk prosthesis with six degrees of freedom: biomechanical concepts, development program and preliminary clinical experience. *European Journal of Orthopaedic Surgery and Traumatology*, 26:9–19, 1 2016.

[52] Evivo Biomaterials. The cervical prosthesis. https://evivobio.com/products/cp-esp/. [Accessed: 21/03/2023].

[53] Robert J. Hacker, Joseph C. Cauthen, Thomas J. Gilbert, and Steven L. Griffith. A prospective randomized multicenter clinical evaluation of an anterior cervical fusion cage. *Spine*, 25:2646–2655, 10 2000.

[54] Thomas A. Zdeblick and Frank M. Phillips. Interbody cage devices. *Spine*, 28, 8 2003.

[55] Benjamin Whatley. *BIOFABRICATION OF SCAFFOLDS FOR INTERVERTEBRAL DISC (IVD) TISSUE REGENERATION*. PhD thesis, Clemson University, 8 2013.

[56] Antonio Gloria, Filippo Causa, Roberto De Santis, Paolo Antonio Netti, and Luigi Ambrosio. Dynamic-mechanical properties of a novel composite intervertebral disc prosthesis. *Journal of materials science. Materials in medicine*, 18:2159–2165, 11 2007.

[57] Mariana Vasquez-Alvarez, Uriel Zapata, and Fanny L. Casado. Development of an intervertebral disc for cervical spondylosis composed of seeded biomaterials. *Annual International Conference of the IEEE Engineering in Medicine and Biology Society. IEEE Engineering in Medicine and Biology Society. Annual International Conference*, 2022:3931–3934, 2022.

[58] Celien A.M. Jacobs, Christoph J. Siepe, and Keita Ito. Viscoelastic cervical total disc replacement devices: Design concepts. *The spine journal : official journal of the North American Spine Society*, 20:1911–1924, 12 2020.

[59] Alan McLeod. Health innovation support - medical devices experience. https://www.healthinnovationsupport.co.uk/experience/, 2017. [Accessed: 18/04/2023].

[60] Kenneth A. Pettine. Clinical and radiographic outcome of the neodisc cervical total disc replacement (tdr) at 2-year follow-up. *The Spine Journal*, 10:S44, 9 2010.

[61] Food and Drug Administration. P060023b summary of safety and effectiveness data (bryan cervical disc). https://www.fda.gov/, 5 2009.

[62] Afonso J.C. Silva, Ricardo J. Alves de Sousa, Fábio A.O. Fernandes, Mariusz Ptak, and Marco P.L. Parente. Development of a finite element model of the cervical spine and validation of a functional spinal unit. *Applied Sciences 2022, Vol. 12, Page 11295*, 12:11295, 11 2022.

[63] Matthew D. Harmon, Daisy M. Ramos, D. Nithyadevi, Rosalie Bordett, Swetha Rudraiah, Syam P. Nukavarapu, Isaac L. Moss, and Sangamesh G. Kumbar. Growing a backbone - functional biomaterials and structures for intervertebral disc (ivd) repair and regeneration: challenges, innovations, and future directions. *Biomaterials science*, 8:1216–1239, 3 2020.

[64] Vishakha (Gajre)Kulkarni, Kishor Butte, and Sudha Rathod. Natural polymers-a comprehensive review. *International Journal of Research in Pharmaceutical and Biomedical Sciences*, 3:1597–1613, 12 2012.

[65] Fatemeh Asghari, Mohammad Samiei, Khosro Adibkia, Abolfazl Akbarzadeh, and Soodabeh Davaran. Biodegradable and biocompatible polymers for tissue engineering application: a review. *Artificial cells, nanomedicine, and biotechnology*, 45:185–192, 2 2017.

[66] Elsie S. Place, Julian H. George, Charlotte K. Williams, and Molly M. Stevens. Synthetic polymer scaffolds for tissue engineering. *Chemical Society reviews*, 38:1139–1151, 3 2009.

[67] Chenxi Li, Jia Chen, Yarong Lv, Yueqi Liu, Quanyi Guo, Jiandong Wang, Ce Wang, Ping Hu, and Yong Liu. Recent progress in electrospun nanofiber-based degenerated intervertebral disc repair. *ACS Biomaterials Science and Engineering*, 8:16–31, 1 2022.

[68] F. Croisier, A. S. Duwez, C. Jérôme, A. F. Léonard, K. O. Van Der Werf, P. J. Dijkstra, and M. L. Bennink. Mechanical testing of electrospun pcl fibers. *Acta Biomaterialia*, 8:218–224, 1 2012.

[69] Roberto Scaffaro, Francesco Lopresti, Luigi Botta, and Andrea Maio. Mechanical behavior of polylactic acid/polycaprolactone porous layered functional composites. *Composites Part B: Engineering*, 98:70–77, 8 2016.

[70] Rita Costa Amador. Development of an experiment plan with 3d electrospinning equipment for cartilage tissue engineering, 2022.

[71] Kaiwen Zheng and Dajiang Du. Recent advances of hydrogel-based biomaterials for intervertebral disc tissue treatment: A literature review. *Journal of tissue engineering and regenerative medicine*, 15:299–321, 4 2021.

[72] Chunxu Li, Qiushi Bai, Yuxiao Lai, Jingjing Tian, Jiahao Li, Xiaodan Sun, and Yu Zhao. Advances and prospects in biomaterials for intervertebral disk regeneration. *Frontiers in Bioengineering and Biotechnology*, 9:22, 10 2021.

[73] Guoke Tang, Bingyan Zhou, Feng Li, Weiheng Wang, Yi Liu, Xing Wang, Chao Liu, and Xiaojian Ye. Advances of naturally derived and synthetic hydrogels for intervertebral disk regeneration. *Frontiers in Bioengineering and Biotechnology*, 8:745, 6 2020.

[74] Michel Vong, Francisco Javiez Diaz Sanchez, Antonios Keirouz, Wiwat Nuansing, and Norbert Radacsi. Ultrafast fabrication of nanofiber-based 3d macrostructures by 3d electrospinning. *Materials and Design*, 208, 10 2021.

[75] Antonios Keirouz, Michael Chung, Jaehoon Kwon, Giuseppino Fortunato, and Norbert Radacsi. 2d and 3d electrospinning technologies for the fabrication of nanofibrous scaffolds for skin tissue engineering: A review. *Wiley Interdisciplinary Reviews: Nanomedicine and Nanobiotechnology*, 12, 7 2020.

[76] Mihael Lazebnik, Milind Singh, Paul Glatt, Lisa A. Friis, Cory J. Berkland, and Michael S. Detamore. Biomimetic method for combining the nucleus pulposus and annulus fibrosus for intervertebral disc tissue engineering. *Journal of tissue engineering and regenerative medicine*, 5, 2011.

[77] Conor T. Buckley, Stephen D. Thorpe, Fergal J. O'Brien, Anthony J. Robinson, and Daniel J. Kelly. The effect of concentration, thermal history and cell seeding density on the initial mechanical properties of agarose hydrogels. *Journal of the Mechanical Behavior of Biomedical Materials*, 2:512–521, 10 2009.

[78] Georgia Kaklamani, David Cheneler, Liam M. Grover, Michael J. Adams, and James Bowen. Mechanical properties of alginate hydrogels manufactured using external gelation. *Journal of the Mechanical Behavior of Biomedical Materials*, 36:135–142, 8 2014.

[79] Dassault Systèmes 3DEXPERIENCE. Transversely isotropic elasticity - user assistance r2023x. `https://help.3ds.com/2023x/english/dsdoc/simmatusermap/simmat-c-elastic-transverselyisotropic.htm?contextscope=cloud&highlight=transverselly+isotropic+elasticity&id=f50774cb8d4a4539b521dc16cdfc6abc&analyticsContext=search-result&analyticsSearch=transverselly+isotropic+elasticity&myapp=false`, 2023. [Accessed: 29/03/2023].

[80] Marta Kurutz and Marta Kurutz. *Finite Element Modelling of Human Lumbar Spine*, chapter 9, pages 151–171. IntechOpen, 8 2010.

[81] Grace D. O'Connell, Edward J. Vresilovic, and Dawn M. Elliott. Human intervertebral disc internal strain in compression: the effect of disc region, loading position, and degeneration. *Journal of orthopaedic research : official publication of the Orthopaedic Research Society*, 29:547–555, 4 2011.

[82] A. Completo and P. Marques. Automated manufacturing of three-dimensional cell matrices with nanofibres of controlled alignment and uniform cell distribution, 9 2021.